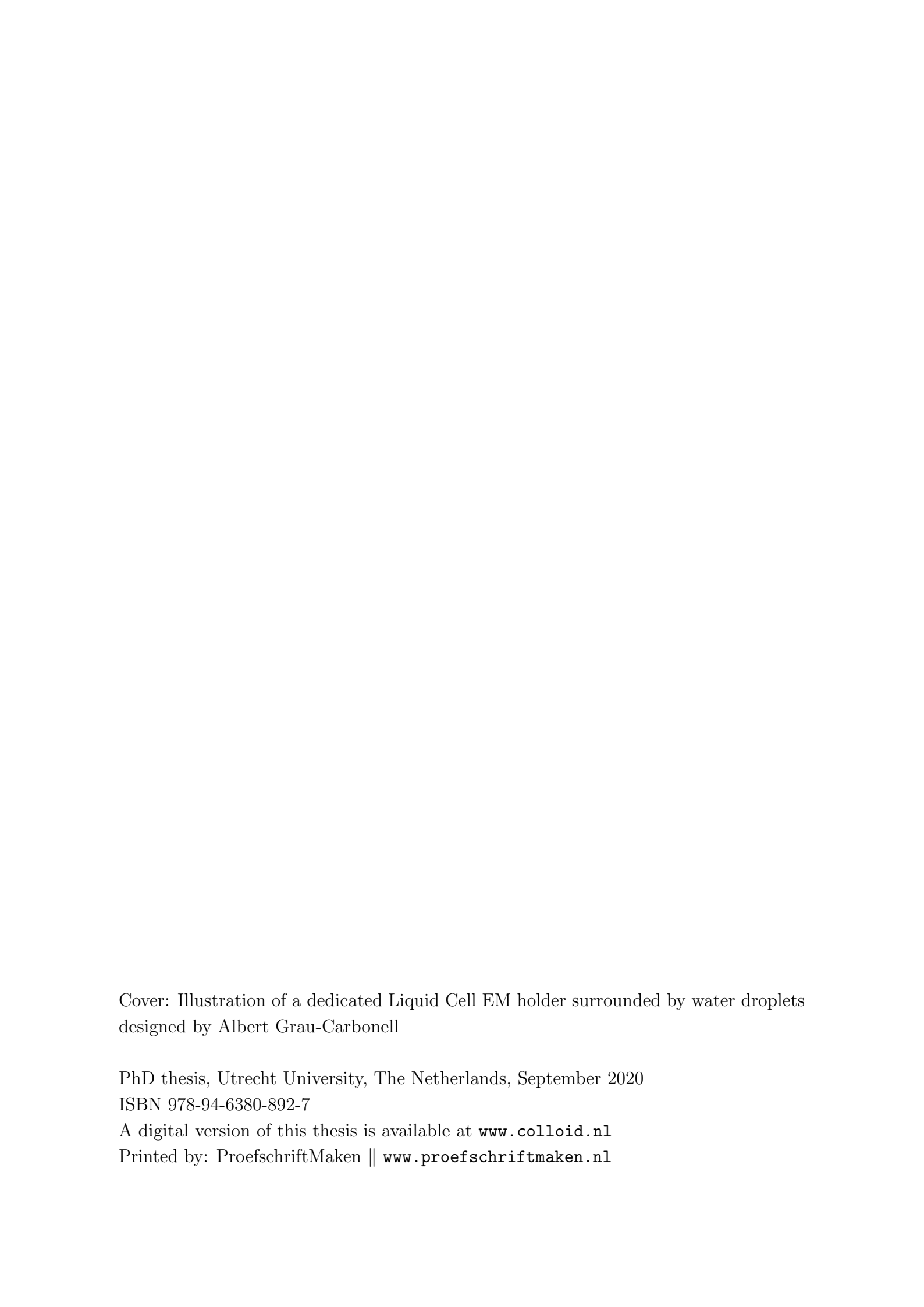


**Chemistry and interactions of silica
based particles studied by liquid
cell electron microscopy**

A completely blank white page with no visible content or markings.

Cover: Illustration of a dedicated Liquid Cell EM holder surrounded by water droplets
designed by Albert Grau-Carbonell

PhD thesis, Utrecht University, The Netherlands, September 2020

ISBN 978-94-6380-892-7

A digital version of this thesis is available at www.colloid.nl

Printed by: ProefschriftMaken || www.proefschriftmaken.nl

Chemistry and interactions of silica based particles studied by liquid cell electron microscopy

Chemie en interacties van silica-gebaseerde deeltjes bestudeerd
met behulp van vloeistofcel-elektronenmicroscopie

(met een samenvatting in het Nederlands)

Proefschrift

ter verkrijging van de graad van doctor aan de
Universiteit Utrecht op gezag van de rector magnificus,
prof. dr. H.R.B.M. Kummeling, ingevolge het besluit van het
college voor promoties in het openbaar te verdedigen
op woensdag 2 september 2020 des ochtends te 11.00 uur

door

Sina Sadighikia

geboren op 12 mei 1990 te Tabriz, Iran

Promotor: Prof. dr. A. van Blaaderen

Copromotor: Dr. ir. M.A. van Huis

The research in this thesis was financially supported by the NWO-TTW Perspectief Program ‘Understanding Processes Using Operando Nanoscopy’, project UPON-B3 (No. 14206).

Contents

Chapter 1. Introduction	1
Chapter 2. Electron beam induced shape-deformation of silica based particles in liquid phase electron microscopy	15
Chapter 3. Liquid cell scanning transmission electron microscopy study of diffusion of colloidal particles inside spherical shells	31
Chapter 4. In-situ study of the wet chemical etching of SiO ₂ and Metal(oxide)@SiO ₂ core-shell nanospheres	59
Chapter 5. Complex internal chemical structures of rod-shaped silica colloids investigated by in-situ etching using low-dose liquid cell electron microscopy	85
Bibliography	113
Summary	129
Samenvatting	133
Acknowledgments	138
List of Publications	143
About the Author	145

1

Introduction

1.1. COLLOIDS

A distribution of particles of one phase throughout another continuous phase is known as a colloidal suspension if the particles have size roughly sizes as small as several nm to as large as several micrometers. Particles that have this characteristic are known as colloidal particles because in their theoretical description one can integrate out the usually much faster and smaller length scale degrees of freedom of the solvent they are dispersed in. Generally, colloidal particles are small enough that they do not settle completely to the bottom of a vessel upon standing although for the larger particles sedimentation diffusion equilibria can form. In most cases, the colloidal particles are large enough to scatter light. This observation was made by Faraday who noticed that a narrowly defined beam of light passing through a gold colloidal suspension shows the light ray passing through the dispersion. This phenomenon was further studied by Tyndall and is known as the Tyndall effect [1–3]. Therefore a dispersion of colloidal particles usually appears cloudy or opaque. A colloid and a solution can be distinguished in this way, by shining a beam of light and checking whether the scattering happens or not. A familiar observation of the Tyndall effect in daily life is seeing the rays of light which become visible when light is scattered by colloidal particles in the air (smoke, dust, fog) (Figure 1.1). Other daily life examples of colloids include inks, paints (solid in a liquid known as sol), clouds, fog (liquid in gas known as aerosol), milk, mayonnaise, butter (liquid in a liquid known as an emulsion), and foams, whipped cream (gas in a liquid known as foam).



FIGURE 1.1. Scattering of light by colloidal particles in the air (fog in this case), which becomes visible as paths of light beams known as the Tyndall effect.

Besides the broad technological applications, colloids are of interest since they can be used to study the fundamental properties of matter. The above-mentioned upper-size limit for colloids is usually defined by Brownian motion [4]. Because of their size, colloidal particles experience a diffusive motion that is caused by solvent molecules that collide with them. This motion is irregular, consisting of translations and rotations, where the particles move even when they get close to each other. In 1827, Robert Brown used a microscope to observe the motion of pollen grains. Although he was not the first to make such an observation, this effect has come to be known as Brownian motion. In 1991 a researcher (D. H. Deutsch) [5] was doubting whether Brown actually investigated ‘real’ diffusive Brownian motion in his research. His arguments were kind of: Brown’s system was too noisy, that he did not use cover slips (not yet invented), the microscope was not powerful enough, the pollen particles were much too large, too light or too heavy, so he was actually looking at vibrations, drying induced motion, etc. However, G. Cadée countered in a letter to Nature, that Deutsch had not read Brown’s work that well as Brown clearly stated that he did not look at the motion of Pollen particles but instead [6]: *“if he had read Brown’s papers more thoroughly, he would have noted that Brown did not describe the movements of pollen grains, which indeed are too large for Brownian motion, but described movements of particles inside pollen grains (see also the title of his paper).”* He was mentioning the paper by Brown [7] entitled

“A brief account of microscopical observations made in the months of June, July and August, 1827, on the particles contained in the pollen of plants and the general existence of active molecules.” In short, Brown used the Pollens particles and the motion of the micron-sized particles inside like a yolk-shell system (This type of particle systems were studied in this Thesis), thus also making it much less likely that (even without the use of cover glasses (not yet invented) his observations were incorrectly influenced by external vibrations and/or drying forces. Brown also mentioned that in some grasses, the membrane of the pollen was so transparent that the motion of the particles could be seen inside the intact pollen grains, where currents or evaporation can be excluded as a cause of the movements observed. Deutsch did not agree [8]. But for most scientists, it was B.J. Ford who had already reported on Brown’s work earlier using the same microscope that Brown used, who as closely as he could, redid Brown’s experiments and made video recordings of what he observed [9]. However, the leading improvement was made by Albert Einstein who used colloid-atom analogy to theoretically explain the so-called Brownian motion in 1905 [10]. Shortly after, Jean Baptiste Perrin [11] experimentally tested successfully Einstein’s theory in 1908 by measuring both the translational and rotational diffusion of particles using light microscopy. The Brownian motion is driven by thermal energy and if this energy dominates the gravitational energy, colloidal suspensions may reach thermodynamic equilibrium states. Showing thermodynamic properties similar to those of atomic systems makes colloids a superb model system to study condensed matter physics phenomena such as homogeneous [12, 13], and heterogeneous [14] crystal nucleation. “Colloidal crystals” is an excellent example illustrating the analogy between colloids and atomic systems where they can be used to study crystallization and melting [15, 16]. There are some advantages to studying colloids over atomic systems. First of all, they have much larger dimensions compared to atoms which makes the dynamics of these particles slower so that they can be studied in real time and real space. Moreover, the extensive possibilities of making diverse colloidal particles in a broad variety of length scales, shapes, and surface charges, together with the ability to change temperature, and solvent properties (e.g. the ionic strength), makes it feasible to tune the colloid-colloid interactions to a certain degree. In contrast, the interactions between molecules and atoms are almost completely fixed.

1.2. INTERACTIONS BETWEEN COLLOIDS

Charged colloidal particles immersed in an electrolyte solution are surrounded by an ionic ‘cloud’ formed by the mobile electrolyte ions. This ionic cloud contains both co-ions (electrolyte ions with charges of the same sign as the particle surface charges), and counter-ions (electrolyte ions with charges opposite to that of the particle surface charges). However, due to electrostatic interactions between electrolyte ions and particle surface charges, close to the particle surface the concentration of counter-ions is much

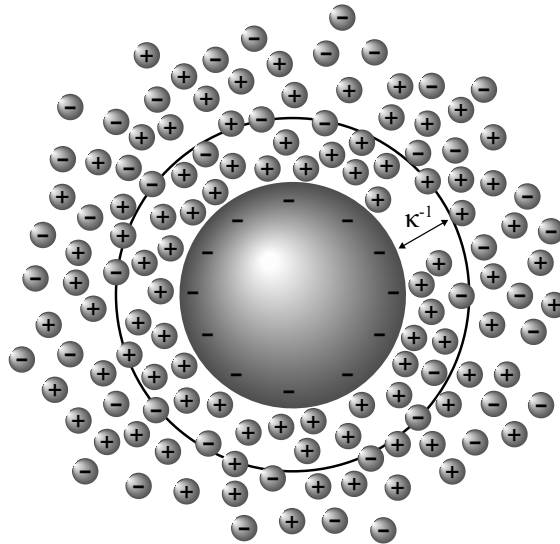


FIGURE 1.2. The distribution of ions around a charged spherical particle of radius a . The thickness of the electric double layer (Debye length) around the spherical particle is κ^{-1} .

higher than that of the co-ions. Figure 1.2 schematically shows the distribution of ions around a charged spherical particle of radius a . The charge on the particle surface along with the ionic cloud surrounding it forms the so-called electric double layer. Due to the thermal motion of ions, the distribution of the counter-ions around the particle has a diffuse structure and it decays as a function of the distance from the particle surface.

The presence of the electric double layer around the charged particle causes colloidal particles to interact with each other. In the case of having a surface charge of the same sign on the particles, this interaction would be repulsive. The distribution of counter-ions around the particle and the electric potential across the electric double layer strongly affects the electrostatic interaction between colloidal particles [17, 18]. In addition to repulsive electrostatic interactions, there is an attractive interaction between colloids due to the van der Waals forces [19]. The attractive intermolecular forces (also known as van der Waals forces) arise as a result of the interactions between the fluctuating instantaneous electric dipoles of the atoms and molecules forming the colloidal particles. If there is no repulsion, the attraction interactions due to van der Waals forces results in aggregation of the particles that is too strong to overcome with thermal fluctuations. Therefore, the stability of colloidal particles in a colloidal system depends on the balance between the electrostatic interaction and the van der Waals interaction between particles.

Derjaguin and Landau, and Verwey and Overbeek [17, 18] were two pair of scientists who independently derived a theory to explain the interactions between two charged spherical particles. The DLVO theory assumes that the electrostatic double layer forces

and the van der Waals forces are independent and can be summed up at each interacting distance for two particles. Hence, the full interaction potential between two charged spherical particle can be calculated via DLVO theory [17,18] by summing van der Waals interaction

$$U_{vdw} = -\frac{A}{3} \left(\frac{a_1 a_2}{r^2 - (a_1 + a_2)^2} + \frac{a_1 a_2}{r^2 - (a_1 - a_2)^2} + \frac{1}{2} \text{Log} \left[\frac{r^2 - (a_1 + a_2)^2}{r^2 - (a_1 - a_2)^2} \right] \right)$$

and the electrostatic interaction

$$U_{es} = \lambda_b \frac{Q_1 Q_2}{(1 + \kappa a_1)(1 + \kappa a_2)} \frac{e^{-\kappa(r-a_1-a_2)}}{r}.$$

Here A is the Hamaker constant, a is the radius of the charged particles, r the center-to-center distance, λ_b is the Bjerrum length, Q is the number of charges, e is the elementary charge, ϵ_0 is the permittivity of the vacuum, ϵ_m is the dielectric constant of the medium, κ is the inverse Debye screening length which is the length at which the inhomogeneous distributions in the ion concentrations drop to $1/e$ of the values, similarly as the skin depth inside a metal and thus can roughly be interpreted as the distance over which charged particles significantly interact as compared to their thermal energy. The Debye screening length depends on the ion concentration that screens the charge on the particle. It can be calculated as follows:

$$\kappa = \sqrt{\frac{2N_A c e^2}{\epsilon_0 \epsilon_m k_B T}}$$

where N_A is Avogadro's number, and c is the ion concentration in the bulk. According to the Debye screening length formula, it can be realized that one can tune the repulsive range between two charged particles by changing the salt concentration of the electrolyte solution.

The intriguing analogy between the colloidal dispersions and the atomic systems breaks down when the comparison shifts from thermodynamic equilibrium properties to dynamics. As already mentioned above two colloidal particles "directly" interact with each other through their inter-particle interactions just as atoms and molecules. However, the particle movement through its dispersion displaces the solution in between two particles which consequently induces a force on another particle. Here there is an "indirect" interaction between particles through the liquid medium which has no corresponding interaction in atomic systems since atoms move in a vacuum. Moreover, because of the same origin of the Brownian motion and the hydrodynamic interactions (medium molecules), the study of the dynamics of colloidal particles is rather complicated [20].

In this thesis, we used a new class of colloidal particles where one particle is entrapped by moving within another hollow particle. Both of these particles have a similar charge on their surfaces, thus they have electrostatic repulsion interactions with each other.

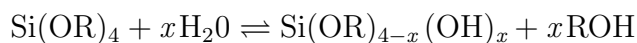
Because of their different geometry compared to two spherical charged particles, the electrostatic interactions cannot be analytically described by the DLVO theory. This so-called ‘rattle’ particle, is a perfect system to test the hydrodynamic interactions of a single particle with its environment; studying and understanding the interactions between these particles in this kind of geometry is therefore of great interest. Because the particles inside the shells can be moved with external fields, like an electric field, these kinds of shells with movable cores are also interesting for several tunable photonic applications.

1.3. SILICA

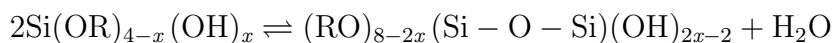
None of the above-mentioned physical properties can be studied unless we have a monodisperse model system. Currently, a vast variety of colloids can be synthesized out of various materials with different shapes and sizes. Polystyrene [21], polymethylmethacrylate (PMMA) [22, 23], silica [24, 25], titania [26, 27], and poly (N-isopropylacrylamide) (pNIPAM) [28] can be mentioned as amongst the most common ones. Silica in particular is of great interest because of its excellent thermal, chemical, and mechanical properties. The word silica which is also known as silicon oxide can be referred to all natural and synthetic, crystalline, or amorphous types. However, in this thesis synthetic amorphous silica in the colloidal state is studied. Although silica is a common material being one of the major components of the earth’s crust, there is still much to learn about silica and its chemical and physical properties. Since, Stöber, Fink and Bohn [29] developed a procedure for the synthesis of monodispersed colloidal silica particles in 1968, different modified procedures have been developed to produce silica particles with different shapes and chemical structures. Three main strategies of synthesizing silica spherical particles include the Stöber [29], water-in-oil microemulsion [30], and Amino Acid-Catalyzed (AAC) [31–34] procedures. In subsequent sections, the synthesis method along with the properties of these silica particles will be described. In the following, two new types of silica particles which we have studied in this thesis, known as ‘rod-like’ silica particles and silica ‘rattles’ will be briefly introduced.

1.3.1. Stöber silica

The synthesis procedure in the Stöber method is based on the hydrolysis and condensation polymerization of alkoxy silanes. During the hydrolysis reaction the alkoxy-arms of the silica precursor are hydrolyzed as follows:



Then the condensation process takes place either by water condensation:



Or with alcohol condensation as in the following reaction:



Here x and $4-x$ represent the numbers of silanol and ethoxy groups, respectively ($x = 1-4$). The reaction medium is a short-chained alkanol together with water and ammonia as the basic catalyst. The synthesis has a relatively simple procedure starting with adding saturated ammonium hydroxide solution to alcohol(commonly ethanol)-water mixture followed by adding alkoxysilane precursor (commonly tetraethoxysilane, TEOS). Then the mixture is agitated throughout the overnight reaction.

The products of the hydrolysis part of the reaction are Si-OH groups, known as silanol groups. They are the reactive monomers from the silica precursor which subsequently react with one another in the condensation part of the reaction (water condensation) to yield branched Si-O-Si bonds, known as siloxane bonds. The first formation of these siloxane bonds can be linked to the nucleation and growth of silica particles, although it has been shown that aggregation between clusters is important as well early in the silica growth [24]. Apart from the reaction between two silanol monomers, they may also undergo a reaction with the unhydrolyzed ethoxyl groups of TEOS via condensation between silanol and ethoxyl groups (alcohol condensation). The latter reaction also participates in producing siloxane networks. During the hydrolysis stage, the OH⁻ ions attack at the silicon atom, causing a nucleophilic replacement to occur via pentacomplexation transition state [35,36]. This explains the fact that the presence of ammonia increases the hydrolysis rate in base-catalyzed reactions since the OH⁻ ions of ammonia are extremely effective nucleophiles as compared to H₂O molecules. As the reaction continues and more ethoxyl groups convert to silanol groups, the steric hindrance of ethoxyl groups to OH⁻ ions decreases which in turn causes an increase in the hydrolysis rate. The condensation stage which takes place by the reaction of two neighbor silanol monomers or silanol monomers with ethoxyl groups also occurs via nucleophilic attack, but this time the nucleophile is the silanol group. Condensation occurs at much higher rates compared to hydrolysis. This results in the condensation of silanol monomers onto large siloxane network and less onto other monomers [37].

The experimental parameters of the Stöber method have been extensively studied during the past decades to investigate their effects on the size, shape, and the chemical structure of the silica particles. The studies showed that the reaction rate is highly dependent on the length and thus polarity of the alcohols used. The faster reaction was reported for a shorter chained alcohol media [29]. Methanol yields the fastest reaction while the slowest reaction was reported when butanol was used as the medium [29]. However, the faster reaction results in a wider particle size distribution (higher polydispersity) [29]. Bogush *et al.* [38] investigated the effect of the temperature on the

particle size. They have reported that by increasing the temperature, the mean particle size decreased [38].

In principle, the silicon atom in a Stöber silica particle can be bonded to four other silicon atoms through oxygen atoms. When a silicon atom has four bonds with other silicon atoms it reaches the highest degree of condensation which is shown as Q^4 in NMR terminology (4 indicates the degree of condensation). However, in Stöber silica it is also possible that a fraction of the silicon atoms have fewer bonds to neighboring silicon atoms. For instance, there can be three bonds between silicon atoms. In this case, there is one silanol group in the siloxane structure. Similarly, this is shown as Q^3 . A Stöber silica particle might contain all siloxane structures (Q^1 to Q^4) meaning that it is not fully condensed and interconnected. Van Blaaderen *et al.* [39] investigated the structure of the siloxane network in silica particles using solid state ^{29}Si nuclear magnetic resonance spectroscopy (NMR) and reported that due to incomplete hydrolysis and condensation of TEOS, a small amount of ethoxy groups can be found in particles which results in an inhomogeneous internal structure of silica particles. This is of great interest when the dissolution of silica is being studied. This feature together with the ultra-microporous structure of the Stöber silica particles [40, 41] which allows the small species such as OH^- , and H^+ penetrate the structure, can be used to make new types of particles by selectively etching them. We will elaborate on this in further sections. According to the recommendations of a panel convened by the International Union of Pure and Applied Chemistry (IUPAC), materials with pores less than 1 nm are considered as ultra-microporous materials, those with pores less than 2 nm are considered as microporous, the ones with pores between 2 to 50 nm are defined as mesoporous, and materials with pores > 50 nm are considered as macroporous materials [42].

1.3.2. Silica particles made by water-in-oil (W/O) microemulsion method

One of the modified procedures derived from the Stöber method which is often used to synthesize highly monodispersed silica nanoparticles is the synthesis in a non-ionic water-in-oil microemulsion [30]. The synthesis procedure is based on hydrolysis and condensation of alkoxy silanes same as Stöber method, except that here the reaction takes place in water-in-oil microemulsion droplets. Water-in-oil (W/O) microemulsions (also known as reverse micellar solutions) are isotropic, optically transparent, and thermodynamically stable nano-sized liquid dispersions which consist of a continuous non-polar (oil) phase and a dispersed polar (aqueous) phase. These water droplets are thermodynamically compartmentalized by a surfactant. The nano-sized W/O microemulsion droplets act as microreactors where the hydrolysis and condensation reactions take place. They also act as steric barriers to prevent aggregation of the growing silica particles. Both polar and nonpolar reagents are soluble in microemulsion

media and it can occur in defined locations throughout the dispersion. This gives excellent control over hydrolysis and condensation reactions providing the advantage to synthesize highly monodispersed, smooth, and spherical silica particles. Particles synthesized with this method usually have a size range between 25 and 70 nm [30,43,44]. The water to surfactant molar ratio (R) plays a crucial role in the relative rates of hydrolysis and condensation reactions in a non-ionic microemulsion [45]. The complex effect of the water to surfactant ratio (R) and the ammonium hydroxide concentration on the particle size has been studied by Arriagada *et al.* [46]. They have shown that at relatively low ammonia concentration by increasing R the particle size decreases monotonically, while at higher ammonia concentrations the particle size goes through a minimum by increasing R [46]. An excellent study has been carried out by Chang *et al.* where they have investigated the effect of the oil and the surfactant type as well as the surfactant and the water concentration on the formation of silica particles and their size distribution [47]. Silica particles prepared in nonionic W/O microemulsions were found to have a less condensed structure (lower concentration of Q^4 silicon sites) compared to Stöber silica [39], which is one of the topics that we have studied in this thesis. Although highly monodispersed silica particles with great control on the particle size [48,49] is achievable with this synthesis technique, however, the presence of anionic or non-ionic surfactants and co-surfactants in the synthesis procedure make the subsequent cleaning steps more extensive and time-consuming [50].

1.3.3. Silica particles made by water-based amino acid-catalyzed method

The wide particle size distribution of sub 100 nm or nano-sized Stöber silica and the time-consuming cleaning steps in water-in-oil microemulsion method have raised the need for an alternative silica synthesis procedure without using surfactants to attain highly monodispersed silica nanoparticles. In recent years an environmentally friendly water-based synthesis has been developed by Yokoi *et al.* [31,32] and independently by Davis *et al.* [33,34] which takes place under weakly basic conditions (pH 9-10) through hydrolysis and condensation reactions of TEOS in water. The reaction is an amino acid-catalyzed seed regrowth procedure where the formation of new particles is suppressed during the overgrowth steps [51]. This method is different than the Stöber method in terms of using amino acid catalyst instead of ammonia which results in a lower pH of the reaction medium. The other difference is the different solvent used in two methods. While the Stöber method takes place in ethanol, the solvent for the amino acid-catalyzed method is water. The basic amino acids used in this method are usually lysine and arginine where they act also as a buffer to keep the pH of the solution constant during the reaction [52]. The first step of synthesis yields monodisperse silica seeds which can be used in further particle growth steps to obtain the desired particle size. The growth steps can be followed either by the Stöber method or completely by the amino

acid-catalyzed method. By varying the TEOS concentration or the synthesis condition the size of the seeds can be tuned between 8 to 35 nm [32]. Recently Shahabi *et al.* [53] have developed a synthesis procedure based on the amino acid-catalyzed method to make fluorescent silica particles by incorporating rhodamine B isothiocyanate (RBTC) organic fluorophore. The liquid-state ^1H NMR studies showed that the hydrolysis of TEOS occurs slowly at the oil-water interface due to weakly basic environment and the silicate species are consumed to grow the initially formed particles rather than producing new particles [32]. The slow and continuous supply of hydrolyzed TEOS in this method results in a different inter-particle chemical structure compared to Stöber silica particles. This characteristic of amino acid-catalyzed silica particles is studied in this thesis as well.

1.3.4. Silica yolk-shell (rattle) particles

A new class of particles with a distinctive core@void@shell configuration where the encapsulated core particle ‘freely’ moves within a hollow shell, is known as a yolk-shell particle [54–58]. They typically are shown as A@B particle where A and B represent the core and shell materials respectively. They are also termed as mobile core-shell or rattle-type nanostructures. In this thesis, we denote them as rattle particles. The unique structure of the rattle particles makes them advantageous in a wide variety of applications, such as drug/gene delivery [59, 60], catalysis [61, 62], lithium batteries [63, 64], and sensors [65–68]. The core material is usually a metal or metal oxide particle with e.g. optical [69] or catalytic [70] properties. Among various types of inorganic materials, silica is one of the most promising materials to be used as the shell because of its wide range of applications and advantageous chemical and mechanical properties. The advantages of a silica shell can be summarized as follows: simple to synthesize, chemically inert which is beneficial in biological applications [71], available in different shapes and functionalization of its surface for diverse purposes such as drug delivery [72], acting as a barrier for catalyst core to prevent aggregation and to increase the catalytic activity [73].

Among various approaches to synthesize rattle particles, selective removal of a sacrificial layer, or a dissolution method, are the most common ways to make rattles with a silica shell. Core-shell particles can be used to partially remove the core or the shell to make rattle particles. In this method first, core-shell particles with a core and one layer shell or double shells from different materials are made. Subsequently, a part of the core, shell or the inner shell is selectively removed. An example of utilizing this method can be found in Ref [74] where a core-shell particle with a ‘sandwich’ structure consisting of a core, an organic silica layer (prepared by hydrolysis and condensation of N-3-(trimethoxysilyl)propyl ethylenediamine), and an inorganic silica layer (prepared by hydrolysis and condensation of TEOS) was synthesized. Then

the middle layer (organosilica layer) was selectively removed by aqueous hydrofluoric acid (HF) etching resulting in a rattle-type particle. Another common procedure to synthesize rattle particles with selective removal method is to use polymers as the sacrificial layer. For instance, cross-linked polymethylmethacrylate (PMMA) is often used as the sacrificial layer between two inorganic materials which can be efficiently removed by heat treatment in which the polymer is burned away in an oxygen-rich atmosphere. Highly monodisperse rattles with various compositions such as $\text{SiO}_2@\text{SiO}_2$, $\text{TiO}_2@\text{SiO}_2$ can be synthesized using this method [75, 76]. Apart from the chemistry of rattle particles, the spherical confinement of a charged particle in another charged particle is an intriguing field of study in physics, and as mentioned advanced functional photonic materials are envisaged as well.

1.3.5. Rod-like silica particles

So far we have introduced spherical silica particles with different chemical structures. However, it is possible to make colloidal particles with different shapes such as triangles [77], cubes [78], platelets [79, 80], and octopods [81, 82]. Recently, a new shape of silica particles was developed by Kuijk *et al.* [83] known as rod-like silica particles. Although the reaction is based on hydrolysis and condensation of the silica precursor, like in the Stöber method, the anisotropic supply of the silica precursor (TEOS) results in growth only in one direction thereby forming a rod-like silica particle. The synthesis is a simple one-pot method where ethanol, water, sodium citrate, and ammonia were added to a solution of polyvinylpyrrolidone (PVP) in pentanol. This yields an emulsion of water droplets which further includes the base catalyst ammonia as well, next to PVP and sodium citrate in pentanol stabilized by sodium citrate and PVP. Upon the addition of apolar silica precursor (TEOS) to the continuous pentanol oil phase, the growth mechanism starts. Silica rods prepared with this method have a flat bottom end and a round tip. Due to the synthesis procedure of rod-like silica particles, they possess a unique chemical structure that can be subsequently manipulated by selectively etching the less condensed parts of the rods to make a new shape of silica particles [84]. Moreover, it has been shown that by changing the reaction conditions (e.g. tuning hydrolysis and condensation of silica precursors or changing the reaction temperature) during the growth of rods, various shapes of silica particles with inhomogeneous chemical structures can be synthesized [85, 86].

1.4. SILICA DISSOLUTION

The reverse process of hydrolysis and condensation is known as the dissolution of silica. Using this possibility, one can tailor the nano-structure and shape of silica particles by modifying the initial shape of the silica particle by selectively removing parts in well-controlled processes. During silica dissolution, the breakage of the Si-O-Si bonds

occurs which is known as a silica etching mechanism. The commonly used etchants in the dissolution of silica, are hydrofluoric acid (HF) or alkaline solutions such as NaOH or ammonia. It has been shown that the silica can be etched in hot water shortly after the synthesis of the particles [87,88]. However, due to the inhomogeneous chemical structure of the Stöber silica (see section 1.3.1), the outer shell of the particle becomes robust against etching when the particles are aged [88]. The most common way of etching silica particles that are synthesized by hydrolysis and condensation, is to dissolve them at pH above 9. The basic condition catalyzes the breakage of siloxane bonds and accelerates the etching process. In these solutions, the OH⁻ ions coordinate to Si atoms and break the siloxane bond by increasing the coordination number from four to five in a transition state complex. Etching in hot water and alkaline solutions can be chemically reversible by the bond formation among different preformed silicate oligomers. On the other hand, it is also possible to etch silica particles in acidic conditions. Hydrofluoric acid (HF) is often used to dissolve silica. Similar to OH⁻ ions, F⁻ ions attack the silicon atoms and break the Si-O-Si bonds which ultimately result in etching of the silica particle. Nevertheless, etching with HF is fast and irreversible, and the main etched products are gaseous Si-F compounds [89, 90]. HF was found to selectively etch the organic silica framework. Chen *et al.* [74] showed this by synthesizing a sandwiched silica nanoparticle system where the middle layer of the nanoparticles was formed by the co-condensation between TEOS and N-[3-(trimethoxysilyl)propyl]ethylenediamine. This layer was subsequently etched by HF to make rattle nanoparticles. The interior part of a poly(vinyl pyrrolidone) (PVP) coated Stöber silica can be selectively etched using NaOH [91]. Moreover, by using NaBH₄ as the etchant solution, silica nanoparticles were found to be directly transferred to hollow structures by a dissolution-regrowth mechanism [92].

Apart from the pH and the solvent temperature, other parameters such as the presence of the impurities, size and the shape of the particles, and hydrothermal conditions. affect the dissolution of silica nanoparticles.

1.5. SCOPE OF THIS THESIS

This thesis covers a broad study on the physio-chemical properties of various types of silica nanoparticles. Understanding the complex chemical structure of different types of silica nanoparticles makes it possible to obtain novel shapes of silica nanoparticles by tailoring their chemical composition. The shape of the colloidal particles greatly affects the phase behavior, and ultimately leads to new materials with desired unique properties. On the other hand, studying the interactions between colloidal particles with complicated structures helps to understand the phase behavior and the self-assembly of colloidal nanoparticles. In this thesis, these topics are studied using Liquid Phase

Electron Microscopy (LPEM) which is a recently emerged in-situ microscopy method [93–95].

In **chapter 2**, we introduce LPEM, the core characterization method in this thesis, and the limitations associated with this technique which affect our system of particles. Moreover, we will investigate the beam-induced phenomena found in the LPEM experiments on various silica-based particles. We make use of this knowledge in **chapter 3** to study the diffusion of a spherical charged particle entrapped in another spherical charged particle. In this chapter, we study the effect of the electron beam irradiation on the diffusion of the colloidal particle within a spherical shell and we find the conditions where the effects of the electron beam irradiation are minimized. Moreover, we investigate the hydrodynamic interactions between the core particle and the spherical shell using the LPEM technique. In **chapter 4** we investigate the dissolution of various types of spherical silica particles using the LPEM method at the single-particle level in real-time. By optimizing the electron dose rate, we show that an investigation of the chemical reactions such as silica etching at the single-particle level is feasible with the LPEM technique. In **chapter 5** we study the effect of the liquid cell geometry on chemical reactions such as chemical etching occurring inside the liquid cell. Having control over the parameters of the liquid cell electron microscopy, we investigate the etching mechanism of rod-like silica particles with various chemical structures, and we show that by understanding the chemical structure of the rod-like silica particles, it is possible to make from the rods yet another new shape of silica particles. Overall, in this thesis, we develop the LPEM technique to study the physio-chemical properties of complex structured silica nanoparticles aimed at performing self-assembly and switching of the nanoparticles in more using this method as well in future work.

2

Electron beam induced shape-deformation of silica based particles in liquid phase electron microscopy

ABSTRACT

Liquid Phase Electron Microscopy (LPEM) is a rapidly improving technique that utilizes the powerful capabilities of the electron microscope in order to image and investigate liquid-based processes at the nanoscale. However, the presence of the liquid and particles dispersed in the liquid and the high energy electron beam can greatly affect the ongoing processes inside the liquid cell thus the results need to be carefully interpreted. In this chapter I will briefly introduce the transmission electron microscope (TEM), the core instrument used in this thesis, after which I will elaborate on the LPEM technique, following by an explanation of the beam-induced phenomena found in the LPEM experiments on various systems of silica particles studied in this thesis. Silica particles can undergo severe shape deformation upon electron beam irradiation in water. Optimizing the conditions as well as understanding the challenges associated with the act of observation, affecting the nature of the solution, the system of particles, and the dynamic behavior of the particles, is the first step of performing any LPEM experiment with any type of dispersed colloidal particles.

2.1. INTRODUCTION

2.1.1. Transmission Electron Microscopy (TEM)

The defining characteristic feature of colloidal particles is their nano to micron-scale size. There are various ways to characterizing the properties of nanoparticles, however, ‘seeing is believing’, i.e., obtaining detailed real space information about the particles is an important research tool to investigate and help interpret complicated processes directly in real space. Nanoparticles cannot be resolved using conventional light microscopes since they have much smaller dimensions than the typical wavelength of light (ranging from 390 nm to 700 nm). According to the Rayleigh criterion, the corresponding minimum resolvable distance for these wavelengths is 200 nm. (Although we are aware of the super-resolution optical microscopy techniques who are pushing optical microscopy towards true ‘nanoscopy’, these resolutions still cannot match that of an electron microscope [96–102]. De Broglie was the first who theorized about the wave-like nature of the electrons in 1925 [103], and soon after, the first electron microscope was built in 1932 by Ruska and Knoll [104]. In principle the spatial resolution of an electron microscope could be in the sub-atomic distance range as the wavelength of the electrons is only several pms. However, there are other practical limitations which affect the resolution of an electron microscope such as different kind of aberrations of the lenses that are used to focus the electron beam [105]. Nevertheless, the currently available aberration-corrected electron microscopes have a spatial resolution of 50 pm which is several times smaller than the typical distance between atoms [106].

Understanding the electron-matter interaction is the starting point for obtaining extensive information about the material under study. The interactions between the electrons and materials are manifold and include e.g., diffraction, low-angle, and high-angle scattering, X-ray emission, and electron energy losses. In modern TEMs electrons are generated using a field-emission electron source that has a better temporal and spatial coherence and smaller probe size compared to thermionic electron sources [105]. The electrons can be accelerated to different energies to best suit the investigation of the material under study [107]. The accelerated electrons pass through the different electromagnetic lenses and apertures before they hit the sample. The beam characteristics before they reach the sample are defined by the coils located above the sample which are known as condenser lenses, see Figure 2.1. Conventional TEM’s usually contain two condenser lenses (C1 and C2), however modern TEM’s use a third condenser lens C3. Most materials science transmission electron microscopes possess two different imaging modes. A wide, homogeneous, and parallel electron beam results in bright-field TEM imaging mode. It is possible to focus the electron beam into a fine spot known as a ‘probe’ and scan the sample with it. This is known as the scanning transmission electron microscopy (STEM) imaging mode (Figure 2.1). The C3 lens is of great importance in

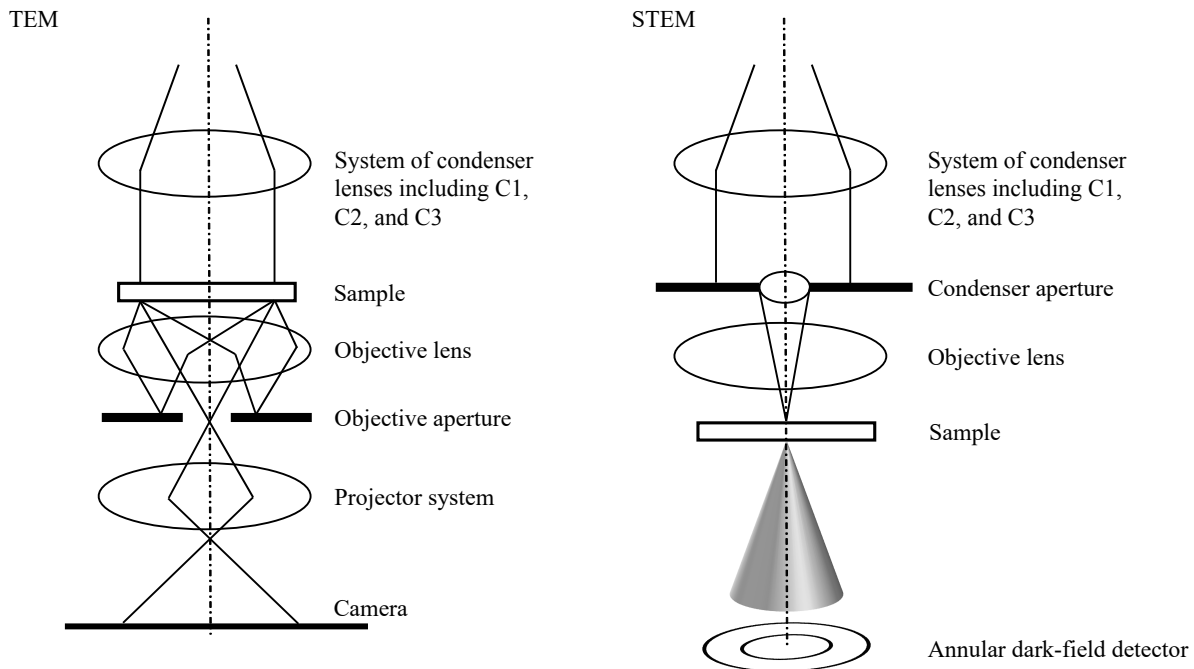


FIGURE 2.1. Ray diagram for bright-field TEM and annular dark-field STEM mode. While in TEM a wide, homogeneous, and parallel electron beam is used to image the sample, in STEM the electron beam is focused to a fine spot that scans the sample to get information.

STEM investigations as it enables attaining a smaller probe size that results in a higher spatial resolution. In TEM, the C3 lens makes the beam parallel to the sample. The ‘spot size’ in the STEM imaging mode, which corresponds to a certain beam current, is tuned by the combination of the C1 lens and the C2 aperture.

When an electron passes through the lenses and apertures and hits the sample, there is a probability of being scattered. In TEM, the sample is typically thin enough (less than 100 nm) compared to the mean free path of the electrons in the material, and most of the electrons pass through it either unaffected and when they do have interactions with the sample, are scattered without loss of energy (elastic scattering). The electrons which do lose part of their energy (inelastic scattering) transfer energy to other quanta, such as X-rays, plasmons, phonons, etc. Each of these signals contains unique information about the sample under study, and depending on the purpose of the study, one can collect the desired information using a proper detector. In TEM imaging mode, depending on the selected detection of electrons with a small scattering semi-angle or those with a high scattering semi-angle, it is possible to perform bright-field (BF) imaging or dark-field (DF) imaging, respectively. In the case of annular dark-field STEM (ADF-STEM) imaging, only the electrons that are scattered elastically over a large angle (larger than 30 mrad) are used.

The electrons scattered as a result of electron-matter interaction pass through a number of lenses before image formation. In BFTEM, objective lenses are used to focus and magnify the electron beam and further magnification is also performed using intermediate lenses, and the projector lens. A metal screen coated with a fluorescent material such as ZnS can be used to form the image. Moreover, it is also possible to record the image by using a charge-coupled device (CCD) camera. Apart from the fact that CCD cameras are inefficient in detecting electrons possessing energies above 20 keV, and that the signal needs to be converted to photons, the main drawback of CCD cameras is the low imaging speed (maximum 30 frames per second). Nowadays, CMOS chip detectors, monolithic active pixel sensors, that are also known as direct detection cameras, are used to perform digital imaging which makes it possible to image at very high frame rates (up to 1600 frames per second) while using very low electron dose rates [108, 109].

As already mentioned, in STEM the beam is focused to a fine spot (50 to 1000 pm wide) known as the ‘probe’, on the sample plane using the C3 lens. The sample is scanned by this probe using deflection coils while the C2 lens is completely turned off. An annular dark-field (ADF) detector is utilized to collect the elastically scattered electrons. The virtual distance between the objective lens and the detector in STEM imaging is known as the ‘camera length’. It is possible to reduce the camera length in order to collect only the electrons which are scattered over at higher angles. This imaging mode is known as a high angle annular dark-field (STEM-HAADF). However, in modern TEMs two distinct detectors are used for ADF and HAADF imaging. Elements with higher atomic number Z scatter the electrons over higher angles. Hence, STEM-HAADF imaging mode is a common technique to reveal the Z-contrast over the sample as the intensity scales approximately with Z^2 [105]. In this thesis, the STEM-HAADF imaging technique was extensively used for liquid cell electron microscopy studies.

2.1.2. Liquid Phase Electron Microscopy (LPEM)

A TEM is a powerful instrument to investigate the various properties of nanoparticles. However, a TEM can be operated only at low pressures (below 10^{-6} mbar). Consequently, the TEM sample needs to be thin, dry materials. There are several disadvantages associated with drying colloidal nanoparticles. Aggregation and collapse due to the surface tension upon drying are common drawbacks of making TEM samples out of colloidal suspensions. Furthermore, there are plenty of liquid-based processes that cannot be studied in a dry state, such as the diffusion of nanoparticles in a liquid, the self-assembly of nanoparticles, chemical reactions in liquids, the operation of batteries, the structure of biological materials in liquid, etc. Although this limitation was recognized from the earliest times in the development of transmission electron microscopy, a practical solution has been achieved only in recent years by the use of

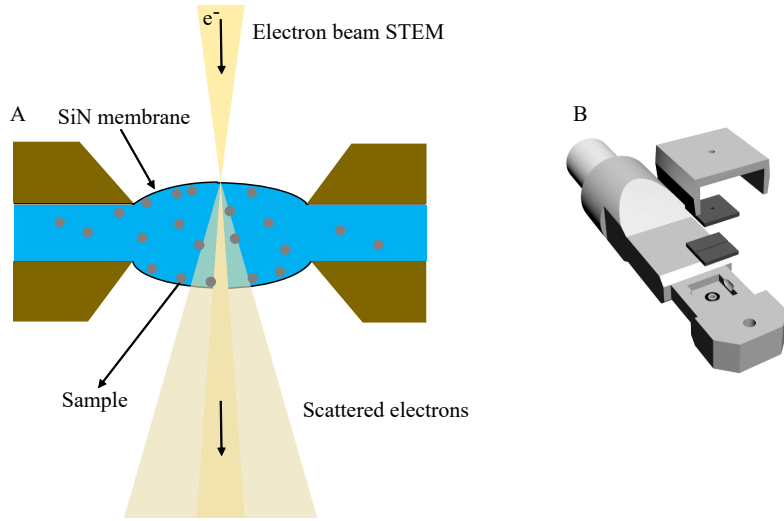


FIGURE 2.2. A) Schematic diagram of a LC-STEM liquid cell. The liquid sample is enclosed between two silicon chips where the electron beam illuminates the electron-transparent silicon nitride ‘window’ consisting of two membranes holding the liquid. The window bulges outward due to the pressure difference between inside and outside of the cell. B) Schematic representation of the tip of the LPEM dedicated holder consisting of the holder tip, silicon chips, and the clamp which keeps the holder vacuum-tight.

modern microfabrication techniques to produce liquid cells with strong but electron-transparent windows. The method which is known as liquid phase electron microscopy (LPEM) or liquid cell (scanning) transmission electron microscopy (LC-(S)TEM) [93–95], has developed rapidly and it is increasingly being used to image liquid-based processes. The liquid cell consists of two chips which are usually made of silicon, containing a tiny electron-transparent silicon nitride (SiN) membrane known as the ‘window’ in the center of the cell (Figure 2.2). The liquid cell chips separate the liquid from the microscope vacuum while they confine the liquid to a layer thin enough that electrons can pass through it. The liquid is sandwiched between the top and bottom chips that are separated from each other by a spacer positioned on the bottom chip. The spacer is either a solid layer with a channel or consists of spherical particles. The thickness of the commercial spacer differs from 100 nm to 5 μm and depending on the sample dimensions an adequate spacer chip should be utilized. In principle, the spacer thickness defines the liquid thickness between the two chips. However, because of the pressure difference between the interior of the cell (atmosphere pressure) and the outside of the cell (i.e. the microscope column pressure; 10^{-6} mbar), the windows bulge outward. This results in a liquid thickness in the middle of the cell of at least 2 to 3 μm which reduces the spatial resolution in LC-TEM dramatically. The decrease in the resolution is due to multiple scattering of electrons in both the SiN window and the liquid layer. In LC-STEM it has been shown that the resolution when focusing

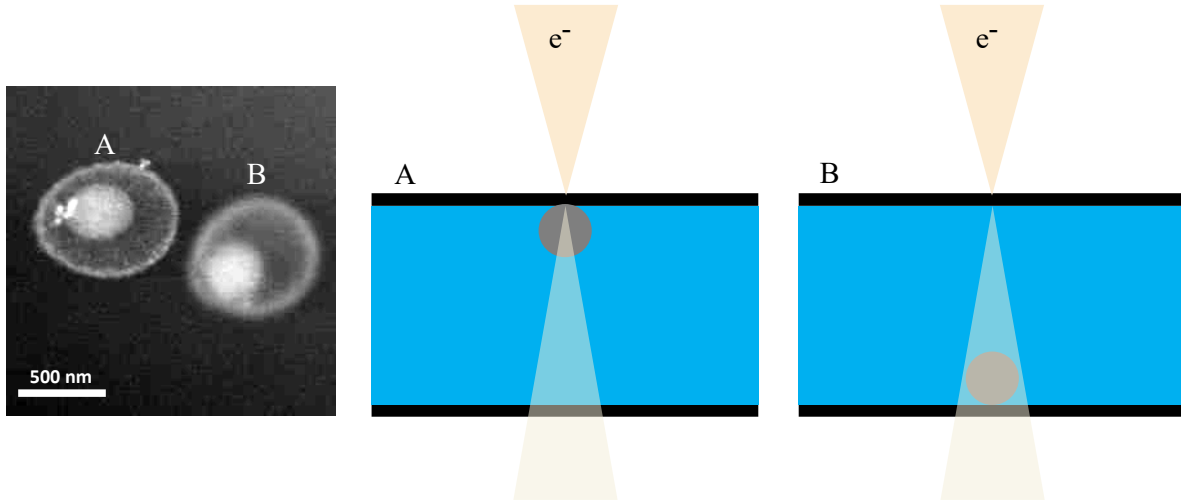


FIGURE 2.3. The resolution difference between two rattle particles in the same LC. A) particle on the top window, B) particle on the bottom window. The resolution on the top window is noise-limited while for the bottom window it is related to the beam broadening due to multiple scattering events. The water thickness is $2 \mu\text{m}$.

the beam on the top window is noise-limited and that inelastic scattering and multiple scattering can be neglected when the particle is on the top window (on top of a liquid layer) [110]. On the other hand, LC-STEM imaging on the bottom window is not noise-limited. Instead, the resolution is limited by the broadening of the electron probe by scattering events in the liquid layer before it reaches the bottom window [110] (Figure 2.3).

Nevertheless, high-resolution LC-(S)TEM imaging can be achieved using thin materials such as graphene as liquid cell [111–114]. Apart from the investigations of the different properties of nanomaterials in liquids, with recent developments in LC holders and in micro-electromechanical systems (MEMS) technology, it is also possible to incorporate additional functionalities such as flowing the liquid inside the cell, applying electric fields using electrodes, and heating the liquid inside the cell using dedicated heating LC chips. Despite the great improvements of the LC-(S)TEM technique, there are still substantial limitations that should be considered when performing and interpreting the LC-(S)TEM studies. The two main limitations are the electron beam effects and the geometry of the liquid cell, which may change the conditions of the *in-situ* experiments compared to their *ex-situ* counterparts. In this thesis, we extensively study the effects of the electron beam and the geometrical differences, and we focused on optimizing the LC(S)TEM conditions to study the physio-chemical properties of silica based particles.

2.2. EXPERIMENTAL

2.2.1. Materials

Tetraethyl Orthosilicate (TEOS, 99%, Sigma-Aldrich), Absolute ethanol (Merk), MilliQ water (Millipore system), Sodium citrate (Sigma-Aldrich), Chloroauric acid (ACS reagent), Polyvinylpyrrolidone (PVP, Average Mw 10000 g.mol⁻¹), Ammonia (ACS reagent, 28-30 w% NH₃ basis, Sigma-Aldrich).

2.2.2. Particle synthesis

The rattle particles were synthesized by the selective removal of a sacrificial layer; a polystyrene layer was grown around the Stöber particle (the core), followed by growth an outer silica shell, after which the particles were heated at 500 °C for four hours in the air to remove the sacrificial polystyrene layer a temperature at which the silica does not yet fully condense its siloxane structure [115]. To make the rattle particles fully condensed, they were heated to 900 °C (5 °C.min⁻¹) for three hours [115–119]. Next, the sample was allowed to cool down to room temperature overnight. The particles were redispersed in deionized water (Millipore system). The detailed synthesis procedure can be found in Ref. [120].

The Au-Si core-shell particles were synthesized in a multi-step synthesis procedure. First, 15 nm gold cores were synthesized using the Turkevic method [121]. 10 mL water was added to 0.10 g chloroauric acid and 0.10 g sodium citrate in two separate vials to obtain 1.0% (w/v) gold and citrate stock solutions. Next, 300 mL water and 3.0 mL of the 1.0% (w/v) gold solution were transferred to a two or three-necked round-bottomed flask equipped with a condenser. The flask was heated by a heating mantle until boiling under 600 rpm stirring. 9.0 mL of the 1.0% (w/v) sodium citrate solution was added as soon as the solution was clearly boiling. The solution color gradually changed in time from blue to deep red indicating the formation of gold nanoparticles. Boiling continued for 15 minutes and then the solution was cooled down to room temperature. Subsequently, the gold particles were transferred to ethanol to grow a Stöber silica shell around them. To this end, first, the gold particles were coated by polyvinylpyrrolidone (PVP) to be stable in ethanol [122]. To 5.0 mL of gold nanoparticle solution, 120.0 μL of a 10.0% w/v PVP solution (1.0 g in 10.0 mL water) was added under constant stirring. The solution was left to be stirred for 12 hours. After 12 hours, the solution was centrifuged 15 minutes at 15000 *g* in 5 mL Eppendorf tubes. Then the water was removed carefully using a glass pipet and the particles were redispersed in an equal amount of ethanol. The sample was sonicated for 1 minute for homogenization. The procedure was continued by transferring 5.0 mL of PVP stabilized gold nanoparticles in ethanol to a vial and adding 500.0 μL of ammonia to this solution under constant stirring. 50.0 μL of 10.0 vol% TEOS in ethanol was added to the solution after 1 minute. The addition of 10.0 vol% TEOS was repeated every 90 minutes. This was

done in 3 steps and a total amount of 350.0 μL of 10.0 vol% TEOS was added during the synthesis procedure. The volume of the added 10.0 vol% TEOS was doubled after every addition and the reaction was finished 90 minutes after the last addition.

2.2.3. In-situ liquid cell STEM

All in-situ experiments were performed using a Hummingbird Scientific, (USA) liquid cell dedicated holder with corresponding microchips. The liquid sample was prepared by sandwiching the dispersion between two silicon microchips (Hummingbird Scientific, USA) with 50 nm thick amorphous silicon nitride (SiN) electron-transparent windows with a size of 50 by 200 μm . Depending on the particle size a proper spacer chip was used. For silica rattle particles with a diameter of 800 nm, a chip with a 1 μm spacer was used. The spacer used for 100 nm Au-Si core-shell nanoparticles and 120 nm Stöber silica nanoparticles was 100 nm. Prior to sample loading, the two silicon chips were glow-discharged for 2 minutes to remove organic contamination and to make their surfaces more hydrophilic. For each in-situ experiment, the microchip with the spacer was first placed at the tip of the holder. A 1 μL droplet of the desired particles dispersed in water (Millipore system) dropped cast on the microchip. Next, the top chip was placed on the spacer chip with the hydrophilic side facing the opposite chip and the excess liquid was removed with filter paper, after which the windows were carefully aligned. A syringe pump equipped with a 1 mL glass syringe was used to flow water into the cell. The in-situ experiments were performed using a Tecnai-F20, (Thermo Fisher Scientific) (S)TEM, equipped with a field emission gun operating at 200 kV. A high angle annular dark-field (HAADF) detector at a 120 mm camera length was used to continuously capture image series. In order to calculate the electron dose rate the beam current in vacuum was measured for each spot size and the resulting electron dose rate was calculated by dividing the beam current by the total frame size as follows [123]:

$$d = \frac{I_e}{eA} \quad (2.1)$$

Here d is the electron dose rate, I_e is the beam current, e is the elementary charge, and A is the total frame size determined by the magnification.

For expansion-and-shrinkage experiments after recording the image series, a Gaussian blur (2 pixels) was applied over the images to reduce the noise and the particle size in each frame was measured using the particle size analysis plug-in in ImageJ.

2.3. RESULTS AND DISCUSSION

In conventional transmission electron microscopy, the electron beam irradiation damage has been extensively studied [124]. The beam damage in the vacuum can be classified into electronic damage and knock-on damage. Electronic damage includes

electrostatic charging, and ionization, while knock-on damage includes atomic displacements, structural damage, and mass loss [124]. In liquid phase electron microscopy the presence of a liquid results in a more severe electron beam irradiation damage, as there are additional processes occurring in the liquid layer itself which changes the chemistry of the suspending medium dramatically. Generation of molecular and radical species as well as hydrated electrons and pH changes caused by electron beam irradiation are some of these effects [125]. These “indirect” effects of the electron beam irradiation along with the “direct” effects such as charging, and bond-breaking at and/or in the particles, should be carefully considered when performing and analyzing LC-(S)TEM experiments. In order to study the physio-chemical properties of silica particles and their self-assembly in water, we first need to elucidate the electron beam effects on silica particles in LC-STEM measurements. Hence, we performed LC-STEM experiments on various types of silica particles. We analyzed the beam-induced shape-deformation of silica particles in water. We made use of these results to optimize the LC-STEM conditions to perform in-situ experiments where the electron beam effects were minimized. In subsequent sections, we will elaborate on some of the electron beam irradiation effects on various systems of silica particles studied in this thesis.

2.3.1. Expansion, and shrinkage of silica nanoparticles

Electron beam irradiation of silica particles in vacuum increases the mass density and makes the silica structure stronger as it becomes fully condensed [126]. Studies show that the silica particles undergo a volume reduction by 15–18% upon electron beam irradiation [126], which is similar to heating the same particles above 850 °C which can also fully condense the siloxane structure [115–119]. Nevertheless, the presence of water during electron beam irradiation can change the out of equilibrium boundary conditions and hereby dramatically change the observed results. For instance, electron beam induced products may affect the silica particles. Moreover, because of the presence of water, the hydrolysis of siloxane bonds becomes feasible, next to condensation reactions.

In this section, we investigate the electron beam irradiation effects on silica rattle particles when water is present. The particles were heat-treated to 500 °C for four hours during the synthesis procedure, as mentioned before this temperature does burn away the polymeric material, but does not yet fully condense the siloxane structure of Stöber silica [115]. The observations showed that the silica particles first undergo an expansion and subsequently a shrinkage process upon electron beam irradiation in the presence of water. The change in diameter in the expansion stage was found to depend on the internal structure of the silica particles as well as the electron dose rate. For silica rattle particles (see section 1.3.4) which were heat-treated at 500 °C for four hours during the synthesis procedure, the shell expansion was found to be 2–3%. The

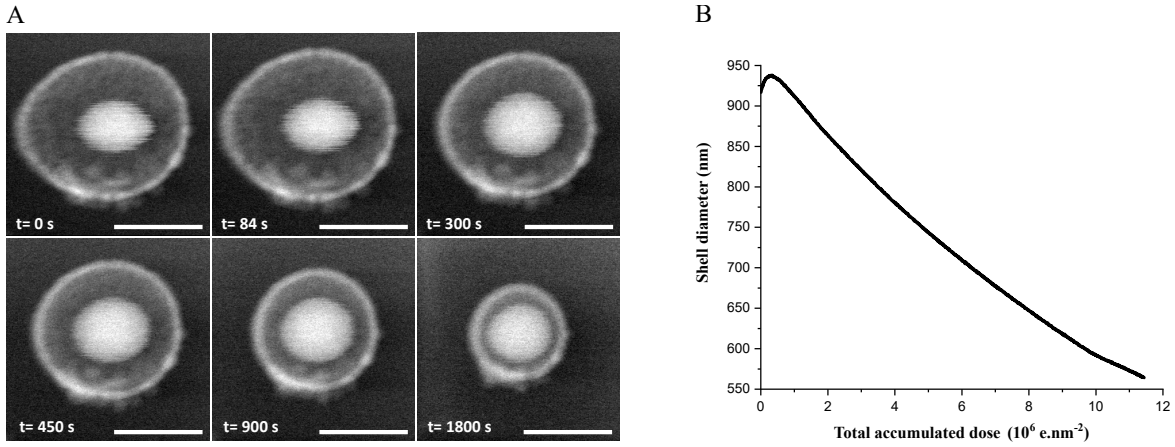


FIGURE 2.4. Expansion-and-shrinkage process of silica rattle particle in water upon electron beam irradiation (electron dose rate: $6.4 \times 10^3 \text{ e}^{-\text{nm}}^{-2}\text{s}^{-1}$, total number of frames: 3600, frame time: 0.5 s, water flow: $5.0 \mu\text{L}\cdot\text{min}^{-1}$). A) Stills of a HAADF-STEM recording showing the expansion-and-shrinkage process of the rattle particle in real-time. B) Shell diameter as a function of the total accumulated electron dose. The total number of frames is 3600 frames. The frame time is 0.5 seconds. The scale bar indicates 500 nm.

shell expansion occurred at the very beginning of the electron beam irradiation with an electron dose rate of $6.3 \times 10^3 \text{ e}^{-\text{nm}}^{-2}\text{s}^{-1}$ where after 84 seconds of irradiation the shell reached its maximum diameter size (second frame in Figure 2.4), which accounts for an increase in shell diameter of 2% (20 nm for this particular shell). Subsequently, the shell started to shrink while being continuously exposed to the electron beam at the same electron dose rate, and this shrinkage continued until the shell closely surrounded the core particle (Figure 2.4).

In another LC-STEM experiment, we used silica rattles which had been previously heated to 900 °C for three hours. It is known that silica condensation occurs upon heating up to 1000 °C [116]. By heating silica rattle particles up to 900 °C for 3 hours they were fully condensed (100% Q^4) [115–119] and upon exposure to the electron beam in water the shell diameter increased up to approximately 10%, which is 75 nm for this particular particle. This is a rather severe increase in the shell diameter compared to the previous 2-3% (Figure 2.5). This strongly suggests that a decrease in density occurred in the silica structure under the electron beam irradiation in the presence of water, which lead to the initial expansion of the particle. This can be explained by the hypothesis that the broken siloxane bonds react with water, and as a result, the density of silica particle decreased. In these experiments, we flowed water into the cell with a flow rate of $5.0 \mu\text{L}\cdot\text{min}^{-1}$. Thus, the dissolved silica was carried away by water flow. The reduction in density is greater for a fully condensed particle (heated to 900 °C) compared to a partially condensed one (heated to 500 °C), which resulted in a bigger

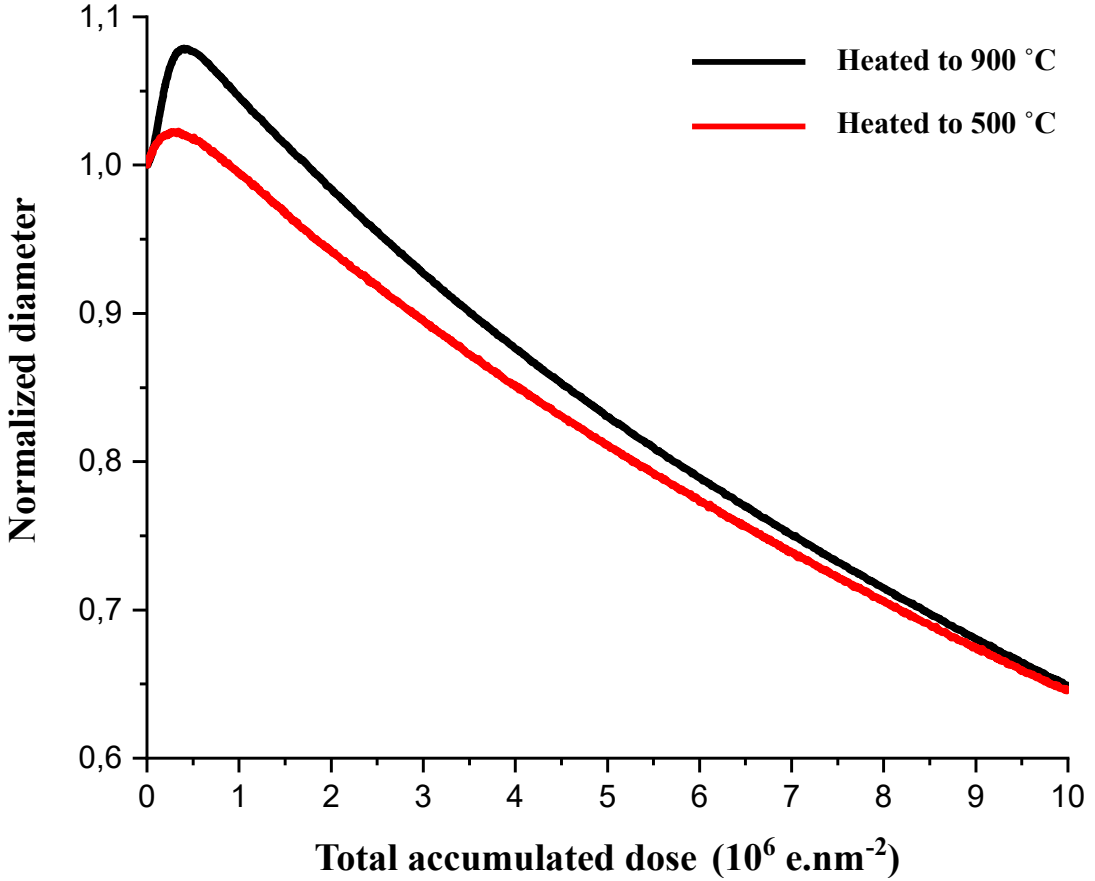


FIGURE 2.5. Comparison of the shell expansion for a fully condensed particle heated to 900 °C for three hours, and a partially condensed particle heated to 500 °C for four hours.

shell expansion for the fully condensed particle. Eventually, the continuous electron beam irradiation resulted in further bond-breaking which lead in the presence of water to loss of material and shrinkage of the silica shell by dissolution.

The decrease in density by silica dissolution can be also observed in the Stöber silica core particle where the contrast of the particle decreased upon electron beam irradiation. Figure 2.6 shows a silica particle with an initial diameter of 120 nm. As we mentioned in a previous section the contrast generation in STEM measurements is due to mass contrast. Since the silica particle is composed of the same elements, the particle thickness and density determine the observed brightness. Therefore, the decrease in the pixel intensity during the electron beam irradiation indicates that the particle converts from a higher density structure to a lower density structure with fewer siloxane bonds. It is also clear that during the electron beam irradiation the particle expanded and became smoother which is most likely due to material restructuring as

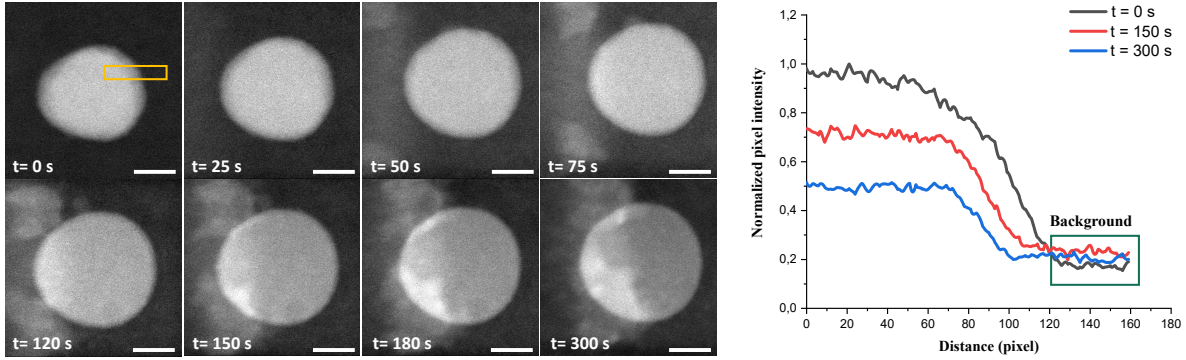


FIGURE 2.6. The decrease in contrast during the electron beam irradiation of a 120 nm silica nanoparticle in water. The yellow box shows the distance for which the intensity profile is plotted. The intensity profile is plotted for exposure times $t = 0$ s, $t = 150$ s, and $t = 300$ s. The background pixel intensity in all frames is the same indicating that the particle mass density decreased in time. Water was not flowed during this experiment. The scale bar indicates 50 nm.

well. Additionally, the LC-STEM observations showed that a certain amount of silica was deposited on the SiN window as well as on the silica particle itself. This is most likely due to continuous bond breaking to the point that the silicon atoms or silicate oligomers were completely disconnected from the silica matrix and redeposited on the SiN window or the silica particle. It has been shown that silica redeposition is strongly related to electron beam irradiation [127]. In this experiment, we didn't flow water into the cell and the redeposited silica was detectable as a light haze in the field of view. The dissolved silica can be partially carried away by flowing liquid through the cell. It is noteworthy that the flow rate above the window in the present cells used in this work was not completely known. However, with recent developments in the commercial LC holders, a more controlled liquid flow is attainable using a pressure based-liquid pump where the liquid only passes through the cell window and not the whole cell.

Another interesting observation that was made from the LC-STEM experiments on the silica rattle particles is that the silica shell maintained its spherical shape during the expansion as well as shrinkage. This implies that during the shape deformation the silica particle may have high plasticity. Zheng *et al.* [128] showed that brittle amorphous silica nanoparticles become ductile upon low-intensity electron beam irradiation. They explained that the high energy electron beam generates structural and bonding defects throughout the silica particle, which increases the flexibility by facilitating bond-switching events [128]. This can be also applied to our system where the electron beam continuously breaks the bonds and allowed the material to restructure, which partially

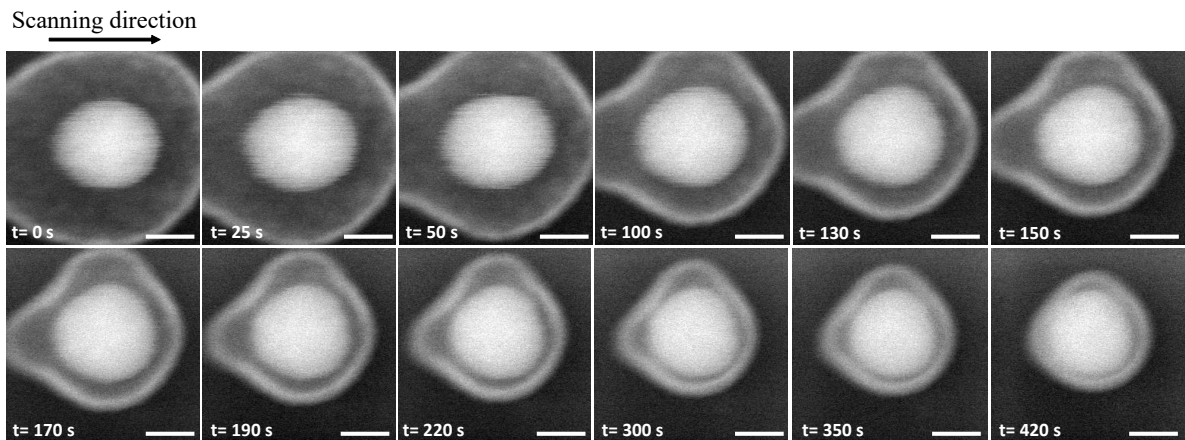


FIGURE 2.7. Electron beam irradiation of the rattle particle in water (electron dose rate: $3.2 \times 10^3 \text{ e}^- \text{nm}^{-2}\text{s}^{-1}$, frame time: 0.5 s, water flow: $5.0 \mu\text{L}\cdot\text{min}^{-1}$). Only the parts which are in the field of view undergo the shape deformation which results in a Mickey Mouse shaped particle. This indicates the importance of the direct effect of the electron beam irradiation on the silica shape deformation. The scale bar indicates 200 nm.

explains the fact that the spherical shell maintained its shape during the expansion-and-shrinkage processes. However, a full understanding of this reshaping is not yet there and most likely will also need an approach in which this process is simulated. Moreover, the LC-STEM observations showed that the expansion-and-shrinkage processes only occurred for the particles present in the field of view, in other words when they were irradiated by the electron beam. Figure 2.7 shows a rattle particle that was partially placed in the field of view. Upon electron beam irradiation the parts of the particle that were in the field of view shrunk while the parts placed out of the field of view did not which resulted in a ‘Mickey Mouse’ shaped particle after shrinking.

It is noteworthy that the silica expansion-and-shrinkage processes occurred at electron dose rates above $10^3 \text{ e}^- \text{nm}^{-2}\text{s}^{-1}$, which is the conventional electron dose rate used in most of the LC-(S)TEM literature and also similar to dose rates used in imaging nanoparticles in TEM without a liquid present. The electron beam irradiation can either directly break the bonds through radiolysis, or it can indirectly affect the particle system by generating different reactive species in the suspending medium (water in this case). The effect of the electron dose rate as well as the accumulated electron dose on LC-STEM experiments of silica nanoparticles was extensively studied in Chapter 4. These results show the complicated and out-of-equilibrium nature of LC-STEM experiments which should be carefully considered when performing such experiments.

2.3.2. Anisotropic shape deformation of silica nanoparticles

An elongation of spherical silica particles in the scanning direction was observed during LC-STEM measurements on these. Figure 2.8 shows a few image series of Au-Si

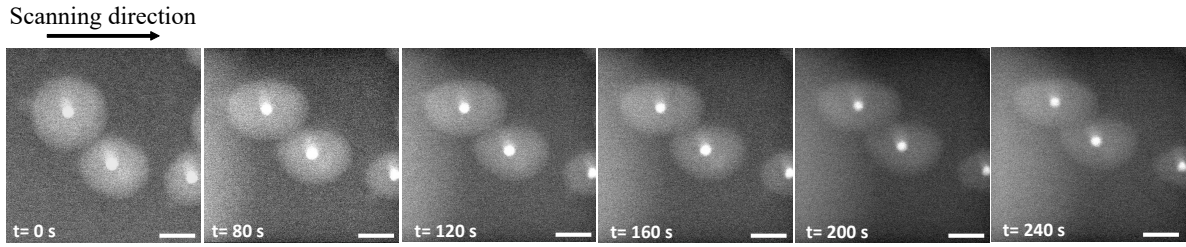


FIGURE 2.8. Electron beam irradiation of the Au-Si core-shell particles in water (electron dose rate: $17 \times 10^3 \text{ e}^- \text{nm}^{-2} \text{s}^{-1}$, frame rate: 0.5 s, water flow: $5.0 \mu\text{L} \cdot \text{min}^{-1}$). The elongation of the silica particles occurred along the scanning direction. The scale bar indicates 50 nm.

core-shell nanoparticles elongation under electron beam irradiation. Here, the scanning direction was from left to right, starting from the top left corner. The elongation of the silica particles was found to be in the scanning direction. The presence of the Au core particle, which remained spherical during the electron beam irradiation, indicates that the anisotropic shape change only occurred in the silica particles and the observed effect is not due to beam misalignment. The electron dose rate used in this experiment was extremely high ($17 \times 10^3 \text{ e}^- \text{nm}^{-2} \text{s}^{-1}$). The enhanced plasticity of the silica particles by electron beam irradiation [128] was already mentioned in the previous section where the silica rattle particle maintained its shape during the severe expansion-and-shrinkage process. However, plastic deformation cannot explain the fact that the elongation occurs in the scanning direction.

It was previously reported that silica nano-spheres with a diameter of 53 nm, elongate along the scanning direction upon electron beam irradiation in water in LC-STEM [129]. The authors suggested a dissolution-precipitation model for the elongation of the silica nanoparticles and explained that the dissolved silica redeposited at the sides of the nanoparticles in the scanning direction of the electron beam, resulting in ellipsoidal silica nanoparticles. In another study, a rapid elongation of silica rattle particle in the scanning direction was reported where the silica shape changed rapidly by changing the scanning direction of the electron beam [130]. The rapid silica particle deformation where the particle elongated in the scanning direction immediately after changing the scanning direction cannot be explained by the dissolution/precipitation model, although the dissolution and the redeposition of the silica were definitely occurring during the electron beam irradiation as it was observable as a light haze on the LC window. Alternatively, the silica particle elongation may be related to the beam-induced electric fields and accumulated charges [131]. Using a randomly patterned electron beam might reveal more about the mechanism of the electron beam induced anisotropic shape deformation and is planned in future work.

2.4. CONCLUSION

The intriguing observations of nanoscale processes in real-time using the LPFM technique, provide important insights in various fields of science where liquid-based processes are concerned. However, the physical and chemical processes can be strongly altered by the high energy electron beam and the peculiar liquid cell geometry, also for electron dose rates used in ‘regular’ observation of nanoparticles. We studied the effect of the electron beam irradiation on various systems of silica particles in water. Heat-treated rattle particles undergo an expansion-and-shrinkage process upon electron beam irradiation with electron dose rates above $10^3 \text{ e}^- \text{nm}^{-2} \text{s}^{-1}$. The particle diameter initially increased upon electron beam irradiation, most clearly exhibited by the shell, while subsequently, the shell diameter decreased drastically until it closely surrounded the core particle. The spherical shape of the particle was maintained during the expansion-and-shrinkage process indicating the high flexibility of the silica particle under electron beam irradiation. Furthermore, the observations showed that only the particles in the field of view underwent the shape deformation indicating that the effect of the electron beam was essential. Comparing the LCSTEM results to electron beam irradiation of silica particles in the dry state revealed that the presence of water is crucial for the expansion of silica particles as the only shrinkage occurs in dry state upon electron beam irradiation. Moreover, using gold core silica shell particles we observed elongation of the silica particle along the scanning direction upon electron beam irradiation in water. The elongation only occurred in the silica particle and the gold particle remained spherical during the electron beam irradiation. This could be due to the higher plasticity of the silica particle under electron beam irradiation or to the charging effects of the electron beam. However, these hypotheses cannot fully explain why the elongation occurs in the scanning direction. In order to understand the underlying mechanism of silica elongation along the scanning direction, further experiments should be designed and compared with numerical simulation of the processes taking place. In the case of high energy ($\sim \text{MeV}$), ion irradiation of silica particles with beams of charged ions such numerical investigations have already successfully performed [132, 133]. For instance, using a randomly patterned electron beam where the scanning direction is not simply from left to right might result in a different type of shape deformation.

2.5. ACKNOWLEDGEMENTS

The authors wish to thank Wessel Vlug for performing additional liquid cell measurements. We thank Albert Grau Carbonell for critical reading of the chapter. The authors also acknowledge the EM square center at Utrecht University for access to the microscopes.

3

Liquid cell scanning transmission electron microscopy study of diffusion of colloidal particles inside spherical shells

ABSTRACT

A novel type of colloidal particle known as a rattle or yolk-shell particles were used to study the diffusion of a particle inside a spherical shell. The study was carried out using liquid cell scanning transmission electron microscopy (LC-(S)TEM) at the single-particle level. The 3D diffusive trajectories of the particles were tracked in a 2D projected form using image analysis. Subsequently, the tracks were analyzed to investigate the electrostatic and hydrodynamic interactions between the core and the shell. We found that in water, increasing the electron dose rate made the core particle approach the shell more closely, and finally became attached to it. Among multiple effects of the electron beam that could explain this observation, the effect of the increase in ionic strength is most likely not the most significant as we did not extensively deionize our systems, instead we think a change of surface charge associated with pH change is more likely the main cause. Furthermore, we used glycerol carbonate as a more viscous polar liquid with a polarity higher than water, to slow down the diffusion of the core particle in order to do further quantitative analysis. The hydrodynamic interactions between the core and the shell slowed down the particle as it approached the shell. We showed that the diffusion inside spherical confinement is asymmetrical and should be decoupled into two diffusion coefficients in the radial and perpendicular directions. The radial diffusion coefficient decreased as the core particle became closer to the

shell, which can partly be attributed to insufficient time resolution, while the perpendicular diffusion coefficient stayed constant within most of the shell. We found that the mobility of the silica core particle did not change significantly when increasing the electron dose rate for both shell sizes whereas it decreased for titania core particle. We also showed that the diffusion coefficient is larger for the particles diffusing within bigger shells.

3.1. INTRODUCTION

The physical properties of colloids are of considerable interest due to their widespread technological applications [134–136]. Developments in making novel model particle systems structured on multiple lengths scale [55, 56, 69, 83, 84, 137, 138], along with new advanced experimental techniques to study their static and dynamic properties, are providing for new opportunities for more fundamental and applied science using these new particle systems and techniques [139–142]. Fluctuations in the momenta of the solvent molecules that continuously collide with the particle give rise to Brownian motion and this may be discussed in terms of a diffusion coefficient D for particles,

$$D = \frac{k_B T}{f} \quad (3.1)$$

where k_B is the Boltzmann constant, T is the absolute temperature, and f is the friction coefficient of the particle in the solvent. Due to the diffusion of the colloidal particles and the too good approximation incompressibility of liquids the solvent liquid has to flow with a stick boundary condition around the particle, which in turn results in a hydrodynamic drag on the particle. The friction coefficient is the ratio of the drag force \vec{F} and the particle velocity \vec{v} . For a single, isolated, spherical particle in a large reservoir of liquid the motion of the particle in three dimensions, having a velocity v , produces a drag force given by the Stokes formula: [143]

$$\vec{F} = -6\pi\eta a \vec{v} \quad (3.2)$$

where η is the solvent viscosity and a is the particle radius. Relating the drag force to the thermal fluctuations yields the Stokes-Einstein equation which was when derived independently by Sutherland [144] and Einstein [10] the first example of what is now called ‘fluctuation-dissipation’ relationships:

$$D = \frac{k_B T}{6\pi\eta a} \quad (3.3)$$

The free diffusion of particles has been extensively studied and is well understood. Over the past decades, the study of diffusion has shifted towards diffusion in complicated geometries. A classical problem is the characterization of the motion of a single colloidal particle near a flat wall, which has been explored experimentally, [145–147] theoretically, [148, 149], and by computer simulations [150]. The diffusion of a particle placed between two parallel planar walls has also been studied [151–153]. The presence of the wall in these cases leads to a modified hydrodynamic drag on the particle due to the flow restriction by the wall. Furthermore, the wall breaks the symmetry around the particle resulting in the diffusion and as a consequence, the diffusion coefficient becoming anisotropic with different values in different directions depending on the symmetry of the problem, in the case of a flat wall: one parallel and one perpendicular to the wall, where both components depend on the separation distance between the particle

and the wall. The studies have shown that the diffusion constants both in parallel and perpendicular directions to the wall decrease as the particle becomes closer to the wall due to the hydrodynamic interactions as a manifestation of the stick boundary condition of the flow at the surface of the wall [146]. The hydrodynamic coupling is the highest when the particle is closest to the wall [154]. In the case of the diffusion of a particle between two parallel planar walls, the motion of the particle is already slower in the middle of two walls compared to free diffusion, due to hydrodynamic coupling between the particle and the walls [152]. Recently more complicated geometries, such as those of a cylindrical or spherical cavity, where the particle is confined from all sides, have gained attention as well. Eral *et al.* [155] showed that the diffusion coefficient of colloidal particles in the center of a closed cylindrical cavity, with both the height and the radius size equal to 9 particle diameters, is 0.75 of the diffusion coefficient D_0 measured in the bulk the same liquid. They also showed that the diffusion inside a closed cylindrical cavity is asymmetrical and that there is a transition region of about 3 particle diameters wide in which the radial D_r and azimuthal D_θ components of the anisotropic diffusion coefficients decrease to respective values of $0.1D_0$ and $0.4D_0$. This is in agreement with the results from computer simulations of the hydrodynamics of a spherical particle entrapped in a closed cylinder [156]. In another paper by Cervantes-Martínez *et al.* [157] they experimentally investigated the diffusion of a $1\text{ }\mu\text{m}$ fluorescent polystyrene spheres entrapped in $6.35\text{ }\mu\text{m}$ spherical water droplets immersed in oil and they showed that the radial diffusion D_r (towards the liquid-liquid interface) slowed down near the wall, however, the perpendicular diffusion D_p (along the curved surface) remained virtually unchanged except close to contact with the interface. The perpendicular diffusion only decreased beyond the equilibrium liquid-liquid interface as the liquid-liquid interface used in this study was deformable, and most likely also does not have a zero velocity at the liquid-liquid interface, resulting in quite different boundary conditions compared to our work where the spherical confinement was a rigid silica shell. We will explain in more detail the particle systems used in this work in subsequent paragraphs. Recently a thorough theoretical study was carried out on diffusion inside a spherical cavity by modeling the behavior of a concentrated colloidal dispersion in such 3D confinements, [158] which provides useful quantitative insights on how the radial and perpendicular diffusion coefficients change due to hydrodynamic interactions in spherical cavities as a function of the geometry. The study shows that 3D confinement breaks the symmetry of the drag on the diffusing particle and gives rise to the anisotropic hindrance of both the radial and perpendicular diffusion components to a different extent. Further, it shows that the diffusion of a confined particle depends on its proximity to the cavity wall and it is maximum at the center of the cavity while it gradually decreases as it becomes closer to the cavity surface. For instance, for the particle-to-cavity size ratio $a/R = 0.2$ the particle in the middle has a diffusion

coefficient of approximately 60% of that of a freely diffusing particle, and when the particle is placed at position $r/R = 0.5$ (r/R is 0 when the core is in the middle and 1 when the core touches the shell) the diffusion coefficient drops to 40% of that of a freely diffusing particle. The diffusion fades entirely at particle-wall contact, which is a direct consequence of the stick boundary condition at the wall. Another important result shown in this study is that the perpendicular diffusion remains above 90% of its value in the middle of the spherical geometry until the core particle is really close to the shell wall ($r/R = 0.85$).

In 2003 Xia and coworkers [159] popularized a type of colloidal particles with a movable core inside a spherical shell. Particles diffusing inside the spherical shell of pollen were already studied as long ago as by Brown, but to make such systems deliberately to be used in model studies and/or applications in advanced materials has become popular only in this century [54–58]. These particles which are known as “rattle” particles or “yolk-shell” particles have a purposely designed core@void@shell geometry. As these particles consist of a core particle entrapped inside a rigid spherical shell, they are an ideal model system to experimentally study the diffusion of colloidal particles in spherical confined geometry and/or to be used in advanced e.g. photonic applications [120]. These rattle particles can be synthesized with a wide range of materials, particle sizes, shapes, and structures [54,55,69,120]. Because of its excellent mechanical, chemical, thermal stability, transparency for visible light, and bio-compatibility, tunable porosity, silica is a promising material to produce rattle particles [74, 120, 160]. Using silica as a negatively charged material in neutral pH conditions [161] to make the shell part of rattle particles, makes it necessary if the stability of the movable core is induced by charge interactions to also be negatively charged if the ionic strength is sufficiently low. The electrostatic repulsion besides the hydrodynamic interactions described above should be considered during the analysis of the core mobility inside the confining spherical shell. Here we used two different rattle particles, $\text{TiO}_2@\text{void}@\text{SiO}_2$ and $\text{SiO}_2@\text{void}@\text{SiO}_2$, to study the diffusion of the core particle inside the spherical shell. In both cases, the core and the shell were negatively charged.

The interaction potential between two charged spherical particles can be approximated via DLVO theory: [17–19]

$$U = U_{vdw} + U_{es}, \quad (3.4)$$

where

$$U_{vdw} = -\frac{A}{3} \left(\frac{a_1 a_2}{r^2 - (a_1 + a_2)^2} + \frac{a_1 a_2}{r^2 - (a_1 - a_2)^2} + \frac{1}{2} \text{Log} \left[\frac{r^2 - (a_1 + a_2)^2}{r^2 - (a_1 - a_2)^2} \right] \right) \quad (3.5)$$

and

$$U_{es} = \lambda_b \frac{Q_1 Q_2}{(1 + \kappa a_1)(1 + \kappa a_2)} \frac{e^{-\kappa(r-a_1-a_2)}}{r}. \quad (3.6)$$

With the Bjerrum length, λ_B , defined as:

$$\lambda_B = \frac{e^2}{4\pi\epsilon_0\epsilon_m k_B T}. \quad (3.7)$$

Here A is the Hamaker constant of the material of the colloidal particle interacting through the liquid it is dispersed in with another colloidal particle, a_1 the radius of the core, a_2 the radius of the shell, r the center-to-center distance, Q is the number of charges, κ is the inverse Debye screening length, e is the elementary charge, ϵ_0 is the permittivity of the vacuum, ϵ_m is the dielectric constant of the medium.

However, the different geometry of rattle particles where a charged particle has electrostatic interactions with a charged shell makes the interaction potential calculations different than the case of the DLVO theory for two charged spherical particles and we are not aware of analytical approximations/solutions for this geometry, although it is not too difficult to numerically solve the Poisson-Boltzmann equations e.g. using Comsol, for this geometry. The interaction potential for a rattle particle is still to be studied and explained. However, the important parameter in the DLVO theory in this respect is the Debye screening length, κ^{-1} , which mainly determines the repulsion range inside the shell and is related to the ion concentration (ionic strength) is for monovalent ions via:

$$\kappa = \sqrt{\frac{2N_A c e^2}{\epsilon_0 \epsilon_m k_B T}} \quad (3.8)$$

where N_A is Avogadro's number, and c is the ion concentration in the bulk. The range of the Debye screening length determines how close the core can get to the shell. The ions screen the charges around the charged object and reduce the length of the electrostatic potential thus making the repulsion shorter ranged. This region is known as the 'electric double layer'.

Liquid-cell (scanning) transmission electron microscopy [94, 95] (LC(S)TEM), which is starting to become a powerful in-situ electron microscopy technique, provides the opportunity of observing and recording dynamic processes of colloidal particles in liquids. In principle, LC-(S)TEM is a new high-resolution method to analyze the diffusion of colloidal nanoparticles in confining spherical shells with high spatial resolution, be it that the analysis is necessarily a 2D projection of a 3D diffusional process. However, the high energy electron beam can significantly affect the diffusion of the particles under study. So far, the far majority of published diffusion studies of colloidal particles in LC-(S)TEM have focused on an extremely slowed down diffusion of particles (3-8 orders of magnitude slower than theoretical predictions) often in studies where effects of the electron beam induced could not be excluded [123, 160, 162–183]. For instance, de Jonge and coworkers [123] proposed that in their study of Au particles with a diameter of 30 nm and stabilized by thiolated chitosan (TCHIT) there is a highly viscous ordered liquid layer exhibiting a viscosity 5 orders of magnitude larger than a bulk liquid

near the LC window, which led to a dramatic slowing down of the particle diffusion of the particles close to the windows of the liquid cell. Other explanations include hydrodynamic hindrance near a wall [166, 169] and strong (beam-induced) interactions with the LC windows [123, 163, 166, 169, 171]. Or a combination of these effects where attractions make the particles reside stuck onto the wall while they can still undergo a kind of stick-slip process moving over the surface. In this explanation, no anomalous viscosity is needed to explain the extreme slowing down of the particles compared to free diffusion. Using rattle-type particles enabled us to record the diffusion of the core particle while the shell was attached to the LC wall in a way where the core particle was not influenced by the window allowing us to find the conditions in which the effects of the electron beam could be neglected. In this study, we investigated the diffusion of core particles inside spherical shells using a low dose scanning transmission electron microscopy (STEM) technique combined with a viscous liquid medium to slow down the movement of the core particle for further analysis. Finding the conditions to observe the diffusion of particles using the LC-(S)TEM method would allow us to explore in future work experiments such as studies on self-assembly of colloidal particles [184]. Moreover, it serves as a powerful new technique to study the diffusion of colloidal particles in liquids at a single particle level with a high spatial resolution which subsequently helps to better understand the diffusion of colloidal particles in more complicated confining geometries. Additionally, if fully understood the diffusional motion of the particles inside the porous silica shells could also be used in more complicated liquid cell experiments as a local probe for the temperature and/or ionic strength.

3.2. EXPERIMENTAL

3.2.1. In-situ liquid cell STEM

All in-situ experiments were performed using a Hummingbird Scientific, (USA) liquid cell dedicated holder with corresponding microchips. The liquid sample was prepared by sandwiching the dispersion between two silicon microchips (Hummingbird Scientific, USA) with 50 nm thick amorphous silicon nitride (SiN) electron-transparent windows with a size of 50 by 200 μm . A spacer of 500 nm on the bottom chip separates the top and bottom chips. However, the pressure difference between inside and outside the cell when the holder is inserted in the microscope makes the windows bulge outwards resulting in a bigger separation between the top and bottom chips thus a thicker liquid layer (for liquid thickness determination see Chapter 5). Prior to sample loading, the two silicon chips were glow-discharged for 2 minutes to remove organic contamination and to make their surfaces more hydrophilic. For each in-situ experiment, the microchip with the spacer was first placed at the tip of the holder. A 1 μL droplet of the desired particles dispersed in water (Millipore system) or glycerol carbonate (4-(Hydroxymethyl)-1,3-dioxolan-2-one, Sigma-Aldrich 455067) dropped cast on the microchip. Next, the top

chip was placed on the spacer chip with the hydrophilic side facing the opposite chip and the excess liquid was removed with filter paper, after which the windows were carefully aligned. For the experiments that were carried out in the water, a syringe pump equipped with a 1 mL glass syringe was used to flow solutions into the cell. However, when glycerol carbonate was used as the solvent for particles, no liquid was flowed during the experiment due to the high viscosity of glycerol carbonate ($\eta = 0.147 \text{ Pa}\cdot\text{s}$). It should be realized that there is a small uncertainty in the viscosity due to the possibility of there being some water present within glycerol carbonate therefore it is a good strategy for hygroscopic liquids to add a certain amount of water (e.g. 5%). The in-situ experiments were performed in a Tecnai-F20, (Thermo Fisher Scientific) (S)TEM, equipped with a field emission gun, operating at 200 kV. An annular dark-field detector (ADF, E.A. Fischione Instruments Inc., Model 3000, USA) with a 120 mm camera length was used to continuously capture image series to produce movies of the diffusion of the particles. The frame times in all experiments were either 0.2 or 0.5 seconds. The electron dose rate was calculated as mentioned in Chapter 2, section 2.2.3.

3.2.2. Particle tracking and analysis

We used a published algorithm by John Crocker and David Grier for the fitting and tracking of particles in 2D electron microscopy images using IDL Version 8.3 [185]. Prior to tracking, a Gaussian blur (2 pixels) was applied over the image to reduce the noise using ImageJ (Fiji version). By inserting the particle size in pixels in the code, the center of the particle was identified. After identifying all particle positions in all frames it was tracked in time by looking for the particle in the next frame within a certain maximum displacement which is defined for the software as the distance from particle's previous position.

Next, when the x and y coordinates of the particle were determined in all frames we performed the analysis using Wolfram Mathematica software version 11.1 to obtain the analytical data to study the diffusion of a core particle in a confined spherical shell.

The displacements between frames were split into a radial component and a component perpendicular to the radial direction. This resulted in radial and perpendicular displacements in time steps of 0.2 s. These displacements were categorized to be in a certain part of the shell by the average position of the particle between the two frames. For the part of the shell geometry under investigation, a histogram of displacements for both directions was made with a bin size of 10 nm. The width of the distribution was translated to a radial and perpendicular diffusion coefficient D_r and D_p using $D_i = \frac{\sigma_i^2}{2t}$, where σ_i is the width of the Gaussian fit for the radial or perpendicular displacements and t is the timestep of 0.2 s.

3.2.3. Finite element calculations

In order to model the hydrodynamic slowing down of a core particle within the shell geometry, we performed finite element calculations using the COMSOL 5.4 MultiPhysics Modeling Software. We set up a system with a spherical colloid of radius $R = 170$ nm (no-slip boundary condition) within a no-slip shell of varying radius, depending on the particles in the experiments. The spherical shell, including the core particle and liquid, was placed within a cylindrical domain with open boundary conditions (zero normal stress) for the fluid. We solved Stokes' equations for an incompressible fluid. The fluid density was taken as $\rho = 1.4 \times 10^3$ kg m⁻³ and the dynamic viscosity used was $\eta = 0.147$ kg m⁻¹ s⁻¹ in accordance with the experimental parameters. We solved for the force exerted by the fluid and the shell wall on the sphere. We applied a constant velocity boundary condition to obtain the translational mobility. To ensure that the laminar flow condition is satisfied, a low velocity of the sphere was used: $v = 10^{-6}$ m s⁻¹. This typically resulted in a Reynolds number $Re < 10^{-2}$. We varied the position of the sphere inside the shell to determine the radial position dependence on mobility. Furthermore, we changed the direction of the velocity boundary condition on the core particle to decouple the hydrodynamic slowing down of the mobility towards the shell and along with the shell. Whenever possible, we exploited the rotational symmetry of the system to minimize the number of elements required, i.e. when the velocity boundary condition was directed towards the shell. When the velocity boundary condition was directed along with the shell, a full 3D calculation was required. Constructing a sufficiently small mesh was only feasible when local refinement of the elements on the surface of the core particle was used. Generally, an element size of 2 nm was employed on the surface of the core particle and the element size was allowed to grow radially outward. We performed mesh refinement for a few selected calculations and found no significant difference for even smaller element sizes.

3.3. RESULTS AND DISCUSSION

In order to study the diffusion of colloidal particles in spherical shells a novel type of colloidal particles known as rattle particles were used (Figure 3.1). Although the emergence of the synthesized rattle particles is quite recent, in Chapter 1 we mentioned that Brown used the Pollens particles and the motion of the micron-sized particles inside like a yolk-shell system [7]. Rattle particles enabled us to record the movement of a core particle within a shell at the single-particle level at a convenient time scale while the shell is attached to the SiN window of the LC. In this study, we used rattle particles with different silica shell sizes (small being 800 nm, and big being 1100 nm) as well as different core materials with different zeta potentials (silica and titania) as they have both different pH dependencies and different refractive indexes and thus Hamaker constants. We used water and glycerol carbonate as a solvent for these

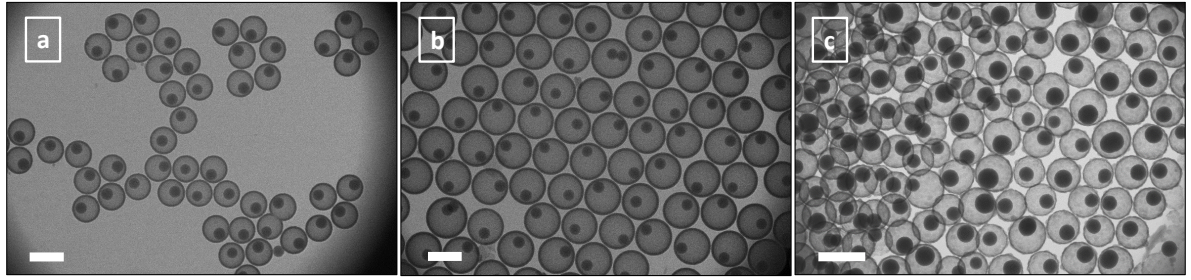


FIGURE 3.1. Transmission electron microscopy (TEM) images of rattle-type particles: (a) silica core diameter $d_{core} = 340$ nm, the void diameter $d_{void} = 740$ nm (b) silica core diameter $d_{core} = 340$ nm, the void diameter $d_{void} = 990$ nm (c) titania core diameter $d_{core} = 350$ nm, the void diameter $d_{void} = 690$ nm. The scale bar indicates $1 \mu\text{m}$

particles. Using two different solvents allowed us to investigate the effect of the viscosity and the interactions on the mobility of these particles, and finding the optimized LC experimental conditions to study the diffusion of colloidal particles within a spherical shell. We used a published particle identification/tracking code to study the direct electrostatic interactions as well as the indirect hydrodynamic interactions between the core and the shell which depends on the core position inside the shell along with the cavity geometry. As mentioned, the diffusional process in the shells is 3D, but we can only analyze a 2D projection of this process in LC work which introduces errors and/or deviations that we tried to correct for by numerical calculations of the frictions factors in full 3D shells. We also qualitatively investigated the effect of the electron dose rate on the interaction potential inside the shell and the diffusivity of the core particle.

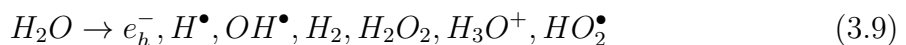
3.3.1. Rattles in water: Electrostatic repulsion under electron beam irradiation

Initially, rattle particles with a titania core and a silica shell were used to investigate the interaction potential between a core and a shell in water. The dispersion was enclosed between two silicon microchips with 50 nm thick electron-transparent amorphous silicon nitride (SiN) windows. The chips were loaded on a dedicated TEM holder and inserted in the electron microscope. Water was flowed at a rate of $2 \mu\text{L}\cdot\text{min}^{-1}$ during the measurements. Since the mobility of the core inside the shell can be strongly influenced by the strength and even more importantly the range of electrostatic interactions, the effect of the electron beam was found to be quite prominent. Hence, to analyze the effect of the electron beam on the electrostatic repulsion between the core and the shell, we performed LC-STEM experiments at various electron dose rates.

The free diffusion coefficient of 340 nm spherical particles in water is $1.45 \times 10^6 \text{ nm}^2\cdot\text{s}^{-1}$, which makes tracking and quantitative analysis almost impossible with currently available scanning speeds. For instance, for the minimum available frame time in our

microscope (0.2 s), a 340 nm spherical particle diffuses $2.9 \times 10^5 \text{ nm}^2$ in water in a single frame. However, it is still feasible to analyze the data qualitatively and roughly find out how close the core particle can come to the shell in water. This was done by taking the maximum intensity of pixels in each frame and making a superposition of all frames of the same movie, which then showed the area in which the particle moved over many frames. Figure 3.2a shows a single LC-STEM image whereas figure 3.2b shows the area the particle displacements averaged in over 255 frames. The core feels electrostatic repulsion as it approached the shell due to the electric double layer overlap. By measuring the minimum distance between the particle and the shell over long periods (such as Figure 3.2b), a measure for the distance at which the core feels repulsion from the shell was obtained for various electron dose rates. It is also clear from Figure 3.2 that the rattle particles were elongated in the scanning direction to a small extend which was due to the high accumulated electron dose ($0.6 \times 10^6 \text{ e}^- \text{ nm}^{-2}$) used to record these frames (see Chapter 2). Figure 3.3 shows the relationship between the electron dose rate and the minimum separation distance between the core and the shell. The results show that by increasing the electron dose rate the minimum separation distance between the core and the shell decreased. For instance, by increasing the electron dose rate from 90 to $160 \text{ e}^- \text{ nm}^{-2} \text{ s}^{-1}$ the minimum separation distance decreased from 85 to 75 nm. At elevated electron dose rates ($\sim > 300 \text{ e}^- \text{ nm}^{-2} \text{ s}^{-1}$) some of the particles become attached to the shell (Figure 3.4). A corresponding movie for the titania core getting attached to the shell at higher magnifications (electron dose rates higher than $\sim > 300 \text{ e}^- \text{ nm}^{-2} \text{ s}^{-1}$) can be found in supporting movie 1. We attempted to understand this finding by looking at electron-solvent interactions.

Schneider *et al* [125] devised a model to model electron-solvent interactions. Upon the interaction of an incident electron with an individual water molecule, the transferred energy from the electron to the molecule excites its orbital electrons. This causes the decomposition of the water molecule into a few species, including hydrated (solvated) electrons e_h^- , hydrogen radicals H^\bullet , hydroxyl radicals OH^\bullet , and hydrogen gas H_2 where the subsequent reaction of these products yields the primary products as follows: [125]



In this way, the electron-water interactions resulted in an increase in the ion concentrations and thus the ionic strength. It is important to remark though that these simulations of the effects of the electron beam in water were done in pure solvent and that is almost certain that details will be (possibly) strongly affected by what also happens within and/or on the particles by the electron beam, which is not taken into account. However, it is still safe to conclude that the ionic strength also if the presence of the particles was fully taken into account would increase. Because of the porous

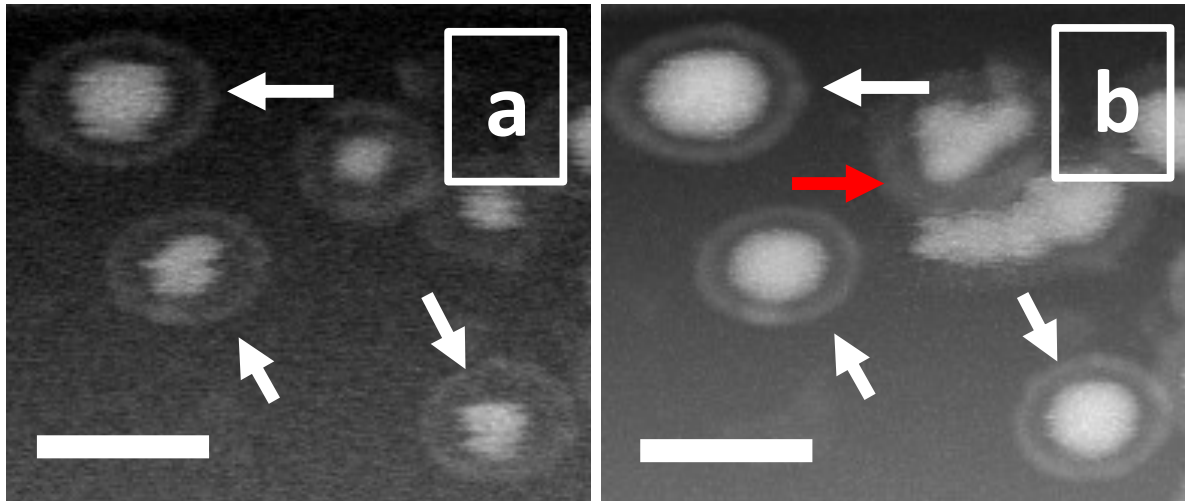


FIGURE 3.2. LC-STEM measurements on rattle-type particles with a titania core and silica shell in water. (a) A single frame of 0.5 s of the recorded HAADF-STEM movie. (b) A superposition of 255 frames of the same movie, showing how close the core particles can get to the shell. During the imaging process, some particles detached and diffused away from the imaging area, while some other particles diffused in the imaging area and attached to the window. That is the reason for differences appeared in the area which is indicated by a red arrow. The scale bar indicates $1 \mu\text{m}$

structure through which also the inner shell was removed [120] of the shell we assume that ions can pass through it so that the ionic strength inside and outside the shell was equalized. By screening the surface charge with ions, one can tune the Debye length and thus the repulsion-free region inside the shell. As already described, the ionic strength, or ion concentration c (mol m^{-3}) is related to the Debye screening length κ^{-1} via equation 3.8. The calculations of the interaction potential between two charged spherical particles using DLVO theory show that by increasing the ionic strength they become closer to each other. After reaching a certain distance which is close enough for the van der Waals attraction forces to become the dominant interaction, the potential becomes attractive. We calculated the increase in ionic strength in our system according to the code from Schneider *et al.* [125]. It should be noted that the calculation from Schneider *et al.* [125] was done for homogeneous electron beam irradiation for solvent only, so not taking into account the particles as mentioned, which obviously is not the case in our system, where a focused electron beam scans over the sample. However, it still provides important insights for the interpretation of the LC-STEM observations. The calculations show that an increase in ion concentration for the electron dose rate interval of our LC-STEM experiments ranges between 5×10^{-3} mM to 28×10^{-3} mM (Figure 3.5a). The ionic strength of deionized water if no precautions are taken to exclude the dissolution of CO_2 can become as high as 10^{-3} mM [186–188]. This means

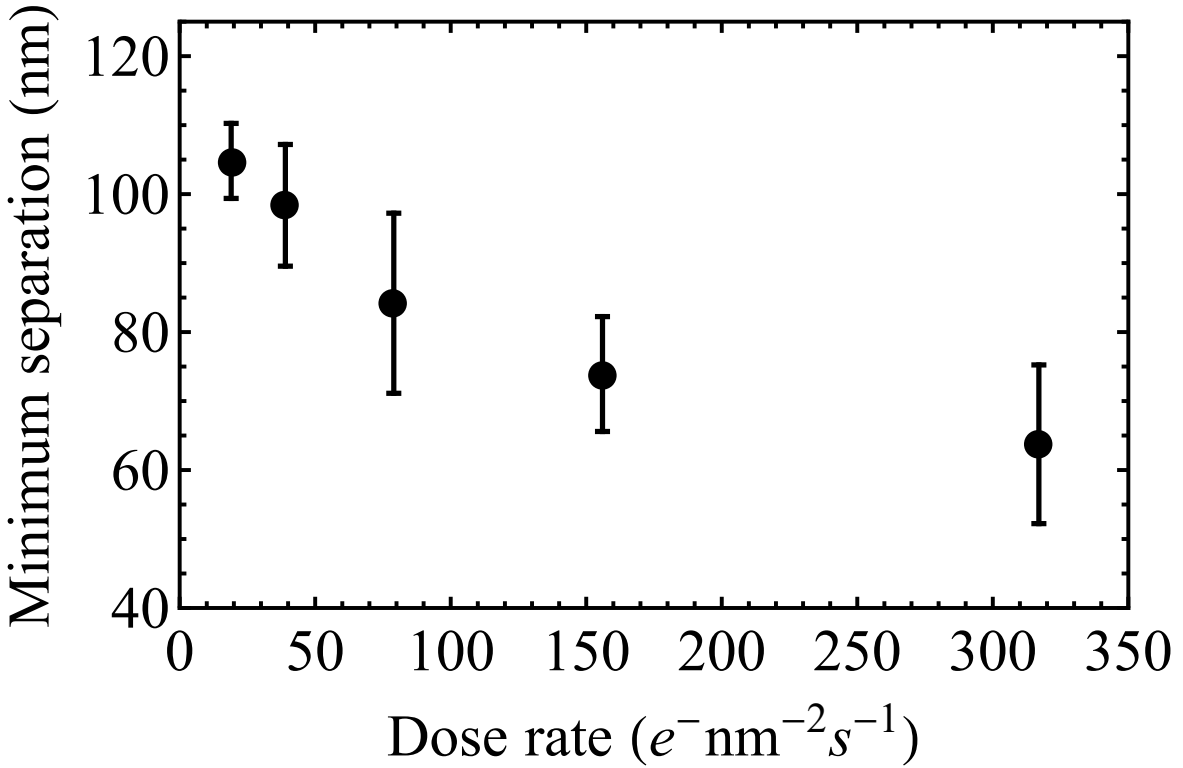


FIGURE 3.3. The minimum separation distance between the titania core and the silica shell as measured for various electron dose rate conditions. The particle position over several frames (>10) was averaged to determine how close the core particle could move to the shell. The closest distance from the shell is a measure for when the core particle feels a repulsive force from the shell.

that the increase in ionic strength for our system is perhaps not that significant and the change in Debye screening length κ^{-1} is relatively small. This would have been quite different if we would have precluded CO₂ dissolution, e.g. by working under an inert atmosphere like the group of Palberg pioneered [186, 187]. Again, we also do not know the amounts of ions released from the particles as well, which most likely cannot be neglected. These reactions might also affect what happens to the pH. Therefore, the change in ionic strength can probably not the main effect that explains our observations, although such effects should always be considered in LC-(S)TEM experiments and clearly need to take into account modellation of the presence of the particles as well in future work.

The relationship between the separation distance and the ionic strength dependence of the interaction potential may not be the only factor affecting the LC-STEM observations. Increasing the electron dose rate not only increases the ion concentration but also caused differences in the charging of the silica surfaces [189] and/or a change in the pH which would change the surface charge on the core and the shell as well. The presence

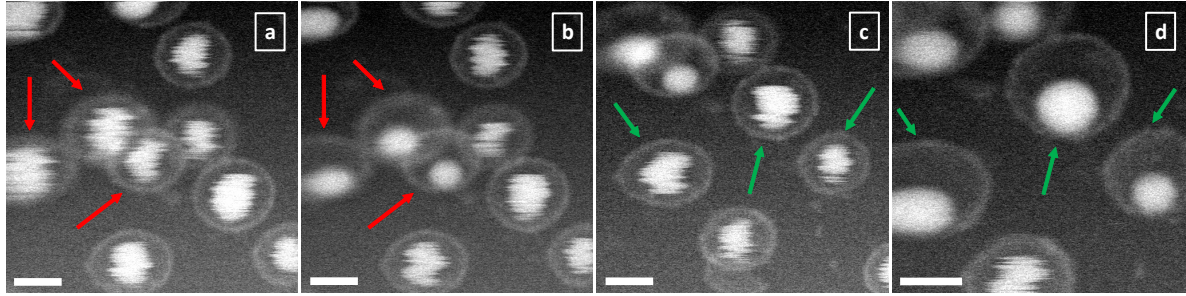


FIGURE 3.4. LCSTEM measurements on rattle-type particles with a titania core and silica shell in the water at increasing magnification and electron dose rate, until they eventually get attached to the shell. (a) Single frame directly after increasing the magnification, when the electron dose rate becomes $317 \text{ e}^- \text{nm}^{-2} \text{s}^{-1}$. At dose rates lower than this, the particles did not get attached to the shell. b) A single frame at the same magnification and electron dose rate as (a), but 2 seconds later. Three particles on the left side of the frame got attached to the shell. (c) A single frame at the same magnification and electron dose rate as (a) and (b), but 20 seconds after frame (b). The particles that were moving in (b) are still moving in (c), indicating the equilibrium ion concentration is reached quickly upon increasing magnification. (d) A single frame, taken directly after increasing the magnification from (c). The electron dose rate is now $634 \text{ e}^- \text{nm}^{-2} \text{s}^{-1}$. The core particles that were moving got attached to the shell within a single frame. The scale bars indicate 500 nm

of H_3O^+ in the electron beam irradiation radiolysis products influences the solution's pH [125], but again the chemistry of the electrons and the silica is not included in this reasoning. The charge on the surface of the negatively charged colloidal particles decreases when the solution pH goes down [189]. The lower surface charge might have resulted in a decreased repulsion between the core and the shell, and a large decrease in the surface charge (due to pH changes) could have to lead the core particle to get attached to the shell.

To better understand the effect of pH on the interaction potential between the core and the shell we estimated the pH of water upon electron beam irradiation for the electron dose rates which we used in these experiments according to the calculation code from Schneider *et al.* [125]. The results show that the drop in pH for an electron dose rate of $640 \text{ e}^- \text{nm}^{-2} \text{s}^{-1}$ – where we observed the attaching of the core particle to the shell within a single frame (Figure 3.4) – would be from the initial pH of 7 for water to 4.8 (Figure 3.5b). This drop of pH upon electron beam irradiation would be significant. Around pH 4 to 5, silica is minimally stable (zeta potential of around -20 mV) [189], however for now too much is not known to know for sure what the change in pH actually was, as also the dissolved CO_2 will be affected by the electron irradiation, next to the effects on the particle itself. For all these reasons there are

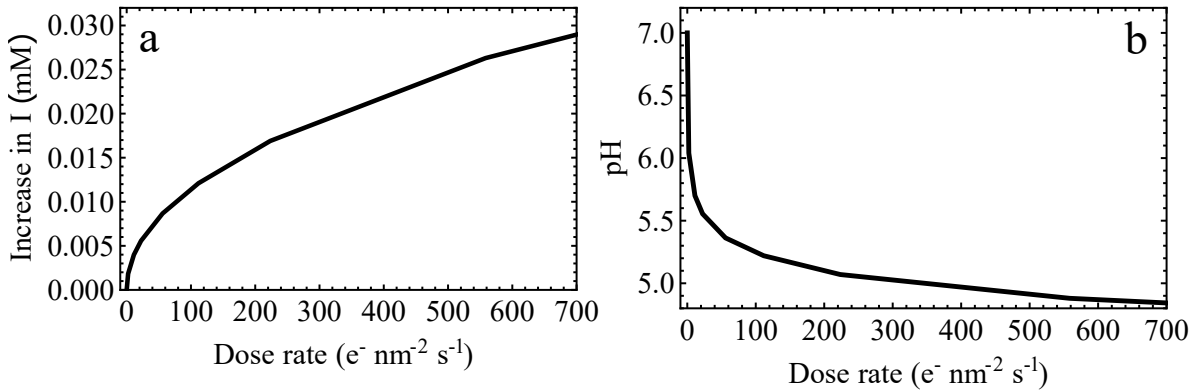


FIGURE 3.5. Calculated (a) ion concentration increase and (b) pH versus electron dose rate. These values are calculated via the homogeneous model of Schneider *et al.* However, as mentioned the presence of the particles is not taken into account. [125]

even opposite effects on pH indicated of silica particles dispersed in water as caused by electron irradiation [127, 129]. We reach this regime using conventional electron dose rates reported in the literature. The effect may be even more severe in STEM mode due to local strong irradiation of the sample. Therefore, using low-dose imaging conditions in LC-(S)TEM experiments to observe the diffusion of particles is important. Moreover, Figure 3.5b shows that the drop in pH is highest when the electron dose rate slightly increases whereas the rate of the pH drop decreases when increasing the electron dose rate. Thus it is important to account for the effect of the potential pH change when interpreting liquid phase electron microscopy results. Overall by analyzing the effect of ionic strength as well as pH change upon electron beam irradiation it can be concluded that the pH change is most likely a more important parameter in the attaching of the core particle to the shell than the increase in ionic strength. However, direct charging effects by the beam hitting the core particle cannot be excluded, just as other chemical transformations as caused by the bond breaking. Multiple effects likely contribute to the core becoming unstable.

3.3.2. Rattles in glycerol carbonate: Mobility of a core particle within a spherical shell

In order to perform a more quantitative study on the diffusion of colloidal particles within a confined spherical shell using LC-STEM, the core particle needs to be tracked. As already mentioned, the high diffusivity of the core in water makes tracking and analysis almost impossible with current scanning speeds. For this reason, we used glycerol carbonate, a medium with higher viscosity ($\eta = 0.147 \text{ Pa}\cdot\text{s}$) as the solvent for rattle particles where the free diffusion of particles is slowed down to $8.7 \times 10^3 \text{ nm}^2\cdot\text{s}^{-1}$. Along with a higher viscosity compared to water, glycerol carbonate has other advantages for LC-STEM experiments as well. A high dielectric constant ($\epsilon =$

111.5) which may reduce the charging effects of the electron beam, together with low vapor pressure, make glycerol carbonate a promising solvent for LC-(S)TEM studies. It is noteworthy that using low electron dose rates is extremely important when glycerol carbonate is used as the solvent since higher electron dose rates ($\sim > 600 \text{ e}^- \text{nm}^{-2} \text{s}^{-1}$) were found to cause bubble formation, caused by either dissolved gasses and/or a decomposition reaction during the scanning which subsequently results in a dry liquid cell. The rattle particles were redispersed in glycerol carbonate, which slowed them down, such that we could observe their motion within the temporal resolution available. The LC sample was prepared using the same procedure of sample preparation for an aqueous dispersion by enclosing the glycerol carbonate dispersion between two silicon microchips with 50 nm thick electron-transparent amorphous silicon nitride (SiN) windows. No liquid was flowed during the experiment. The dynamics of particles were recorded using LC-STEM.

In our system, the diffusion coefficient of the core particle will be different at every point within the geometry. The two factors that influence the diffusion coefficient are the proximity of the core particle to the shell wall, as well as the direction the particle is moving in. Due to the symmetry of the system, the diffusion coefficient can be split into a component in the radial direction as well as a component that is perpendicular to that and along the shell wall. We used these two components in section 3.3.3. However, in the middle of the shell, neither of these two components should yet be significantly different from one another, which means we can use 1 diffusion coefficient to describe the diffusion in the middle of the spherical geometry ($r/R = 0$).

Another complication arises from the fact that the microscope data are a 2D projection of a 3D system. This means that the diffusion coefficient we obtained from the experiments is an average of all diffusion coefficients at various z heights within the system.

We performed finite element calculations to estimate the error that is introduced by not knowing the z coordinate in our experiments. We placed the core particle at various z and r coordinates and gave it a velocity in the radial direction or the direction perpendicular to that. The r coordinates range from 0 to 60 nm as we took this to be the middle of the shell in the experimental analysis (see Figure 3.6b). The z coordinate ranges from 0 to 120 nm from the center for the small shell, and from 0 to 200 nm for the large shell. This is based on how close the core particle can approach the shell in the x and y directions in the experiments. We assumed that this is the same in the z direction. To calculate the diffusion coefficient we expect to find in the projected data, we averaged the diffusion coefficients for all r and z values. Here we assumed that there is no potential in this region and it is thus equally likely to find the particle on all those positions.

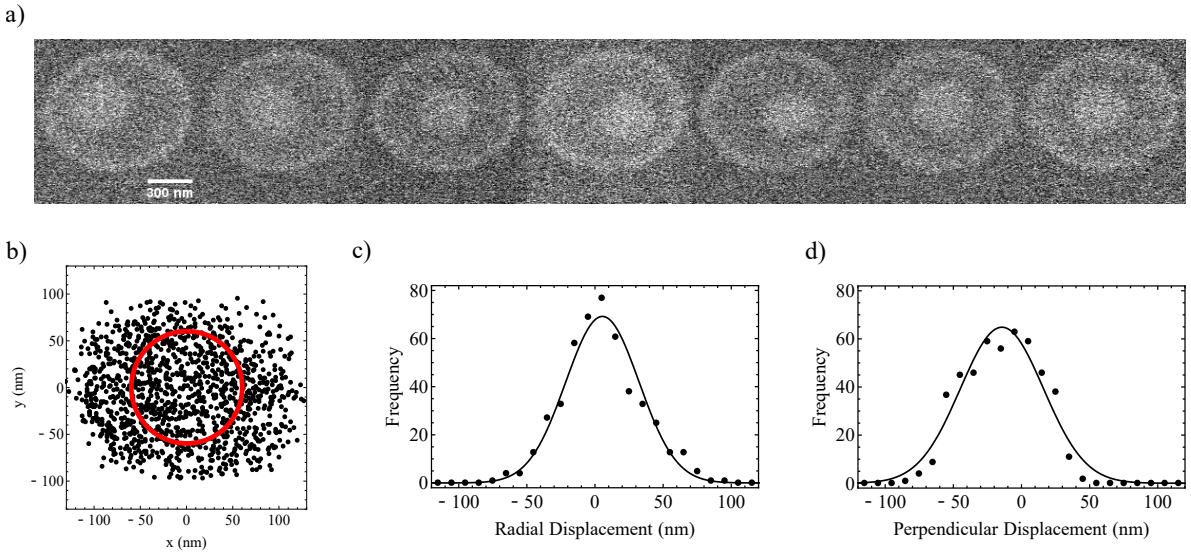


FIGURE 3.6. Mobility of a rattle-type particle with a silica core and small silica shell (Figure 1a) in GC. The electron dose rate is $66 \text{ e}^-\text{nm}^{-2}\text{s}^{-1}$. (a) consecutive frames of a HAADF-STEM movie of a silica core and small silica shell rattle-type particle. The time between each frame is 0.2 s. b) Positions where the core particle is found at over the duration of the acquired movie. The points inside the red circle (radius 60 nm) were used for the analysis to represent the diffusion coefficient in the middle of the shell. (c) Displacements of the core particle in the radial direction between frames of 0.2 s. (d) Displacements of the core particle in the perpendicular direction between frames of 0.2 s.

For the small shell, we found that the diffusion coefficient for the particle in the middle of the small shell should theoretically be 18% of the free diffusion coefficient, which leads to a theoretical diffusion coefficient of $1.5 \times 10^3 \text{ nm}^2\text{s}^{-1}$. However, if we average all the diffusion coefficients we obtain between $0 < r < 60 \text{ nm}$ and $0 < z < 120 \text{ nm}$, we expect to find a diffusion coefficient that is 16% of the free diffusion coefficient, which is $D = 1.4 \times 10^3 \text{ nm}^2\text{s}^{-1}$. This is therefore the value we expect to find in the experiments.

For the large shell, we found that the diffusion coefficient for the particle in the middle of the small shell should theoretically be 33% of the free diffusion coefficient, which leads to a theoretical diffusion coefficient of $2.8 \times 10^3 \text{ nm}^2\text{s}^{-1}$. However, if we average all the diffusion coefficients we get between $0 < r < 60 \text{ nm}$ and $0 < z < 200 \text{ nm}$, we expect to find a diffusion coefficient that is 31% of the free diffusion coefficient, which is $D = 2.6 \times 10^3 \text{ nm}^2\text{s}^{-1}$, which is the value we expect to find in the experiments.

The error in the diffusion coefficient introduced by averaging in the z direction for the particle in the middle area of the projected shell is less than 10% for both the small

and large shells. Our projected data from the experiments should therefore still give a reasonable value for the diffusion coefficient of the particle in the middle of the shell.

Figure 3.6a shows frames of a video recorded with a HAADF-detector of a rattle particle with a silica core and a silica shell in glycerol carbonate. The particles could be tracked and its mobility can be investigated at an extremely low electron dose rate ($< 100 \text{ e}^- \text{nm}^{-2}\text{s}^{-1}$). The tracking was done using a particle identification and tracking computer code in IDL [185]. The positions of the core particle are shown in Figure 3.6b. The histogram of radial and perpendicular displacements between frames obtained by tracking are shown in Figure 3.6c and 3.6d respectively. The width of the distribution gives information about the diffusion coefficient D of the particle. The broader the distribution, the higher the mobility of the particle. The standard deviation σ of a Gaussian curve is used to quantify the 1-dimensional mobility of the core particle in the radial or perpendicular direction via: [143, 190]

$$D = \frac{\sigma^2}{2t} \quad (3.10)$$

where t is the time between frames.

Influence of the electron dose rate and core material on mobility

First, we investigated the core mobility within the spherical geometry as a function of core material and electron dose rate. For this part particles with a titania core or silica core within a silica shell were used, while the size and the geometry of the rattle particles were similar.

Figure 3.7a shows the relationship between the electron dose rate and the mobility for titania core particles within the shell. We already showed that in water the titania core particle could move closer to the shell at higher electron dose rates. Interestingly, when we increase the electron dose rate for titania core rattles in glycerol carbonate, the titania core became more confined to the middle part of the shell geometry (Supporting Movie 2). Therefore the mobility of the titania core particle in glycerol carbonate seemed to decrease as the electron dose rate increased (Figure 3.7a). Due to our relatively long frame time, we were unable to record a reliable diffusion step of the particle between two frames, thus the scanning speed was insufficient when the particle became more confined. Using a direct electron camera might help to understand this odd behavior of titania core in glycerol carbonate better. But it might be caused by an increase in surface charge (as compared to the silica particles), but for now, this is mostly speculation. Figure 3.7b shows the relationship between the electron dose rate and the mobility for silica core particles within the shell with sizes similar to those for titania core/silica shell particles. The mobility of silica core particles seemed less affected by the electron dose rate. A slight increase in the diffusion coefficient of the silica core might occur (Figure 3.7b), although this cannot be said conclusively due to

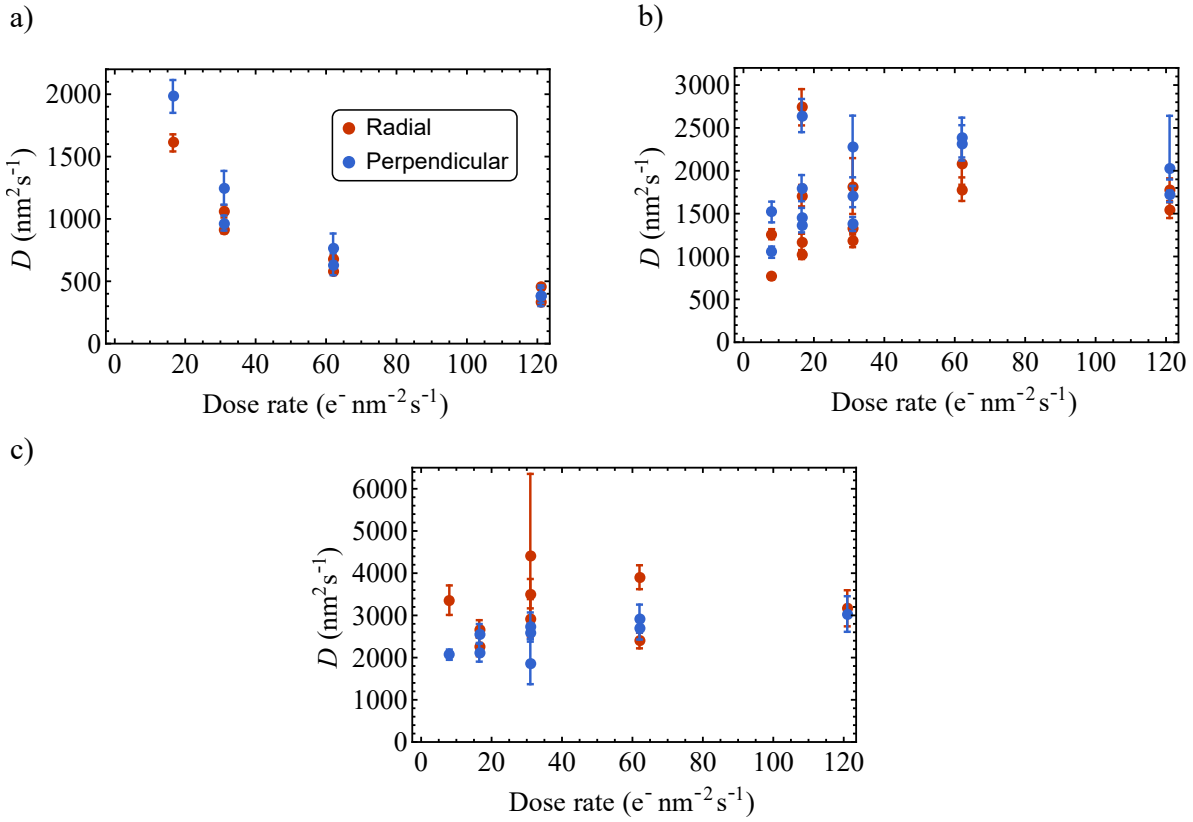


FIGURE 3.7. The mobility of the core particle at different electron dose rates. (a) The influence of the electron dose rate on the mobility of a titania core inside a silica shell. The void diameter is 690 nm. (b) The influence of the electron dose rate on the mobility of a silica core entrapped in a silica shell. The void diameter is 740 nm. c) The influence of the electron dose rate on the mobility of a silica core entrapped in a silica shell. The void diameter is 990 nm.

the errors in the measurement. The diffusion coefficient could increase slightly due to the electron beam altering the solvent's viscosity slightly. It is noteworthy that this was not due to electron beam heating. A detailed study on the heat generation and conduction caused by electron beam found minimal heating (10^{-2} - 10^{-3} K) even at a higher electron dose rate compared to this work (1.1×10^3 e⁻ nm⁻²s⁻¹) [128]. As the electron dose rate had a large effect on the confinement of the titania core particle to the middle of the shell, we cannot give a diffusion coefficient for the titania core, as it may already be affected at the lowest electron dose rate. However, since the silica core seemed to be largely unaffected by the electron dose rate we discuss the diffusion of the silica core particle in the small and large shells in the next section.

Influence of the shell size on mobility of the core particle

Second, we studied the mobility of the core within the middle of the spherical geometry as a function of shell size. Here particles with an identical silica core, but smaller or larger silica shells were used. The mobility of the core particle did not change significantly when increasing the electron dose rate for both shell sizes (Figure 3.7b and c). We used a weighted average of the radial and perpendicular diffusion coefficients, which are similar in the middle of the shell (Figure 3.7b and c), to give a diffusion coefficient for the particle in the center of the spherical geometry. For the small shell we found a diffusion coefficient of $D_{\text{small}} = (1.5 \pm 0.5) \cdot 10^3 \text{ nm}^2\text{s}^{-1}$, while we found $D_{\text{large}} = (2.7 \pm 0.6) \cdot 10^3 \text{ nm}^2\text{s}^{-1}$ for the large shell. When we compare this to the diffusion coefficients we expected to find from our finite element calculations, namely $D_{\text{small,calc}} = 1.4 \cdot 10^3 \text{ nm}^2\text{s}^{-1}$ and $D_{\text{large,calc}} = 2.6 \cdot 10^3 \text{ nm}^2\text{s}^{-1}$, we find excellent agreement. We attributed the difference in mobility of the core particle in the two shell sizes to hydrodynamic slowing down due to the spherical confinement of the core where the hydrodynamic coupling between the core particle and the shell wall in larger shells is lower than in smaller shells. Roughly speaking, the stick boundary condition of the fluid motion at the shell surface is causing the slowing down of the diffusion as compared to free diffusion. The closer one is on average to this shell the stronger the slowing down, while the motion in the direction towards the shell because of this boundary condition completely stops almost at the shell surface while the motion parallel to the shell is also strongly affected but does not go to zero. We will investigate the hydrodynamic interactions between the core and the shell further in the next section.

3.3.3. Hydrodynamic interactions between a core particle within a rigid spherical shell

The hydrodynamic coupling between a diffusing object and a boundary depends on the inter-separation distance as well as the confining geometry [146, 152]. Moreover, in spherical confinement the particle-wall separation and the particle-cavity size ratio influence the diffusivity [158]. Here we study the position-dependent displacement of the core particle. The diffusion of the particle in different parts of the shell is not the same. It can be seen for instance from Figure 3.8 that the mobility of the particle slows down as it approaches the shell. We analyzed the motion of the core particle in various parts of the shell for multiple particles and all of them showed the same decreasing trend as the core approached the shell wall more closely. As the particle approaches the shell, as mentioned, the hydrodynamic interactions become stronger and the radial and perpendicular core diffusion coefficients decrease, but in different ways. We analyzed the 2D projection of the motion of the core particle. By binning the displacements by radial distance from the center in a way that each bin contains the same amount of data points, we can find the influence of the proximity of the shell on the mobility of

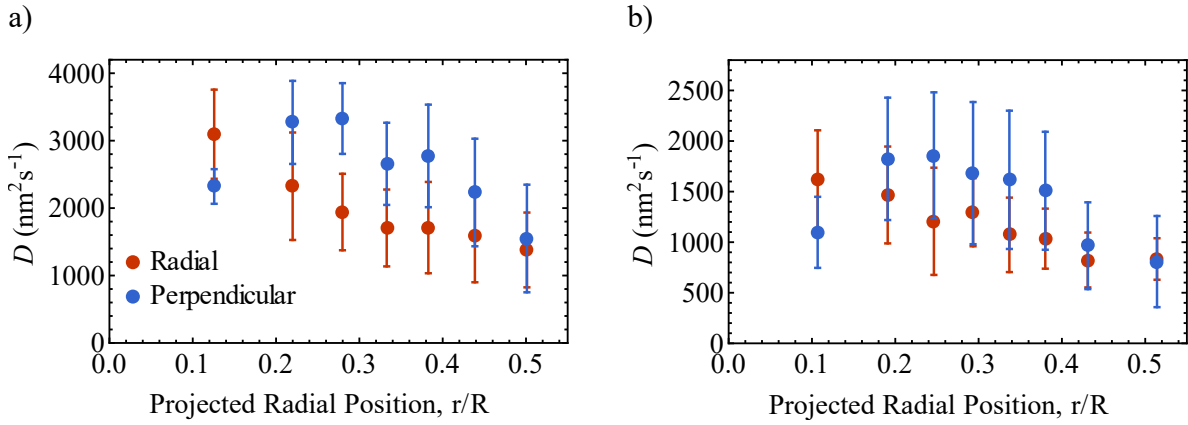


FIGURE 3.8. Experimental diffusion data for the mobility of a core particle within a shell as a function of the projected radial position of the core within the shell for (a) R_{shell}/R_{core} ratio of 3 and (b) R_{shell}/R_{core} ratio of 2.2. Both radial and perpendicular components of the diffusion coefficient are shown. The time step used to obtain the diffusion coefficients was 0.2 s. The radial binning of the displacements was done in such a way that each projected radial area had the same amount of data points. The diffusion coefficients in the graphs are a weighted average over the diffusion coefficients of several data-sets of particles (13 for the small shell and 8 for the large shell).

the particle, as the core will be relatively more often close to the shell even in 3D when it is far from the middle in the 2D projection. As described in the introduction section of this chapter, the shell wall breaks the symmetry around the core particle resulting in an anisotropic diffusion represented by two diffusion constants depended on two orthogonal directionalities with respect to the shell. One for the local motion along the radial direction $D_r(r)$ (towards or away from the center) and another component for the motion perpendicular to the radial direction $D_p(r)$ (parallel to the curved surface). Both components depend differently on the particle wall separation distance [157, 158]. Hence, we decoupled the radial and perpendicular mobility of the core in order to study the dynamics in the 2D projections. Figure 3.8a shows the experimental data for the silica core diffusion inside big shells and Figure 3.8b shows the experimental data for the silica core diffusion inside small shells.

We start the analysis by first looking at the projected radial mobility. The results for both the small and large shells show that the radial diffusion coefficient dropped off when the particle got further from the middle of the shell geometry. While this is in qualitative agreement with the reduction of the radial diffusion coefficient predicted by the theoretical work on the hydrodynamic coupling of a particle in spherical confinement [158], we are likely also observing influence of the time resolution being insufficient to analyze the data close to the shell. For a freely diffusing particle the average step size within our frame time of 0.2 s would be approximately 60 nm. As the particle got further

from the center of the geometry the time resolution was therefore no longer sufficient, especially in the radial direction towards the shell. The particle could go towards the shell and return within 0.2 s, which makes drawing conclusions about the radial diffusion coefficient close to the shell unfeasible. A more viscous medium, such as glycerol mixed with approximately 5 v% of water, as well as a faster camera would improve this result. However, we found that working with glycerol in the electron microscope is even more tricky than working with glycerol carbonate due to bubble formation.

For the direction perpendicular to the radial direction, the problem of the time resolution is still present when the particle is close to the shell wall. However, our data show that the perpendicular diffusion coefficient remained fairly constant for most projected radial positions until $r/R > 0.4$, where the perpendicular diffusion coefficient drops off rapidly. This is likely due to the insufficient temporal resolution of our measurement. The fairly constant perpendicular diffusion coefficient up until $r/R = 0.4$, where the time resolution problem occurs, is in agreement with theoretical work of Aponte-Rivera *et al.* which predicted that the perpendicular diffusion coefficient remains above 90% of its value in the middle until the core particle is really close ($r/R = 0.85$) to the shell. However, our data again shows the influence of the time resolution being insufficient as we observed that the perpendicular diffusion coefficient started to decrease much further away from the shell than predicted.

The error bars in Figure 3.8 show a large spread in the data for individual particles. This may be due to the polydispersity of both the core and the shell sizes which arose from the synthesis procedure, leading to the widespread data points for individual particles, translating to large error bars. This, next to the poor time resolution, hinders us from drawing accurate conclusions. However, our data does hint that the radial and perpendicular components of the diffusion coefficient change differently depending on the radial position of the core particle. With a more viscous medium and a better time resolution, the decoupling of these two components could lead to accurate comparison to theory, and/or comparing these measurements with full 3D measurements that are possible with light 3D nanoscopy as is planned in future work.

The core feels the hydrodynamic interactions even in the middle of the shell due to the long-range character of hydrodynamic interactions. The detailed analysis of the hydrodynamic interactions at the proximity of the shell ($r/R > 0.5$) is not feasible as the electrostatic repulsion between the core and the shell prohibits the core to become close to the shell. Increasing the ionic strength by flowing salt solutions inside the LC increases the repulsion-free region inside the shell and provides the opportunity to study the hydrodynamic interactions when the core is close to the shell.

As mentioned above, our experimental data are a 2D projection of a 3D motion. We used finite element calculations to compare them with experimental results by averaging for the unknown z coordinate in the experiments. This was done by calculating the

hydrodynamic slowing down in many z planes and averaging those calculations in a geometrically meaningful way. For the calculation, the core particle is placed on various z planes, as shown in Figure 3.9a. It is then moved closer to the shell while staying on the same z plane, in order to calculate the effect of the distance between the core and the shell on the diffusion. This results in curves relating the diffusion of the core particle to its position in the shell for a certain z coordinate, as shown in Figure 3.9b and 3.9c. To get a prediction for the trend we would expect to see in the experimental 2D projections, we need to average the curves of all z coordinates. This was done by seeing each z coordinate as a volumetric part of the total object. We calculated an average which was weighted by the likelihood of the core particle, being in the volume of that particular z coordinate region. In the form of an equation, this would look like

$$D(r) = \sum_{z=0}^{z=1} \frac{D(r, z)}{V_{slice}(z) \times V_{total}} \quad (3.11)$$

where

$$V_{slice}(z) = 2\pi(1 - z)^2 dz \quad (3.12)$$

and the different z planes are between 0 and 1. This way we made sure that the sum of all the volume slices is the same as V_{total} :

$$\sum_{z=0}^{z=1} V_{slice}(z) \times V_{total} = 1 \quad (3.13)$$

It is important to notice that, for the calculation of the volumes, an exclusion zone of 30 nm from the shell was assumed to predict the volumes in which the core particle could move. The average of the diffusion curves of all the z slices resulted in an expected diffusion curve for the experimental 2D projection data. The expected diffusion curves for the radial and perpendicular components of the diffusion are plotted in Figure 3.9d and 3.9e, respectively. The 2D projection curves are compared to the 3D curves. It can be seen that the curves for 2D projection are slightly altered from their 3D counterparts. Most notably, the 2D projection curve for both the radial and the perpendicular component predicts that a 2D projection of a 3D object gives a slower apparent diffusion than if the measurement would be done “correctly” in 3D. We are therefore planning to perform such full 3D diffusion data using light nanoscopy on fluorescent rattle particles, before doing the same measurements by TEM. Figure 3.9f shows the final radial and perpendicular diffusion curves we expect for the experimental data, where a 2D projection of a 3D object is measured. Comparing the calculations with experimental results shows that there is a qualitative agreement between the theoretical predictions and the experimental results for the radial diffusion coefficient. The radial diffusion coefficient in the experiments dropped more rapidly as it became closer to the shell wall, due to the limitations of the time resolution. On the other

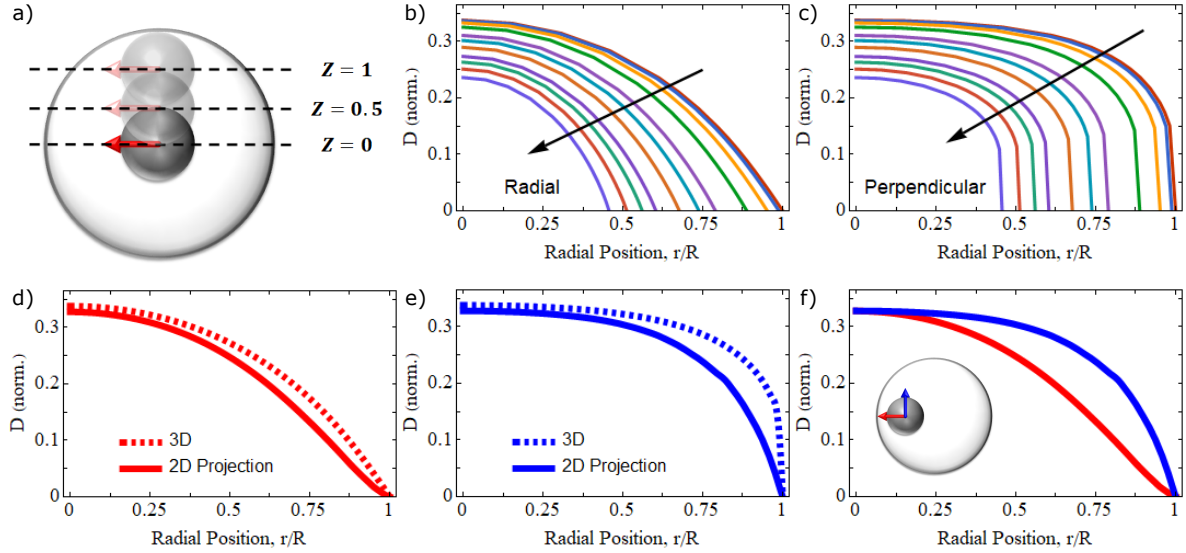


FIGURE 3.9. Finite element calculations for the expected curves for hydrodynamic slowing down in a shell with a R_{shell}/R_{core} the ratio of 3 in experiments, corrected for the 2D projection of a 3D object. a) Schematic showing different particle positions in z , which would be viewed as the same position in an experimental 2D projection image. b,c) Hydrodynamic slowing down of a core particle on different z planes for the radial and perpendicular component of the diffusion, respectively. The arrow indicates the direction of increasing z values. The used z values were 0, 0.15, 0.31, 0.46, 0.61, 0.67, 0.74, 0.80, 0.83, 0.86, 0.89. d,e) The resultant curves after averaging over all z planes, representing a 2D projection, compared to the 3D curves for the radial and perpendicular component of the diffusion, respectively. f) The final radial and perpendicular diffusion curves we expect for the experimental data, where a 2D projection of a 3D object is measured. The red curve is the radial component and the blue curve is the perpendicular component of the diffusion.

hand, the comparison between the experimental results and the calculations reveals that the perpendicular component of the diffusion in the middle of the shell is lower than expected for all types of particles. This is mainly an artifact because any motion from the middle of the core to somewhere else has to be at least partially radially outward. This is seen in experiments, but not in the finite element calculations.

3.4. CONCLUSIONS AND OUTLOOK

We optimized the LC-STEM conditions to study the diffusion of colloidal particles within a spherical shell. A model system of particles where a charged colloidal particle is entrapped in a charged shell, known as a rattle or yolk-shell particles, were utilized to investigate the electrostatic and hydrodynamic interactions between the core and the shell. We found that the diffusivity of the particle in different parts of the shell is different due to the hydrodynamic interactions, which are dependent on the particle wall separation distance as well as on the particle-cavity size ratio. The diffusion coefficient in spherical confinement should be decoupled into two components: one in the radial and the other in a perpendicular direction with respect to the shell. We showed that the radial diffusion decreased as the particle moved closer to the shell, which is partly due to insufficient time resolution, and that the perpendicular diffusion stayed constant for most parts of the shell, in qualitative agreement with hydrodynamic calculations and simulations [158]. We performed finite element calculations to correct the 2D projection experimental data with diffusivities calculated for the full 3D geometry. The results showed that the curves for 2D projection are slightly altered from the correct 3D counterparts. The electrostatic interactions were affected by the presence of the electron beam, and by increasing the electron dose rate the particle was found to be able to diffuse closer to the shell in water. This is the result of multiple effects of the electron beam including pH changes, and direct charging of the particles. The effect of the increase in ionic strength due to a higher electron dose rate was most likely not the main cause of these effects since the change is not significant in our system. Our data provided limits for this system where the effects of the electron beam can be minimized. By using glycerol carbonate and slowing down the movement of the particles, quantitative analysis showed that the diffusion of silica particles is dependent on the shell size and it was found to remain largely unchanged by increasing the electron dose rate. However, the titania core particles were found to be more confined to the center of the shell geometry in glycerol carbonate with increasing the electron dose rate. This effect could be due to the different charging effects of the electron beam on titania in comparison to silica particles. Despite all the limitations of LC-STEM for studying the dynamics of colloidal particles, we expect that using the low dose conditions ($< 100 \text{ e}^- \text{nm}^{-2}\text{s}^{-1}$) with low accumulated electron dose (less number of frames) in combination with a viscous solvent as described in this work, and utilizing advanced microscopy equipment such as direct electron cameras, will make the LC-(S)TEM technique a powerful tool to study the dynamics of colloidal particles in complex geometries. Furthermore, we are close to performing full 3D measurements using nanoscopy and electron microscopy on the same rattle particle to obtain the exact diffusion coefficient of the core particle, which in the future makes it possible to use

rattle particles as a temperature probe and/or a sensor for other sensing capabilities, like the ionic strength inside the liquid cell.

3.5. ACKNOWLEDGEMENTS

This research was done in collaboration with Tom Welling. We thank Kanako Watanabe for synthesizing the rattle particles, and Albert Grau Carbonell for critical reading of the chapter. The authors also acknowledge the EM square center at Utrecht University for access to the microscopes.

APPENDIX 1: SUPPLEMENTARY MOVIES

Supporting Movie 1

LC-STEM movie showing the titania cores became attached to the shell in the water at higher magnifications (electron dose rates higher than $\sim > 300 \text{ e}^- \text{nm}^{-2} \text{s}^{-1}$). The movie is accelerated by a factor of 5 with respect to real-time.

[https://drive.google.com/file/d/13MXBFTvh4JpBMkstqw73hA31dE5jV7UQ/view?
usp=sharing](https://drive.google.com/file/d/13MXBFTvh4JpBMkstqw73hA31dE5jV7UQ/view?usp=sharing)



FIGURE S3.1. Corresponding QR code for supporting movie 1

Supporting Movie 2

LC-STEM movie showing the titania core became more confined to the middle part of the shell geometry in glycerol carbonate by increasing the electron dose rate. The movie is accelerated by a factor of 5 with respect to real-time.

[https://drive.google.com/file/d/1HKfwB2zsXeH80jGjPCgN-36GxLy1cZbN/view?
usp=sharing](https://drive.google.com/file/d/1HKfwB2zsXeH80jGjPCgN-36GxLy1cZbN/view?usp=sharing)



FIGURE S3.2. Corresponding QR code for supporting movie 2

4

In-situ study of the wet chemical etching of SiO₂ and Metal(oxide)@SiO₂ core-shell nanospheres

ABSTRACT

The recent development of Liquid Cell (Scanning) Transmission Electron Microscopy (LC-(S)TEM) has opened up the possibility of studying the behavior of nanomaterials down to the nanoscale in a liquid environment. In this study, we show that the chemically induced etching of different silica nanoparticles can be reliably studied at the single-particle level using LC-(S)TEM with a negligible effect of the electron beam. Here we scrutinize the influence of electron beam irradiation on the etching process for multiple silica-based model systems, and we show that the cumulative electron dose on the imaging area plays a crucial role in the observed damage, and needs to be considered during the experimental design. Monte-Carlo simulations of the electron trajectories during LC-(S)TEM experiments allowed us to relate the cumulative electron dose with the deposited energy on the particles, which was found to significantly alter the silica network under imaging conditions of nanoparticles. Finally, we used optimal LC-(S)TEM imaging conditions to systematically characterize the wet etching of silica and metal(oxide)-silica core-shell nanoparticles with cores of gold and iron oxide, which stand for many other core-silica-shell systems. The LC-(S)TEM method reliably reproduced the different etching patterns of Stöber, water-in-oil reverse microemulsion (WORM), and amino acid-catalyzed (AAC) silica particles that were reported before in literature. Furthermore, we directly visualized the formation of yolk-shell structures from the wet etching

of Au@Stöber silica and Fe₃O₄@WORM silica core-shell nanospheres, without the strong deforming drying forces present in previous studies on dry materials.

4.1. INTRODUCTION

Silica nanoparticles or core-shell silica-shell nanoparticles are of general interest, as they are biocompatible and stable in a large number of solvents [191], in which they also form stable dispersed colloidal systems with interactions tunable over a large range of distances [122, 192–194]. Three widely used strategies to synthesize spherical colloidal silica systems are the Stöber [24, 25, 29, 38, 195], water-in-oil reverse microemulsion (WORM) [30, 44, 46, 196] and amino acid-catalyzed AAC methods [31, 32, 34, 51, 52, 197–201]. These approaches all have in common that a basic environment is created in which both the hydrolysis and condensation of tetra- and/or tri-alkoxysilanes are catalyzed by OH⁻ ions which also impart the growing particles with a negative surface charge and colloidal stability. The Stöber method relies on the hydrolysis and condensation of the precursor tetraethyl orthosilicate (TEOS) which is homogeneously dissolved by the addition of an alcohol to the water phase while basic ammonia catalyzes the hydrolysis and condensation reactions, additionally, protocols for successful seeded growth processes have been developed as well [24, 25, 29, 38, 195]. The WORM method also exploits ammonia as the catalyzing agent, but the condensation reactions take place in the aqueous phase of a water-in-oil microemulsion, while the TEOS is initially dispersed inside the oil phase and hydrolysis at the oil-water interface and then gets dissolved within the water droplets; also for this methodology seeded growth has been achieved [30, 44, 46, 47, 196]. In the AAC method, TEOS condensation is catalyzed by a basic amino acid (L-lysine, L-arginine) in an aqueous solution while unhydrolyzed TEOS is not dissolved until after the first hydrolysis of an ethoxy group; again seeded growth conditions have been established for this method as well [32, 33]. All three synthesis approaches result in spherical, relative monodisperse particles, but potentially different internal silica structures which have shown to be in all cases not to be homogeneous [31, 39, 198].

So far the best-studied silica nanoparticles are Stöber based particles. Their growth mechanism consists of an initial aggregation process of several nm-sized siloxane moieties, followed by their continuous growth by monomer addition into smoother, spherical particles [24, 25, 29, 38, 195]. The overall growth rate is limited by the speed of the hydrolysis of TEOS, which is a first order reaction. Towards the end of the reaction the concentration of hydrolyzed silanol groups goes down, giving more time for the formation of siloxane bonds and the amount of Q⁴ silica goes up [45, 202]. This growth mechanism results in an inhomogeneous internal distribution of silica condensation levels [31, 198, 202]. Silica condensation is typically described using the NMR terminology for the relative amounts of silicon atoms with one (Q¹), two (Q²), three (Q³) and four (Q⁴) siloxane bonds [39]. Particles synthesized with the WORM method are believed to also have an internal structure even less condensed to those of Stöber spheres [39], as the

growth conditions are similar and it has been shown that the cores of the particles are more easily dissolved than the outer parts [203] similarly as for Stöber silica particles. In the AAC method particles form in an aqueous environment, and although it has been shown that the amino acids become incorporated inside the silica particles by adsorbing to the nuclei [31] the total silica particles have similar Q^4/Q^3 ratios indicating that these aggregating smaller silica units from which the particles are build up from [201] are more highly condensed. Furthermore, AAC reactions are performed at relatively elevated temperatures. Silica is known to further condense when the temperature is increased [198] which could explain while the AAC based synthesis overall Q^4/Q^3 ratio is the same as that of Stöber silica, but within the clusters not having AAC attached it has to be higher [197].

Understanding the internal distribution of condensation levels in silica particles can help to explain the reported differences in properties and behavior w.r.t. dissolution between the different silica nano-spheres [197]. The characterization of the internal structure of silica nanoparticles can be investigated with invasive techniques, such as inducing the chemical etching of the particles and monitoring its effects. Silica is slightly soluble in room temperature neutral pH water, as siloxane bonds break, and silicic acid and silicates are released into the aqueous phase [161]. Silica solubility is strongly dependent on the pH, and increased pH values lead to increased solubility [204]. Therefore, the internal organization of the condensation degrees of the silica network can be revealed by exposing the nanoparticles to a basic aqueous solution. Loosely condensed parts (low $Q^4:Q^3:Q^2:Q^1$ ratios) will dissolve more easily, as fewer siloxane bonds need to be broken [45]. Highly condensed parts (high $Q^4:Q^3:Q^2:Q^1$ ratios) will dissolve slower, as the density of siloxane bonds is higher. Gas physisorption can also be used to characterize the size of the pores of nanoparticles and has been used to characterize silica colloids [205], but of course, only gives an averaged impression of the internal structure. Previously how the morphology of particles changes in etching studies consisted of several time-consuming cleaning steps in which the etching needs to be quenched and the particles need to be dried for regular (S)TEM analysis as a function of time. It should be remarked that if drying is not done by e.g. critical drying the drying forces can significantly alter the structures under observation as surface tension forces can be quite strong as compared to kT when the radius of curvature of liquids become in the nm size range.

LC-(S)TEM allows in-situ monitoring of the morphology evolution of nanostructures in chemically active, wet environments [112, 113, 206–209], and thus could possibly be used to characterize the evolution of silica-based nanoparticles in liquid solutions in which the particles can be etched. LC-(S)TEM studies rely upon the illumination of a sample in a liquid environment by a highly energetic electron beam. However, beyond particular thresholds of intensity, electron beam irradiation is known to directly generate

conditions for which particles are affected by radiolysis of the liquid [125, 210]. Up to now, the role of electron irradiation on chemical reactions has been studied extensively for the stability of precursors in solution [111, 211–217] but its effects on other chemical processes (e.g. wet etching of nanostructures) remain not that well investigated. Wet etching (or dissolution) of nanostructures in LC-(S)TEM has been reported in previous studies, but the effects of electron dosage were only partially evaluated or only evaluated after the sample was exposed to the electron beam irradiation in time [206, 208]. The total dose experienced by a sample is also known to play an important role in the behavior of systems in a liquid cell and the interpretation of its results, as the effects of the electron beam accumulate the damage done [212, 218]. Therefore, describing and understanding the impact of the electron beam exposure onto nanoparticles dispersed in chemically reacting solvents is important for the future development of in-situ LC-(S)TEM methodology with a particular aim on finding the conditions where these effects can be neglected.

In this study, we first describe the etching of AAC silica particles dispersed in basic aqueous solutions contrary to Stöber and WORM type silica nanoparticle were found to not etch from the interior through an outside shell, but reduced in size continuously from the outside inwards. Next, we made use of this better defined and different etching of AAC silica nanoparticles to characterize the effects of the electron beam irradiation on this type of silica particles immersed in water and in basic aqueous solutions. The cumulative electron dose during the LC-(S)TEM imaging of the wet etching of silica nanoparticles is the main parameter regarding electron beam effects. Our findings revealed that the effects of the electron beam on the etching and stability of silica nanoparticles can be reduced and even made negligible by minimizing the cumulative electron dose on the particles, independent of the electron dose rate. Furthermore, we found that the electron irradiation directly affected the wet chemical etching of silica by depositing enough energy in the silica to severely alter the siloxane network. This knowledge was used to characterize the wet etching of Stöber and WORM silica nanoparticles, and Fe₃O₄@WORM silica and Au@AAC silica core-shell nanoparticles. The inhomogeneous etching patterns of silica-based nanospheres synthesized via different methods were characterized. We report the direct imaging of the void formation step of yolk-shell nanoparticles from metal@silica core-shell nanospheres via the inhomogeneous etching of the silica shell. LC-(S)TEM shows that the metal core became mobile during this void formation. Describing the behavior of the gold and iron oxide core-shell silica particles, which stand for many more of such core-shell systems, during the yolk-shell formation can lead to a better understanding of the final product, as well as potentially opening the door to new synthesis procedures.

4.2. EXPERIMENTAL

4.2.1. Materials

Tetraethyl Orthosilicate (TEOS, 99%, Sigma-Aldrich), L-arginine (98%, Sigma-Aldrich), Absolute ethanol (Merk), MilliQ water (Millipore system), Sodium hydroxide (reagent grade, ≥98%, pellets, Sigma-Aldrich), Hydrogen tetrachloroaurate trihydrate ($\text{HAuCl}_4 \cdot 3\text{H}_2\text{O}$, ≥99.9%), Sodium citrate tribasic dihydrate (≥99.0%), polyvinylpyrrolidone (PVP, Mw = 10000 g/mol), Polyoxyethylene (5) Nonylphenyl Ether (IGPAL CO-520, Sigma-Aldrich), Ammonia (NH_3 , 30w%, Sigma-Aldrich), Iron chloride ($\text{FeCl}_3 \cdot 6\text{H}_2\text{O}$, 98%, Sigma-Aldrich), Sodium Oleate (95%, TCL), Hexane (98%, Sigma-Aldrich), Oleic acid (90%, Sigma-Aldrich), 1-Octadecene (90%, Sigma-Aldrich).

4.2.2. Synthesis protocols

Stöber Silica Spheres. Stöber Silica particles (120 nm) were synthesized with a simple one-pot synthesis. A 1000 ml round bottom flask was cleaned thoroughly with ethanol and Milli-Q water. Then 500 mL of absolute ethanol was added. 33.3 mL of ammonia was added and the flask was stirred at 600 rpm. Then 20 mL (0.2 M) of TEOS were injected on the top of the stirring cone. The flask was sealed and stirred overnight. The particles were cleaned by centrifugation steps with ethanol and Milli-Q water.

Amino Acid-Catalyzed (AAC) Silica Spheres. AAC Silica particles (113 nm diameter) were synthesized with a three-step synthesis based on previous literature [53]. First, 28 nm cores were synthesized as follows: in a 500 mL 1-neck flask (cleaned with the base) 182.5 mg (0.006 M) L-arginine was dissolved in 169 mL Milli-Q water. The mixture was heated to 70 °C and stirred slowly (200 rpm). After 1 hour, 11.2 mL (0.34 M) of TEOS was added slowly via the wall. The reaction mixture was stirred for 1 day to complete the synthesis. These cores were overgrown up to a diameter of 55 nm as follows: in a 500 mL 1-neck flask (cleaned with the base) 183.5 mg (0.006 M) L-arginine was dissolved in 169 mL Milli-Q water. 19.3 mL of the dispersion of 28 nm silica particles was added. The mixture was heated to 70 °C and stirred slowly (200 rpm). After 1 hour, 11.2 mL (0.34 M) of TEOS was added slowly via the wall. The reaction mixture was stirred for 1 day to complete the synthesis. These nanoparticles were overgrown up to the final 113 nm diameter as follows: in a 500 mL 1-neck flask (cleaned with the base) 182 mg (0.006 M) L-arginine was dissolved in 169 mL Milli-Q water. 19.3 mL of the dispersion of 55 nm silica particles was added. The mixture was heated to 70 °C and stirred slowly (200 rpm). After 1 hour, 11.2 mL (0.34 M) of TEOS was added slowly via the wall. The reaction mixture was stirred for 1 day to complete the synthesis.

Water-in-Oil Reverse Microemulsion (WORM) Silica Spheres. WORM Silica spheres (30 nm diameter) were synthesized following the water-in-oil reverse microemulsion

method [219, 220]. 20 mL of cyclohexane and 1.6 mL of IGPAL CO-520 were mixed and stirred for 15 minutes. To this solution, 120 μ L of NH₄OH solution and 30 μ L of Milli-Q water was added. After 15 minutes, 360 μ L (92 mM) of TEOS was added and the reaction mixture was left under stirring for 12 hours at room temperature. The resultant colloids were centrifuged (7500 *g*, 15 min) and washed with absolute ethanol. The solid product was then redispersed in ethanol.

Au@Stöber Silica Core-Shell Spheres. Citrate stabilized spherical AuNPs (15.5 nm diameter) were synthesized using the sodium citrate reduction method [191, 193]: 200 mL H₂O and 2.0 mL of an aqueous solution containing 10 g/L HAuCl₄·3H₂O were added to a 500 mL two-neck flask with stirring bar and reflux condenser. The flask was placed in an oil bath and heated until boiling. Then, 6.0 mL of an aqueous solution containing 10 g/L sodium citrate tribasic dihydrate was rapidly added under vigorous stirring (1200 rpm) and the mixture was left refluxing and stirring for 15 min. during which a color change from yellow to dark blue to pink and finally deep red was observed. The stirring was slowed down to 400 rpm and the mixture was allowed to cool down to room temperature. Au@Stöber NPs were synthesized as follows: 2.4 mL 10 wt.% PVP [122] in water was added to 100 mL of the as-synthesized AuNPs and stirred (300 rpm) for 24 h. The PVP-coated particles were collected by means of centrifugation (15000 *g*, 1 h.), redispersed in 100 mL ethanol and added to a 300 mL Erlenmeyer flask. Then, a 10 mL ammonium hydroxide solution was added, followed by 0.2 mL of a 10% (V:V) TEOS in ethanol solution under vigorous stirring (1200 rpm) and left stirring. After 90 minutes, another 0.4 mL 10% TEOS in ethanol solution was added and left to react for 90 minutes after which the particles were collected using centrifugation (15000 *g*, 1 h.), redispersed in ethanol, centrifuged and finally redispersed in 10 mL ethanol. The ethanolic particle dispersion was stored at room temperature for at least 1 year without loss of colloidal stability.

Magnetite (Fe₃O₄)@WORM Silica Core-Shell Spheres. Mono-dispersed magnetite nanoparticles (9 nm diameter) were prepared from an iron oleate precursor by thermal decomposition as described in literature [221]. The method involves two steps. In the first step, the metal-oleate precursor was synthesized by reacting iron chloride (FeCl₃.6H₂O) with sodium oleate. In the second step, this metal-oleate precursor was further heated to 320 °C using the high boiling point solvent 1-Octadecene. The solution was kept at this temperature for 30 minutes, which lead to the nucleation and growth of the nanoparticles. The resulting solution was washed with excess acetone and collected by centrifugation and dispersed in hexane or cyclohexane. To synthesize the core-shell magnetite-silica spheres (40 nm diameter) we followed the water-in-oil reverse microemulsion method [196, 219, 220, 222]. In a typical synthesis procedure, 2.5 mg

of Fe_3O_4 nanoparticles stabilized by oleic acid as ligands were dispersed in 20 mL of cyclohexane and 1.6 mL of IGPAL CO-520 were stirred for 15 minutes. To this solution, 120 μL of NH_4OH solution and 30 μL of Milli-Q water was added. After 15 minutes, 360 μL of TEOS was added and the reaction mixture was left under stirring for 12 hours at room temperature. The resultant colloids were centrifuged and washed with absolute ethanol. The solid product was then dispersed in ethanol.

4.2.3. Ex-situ etching experiments

Nanoparticles were dispersed in plastic vials with final concentrations of 0.6 mg.mL^{-1} (10 mM) in NaOH aqueous solutions with the desired base concentrations and were left to react for the desired amount of time. Samples were collected by drop-casting on Formvar/Carbon Film 200 Mesh Copper TEM grids after 1 cleaning step consisting of 10 minutes of centrifugation at 20000 g and redispersion in Milli-Q water.

4.2.4. In-Situ liquid cell experiments

Experiments were performed using a liquid cell dedicated holder from Hummingbird Scientific, (USA). Silicon chips with silicon nitride (SiN) windows ($50 \times 200 \mu\text{m}$, 50 nm thickness) were used to encapsulate the liquid volume. In all experiments, spacers of 100 nm or 250 nm were used. The side of the chips which were in contact with liquid was glow discharged for 90 seconds prior to use. Around 2 μL of a diluted suspension (0.06 mg.mL^{-1}) of the desired nanoparticles were drop-casted on the top chip and let to dry, this way a number of particles were found to be attached to the top window during the experiments. Then the bottom chip was placed in a dedicated holder, 2 μL of Milli-Q water was drop-casted on it and then the top chip was placed into position aligned over the bottom window. Excess water was removed with filter paper and the cell was sealed. To flow solutions into the set-up, a Hamilton syringe pump was utilized with a 1 mL glass syringe. If needed, the chip was carefully opened, left to dry, and placed on a regular TEM holder for dry imaging of the resulting particles after the experiments.

4.2.5. Sample characterization and Imaging

Dynamic light scattering (DLS). The ex-situ etching of AAC silica spheres was followed via DLS with a Zetasizer Nano ZS. A dispersion of AAC silica spheres with a final particle concentration of 0.6 mg.mL^{-1} was prepared in an aqueous solution with the desired NaOH concentration. The particle size was measured continuously every 10 seconds and averaged per minute.

(S)TEM. Imaging was carried out with a Tecnai-F20 transmission electron microscope (TEM, Thermo Fisher Scientific) equipped with a field emission gun and operated at 200 keV. Scanning TEM ((S)TEM) imaging was performed with an annular dark-field

detector (ADF, E.A. Fischione Instruments Inc., Model 3000, USA) with a camera length of 120 mm. The dose rate was calculated from the beam current of the empty column (no holder) and the frame size as described in Chapter 2.

4.3. RESULTS AND DISCUSSION

4.3.1. AAC silica spheres as model system to study the beam effects on wet silica etching

To study the effects of the electron beam irradiation on the wet etching of silica nanospheres, a system of nanoparticles with a quantifiable etching pattern was required. Comparing the LC-(S)TEM observations of such processes with their known ex-situ counterparts would expose the effects of the electron beam irradiation. We characterized the ex-situ etching of AAC silica nanoparticles ($d = 113$ nm, PD: 3%, concentration: 10 mM) dispersed in NaOH aqueous solutions. We monitored the etching process by taking samples in time to compare the bulk etching with the in-situ etching inside the liquid cell (Figure 4.1). AAC silica spheres showed a homogeneous decrease in diameter when exposed to the basic media (Figure 4.1a). The etching process lasted up to weeks if enough NaOH was present in the system (Figure 4.1b), and could be used to easily tune the size of a batch of AAC silica spheres to any desired size. The polydispersity of the AAC silica nanoparticles increased as the particle size reduced during etching while the width of the size distribution remained roughly the same (Figure S4.4). These observations indicate that AAC silica was not found to etch through a more condensed outer shell as Stöber and WORM based silica was found to do [197, 200, 201]. A similar etching behavior was observed when AAC silica nanoparticles were etched in HF aqueous solutions (Figure S4.3).

The homogeneous internal structure of AAC silica spheres was further studied by closely following their etching in time. As the diameter of the particles changes gradually, dynamic light scattering (DLS) is a suitable technique to follow their etching in the presence of different NaOH concentrations (Figure 4.1c). The etching process happens in two different phases. For the first ~ 300 minutes, the particle size decreased slowly (less than 5 nm in a 100 mM NaOH solution). After this initial regime, the etching rate increased and the particle size showed a more pronounced decrease. This second phase has been studied as a linear process to compare the etching rates between various base concentrations. It can be readily observed that as the base concentration increased, the etching rate did increase as well (Figure 4.1d). However, the positive trend of the etching rate slowed down at higher pH.

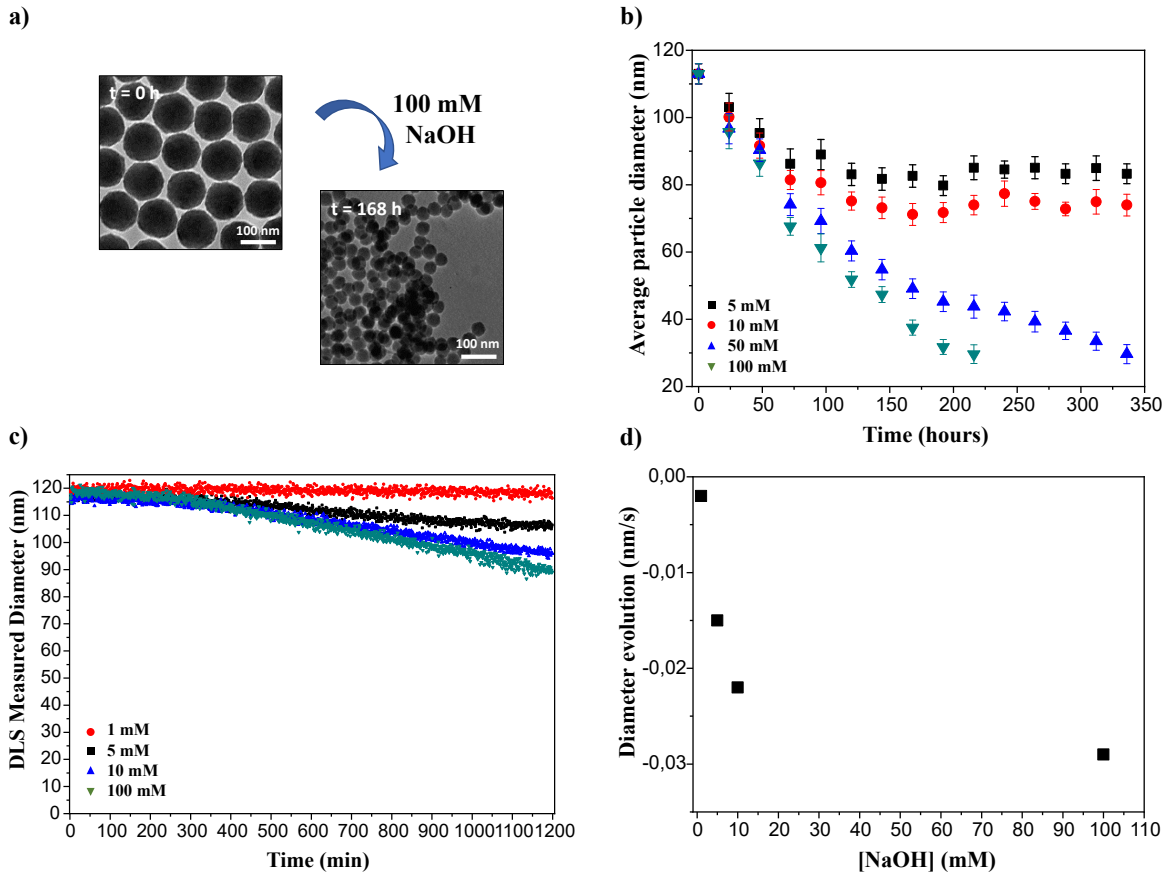


FIGURE 4.1. Ex-situ, bulk etching of AAC silica nanoparticles. a) TEM imaging of AAC Silica particles dispersed in a NaOH aqueous solution. AAC silica particles etch homogeneously, decreasing in size over time. b) Time evolution of the etching process of AAC silica spheres in aqueous NaOH solutions. The data were obtained from TEM imaging of dried samples taken at different time points. c) Time evolution of the etching process of AAC silica spheres in aqueous NaOH solutions followed by DLS during the first 20 hours of the process. The etching process shows two parts. For the first hours (up to around 300 min), the decrease in diameter is slow. The second part (from 300 min to 1200 min) of the etching process shows a faster decrease in diameter. d) The slope of the second part of the etching fitted by linear regression. The speed of the etching increased with the base concentration, but the change in rate was smaller for higher base concentrations.

4.3.2. Characterization of the electron beam irradiation effects on the stability and the wet etching of silica particles

LC-(S)TEM allowed us to study the wet etching of silica nanoparticles at the single-particle level by exposing them to an aqueous NaOH solution during (S)TEM imaging. We showed that AAC silica nanoparticles exhibit two different regimes of etching during the first hours of etching. Here we exploited the mode of etching of the AAC silica

colloids during the first hours in a 100 mM NaOH aqueous solution to determine the conditions under which the silica wet etching process became not altered by the electron beam. The expected behavior was a slow etching of the spheres, and any change in such behavior to be ascribed to electron beam effects. The low degree of polydispersity of the initial AAC silica particles (3%) allowed for the precise analysis of the morphological evolution of the particles. The size evolution of the particles was followed by digital analysis via ellipsoid fitting to binarized data sets as it was done before in the literature [209]. We prepared the liquid cell set-up as described in the methods; the top window of the chip was covered by the nanoparticles. A region of particles was used to focus on the window, the imaging area was shifted with the beam blanked to avoid unnecessary irradiation of any area of interest, after which imaging was performed. If the experiment happened under the NaOH aqueous solution flow, the imaging was started when the liquid leaving the holder outlet was found to be at the desired pH by probing it with pH paper, which happened one or two minutes after the flow started.

Continuous imaging was performed with 1024×1024 pixels, $16 \mu\text{s}$ dwell time, and 1.58 nm or 0.78 nm pixel sizes. The nanoparticles were imaged while pure water was flowing into the cell (Milli-Q grade, $5 \mu\text{L} \cdot \text{min}^{-1}$). Our LC-(S)TEM observations show that the particles expanded gradually up to $\sim 10\%$ of their starting size (Figure 4.2a), and subsequently dissolved, in agreement with the results in Chapter 2 and previous LC-(S)TEM studies of silica particles in water at high electron dose rates [209]. The initial expansion under a flow of pure water happened at a similar rate for all electron dose rates ranging from $570 \text{ e}^- \text{nm}^{-2} \text{s}^{-1}$ to $2.3 \times 10^3 \text{ e}^- \text{nm}^{-2} \text{s}^{-1}$, but the dissolution was faster for higher electron dose rates. When the behaviors were compared for similar accumulated doses they became almost the same (Figure 4.2b). The electron beam irradiation in pure water is known to change the pH of the solution to more acidic values and to produce a number of reducing and oxidizing agents [125]. Scavenging some of these radicals ($\text{e}^- (\text{aq})$, H^\bullet) was shown to increase silica stability in water during LC-(S)TEM experiments [209].

AAC silica spheres were remarkably more affected by the electron beam if the particles were imaged under a flow of a basic aqueous solution (100mM NaOH (aq), $5 \mu\text{L} \cdot \text{min}^{-1}$). The pronounced expansion was consistently observed if the system was imaged for all of the used electron dose rates (Figure 4.2c). This expansion was found to amount to up to $\sim 30\%$ of the initial size of the nanoparticles. This process was faster for higher electron dose rates, ranging from a few minutes for dose rates of $2.3 \times 10^3 \text{ e}^- \text{nm}^{-2} \text{s}^{-1}$ and $3.4 \times 10^3 \text{ e}^- \text{nm}^{-2} \text{s}^{-1}$, to around 20 minutes for a dose rate of $520 \text{ e}^- \text{nm}^{-2} \text{s}^{-1}$ to a number of hours for a dose rate of $31 \text{ e}^- \text{nm}^{-2} \text{s}^{-1}$. The disparity was completely lost when the expansion is considered as a function of the cumulative dose on the frame (Figure 4.2d). The onset and initial evolution of all the expansions happened at similar cumulative electron doses, regardless of the electron dose rate. On the other hand, the dissolution

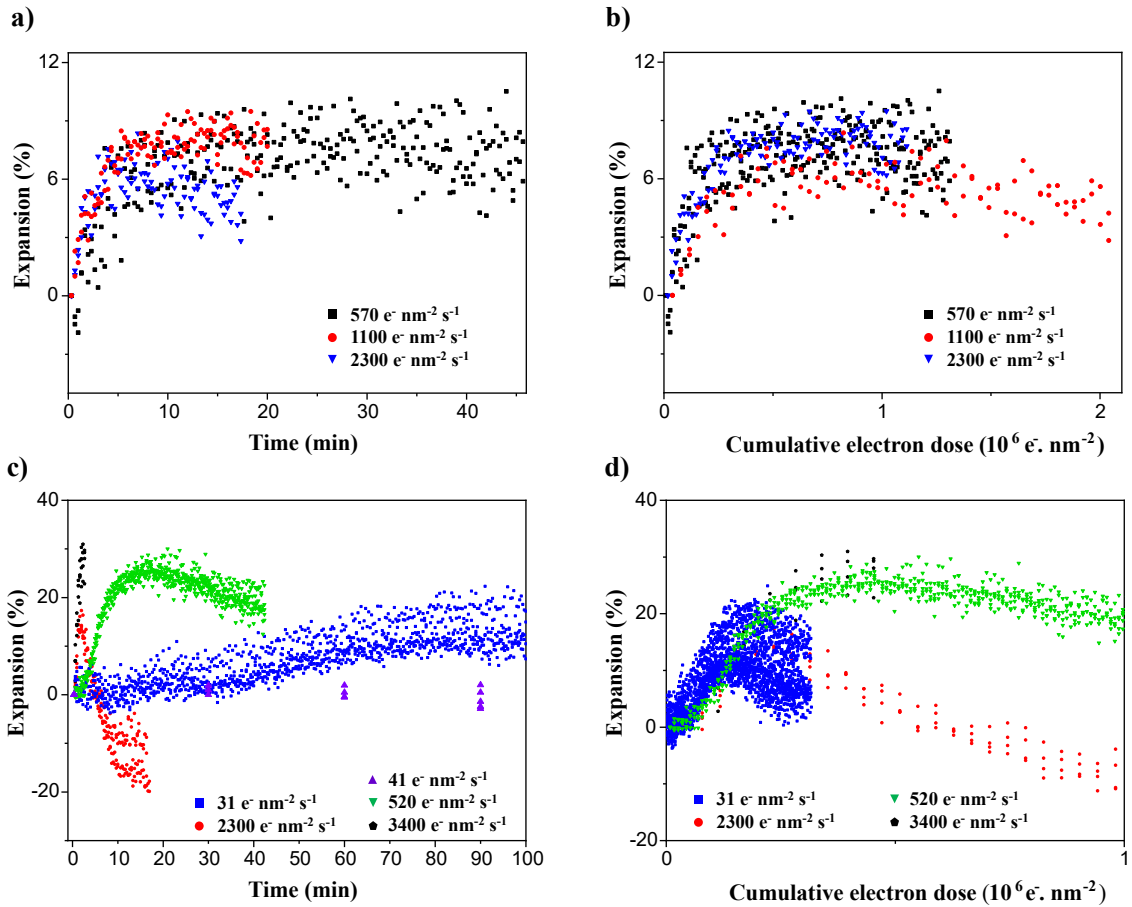


FIGURE 4.2. In-situ etching of AAC silica monitored by Liquid Cell (S)TEM. a) Time evolution of the size of AAC spheres in pure water under different electron dose rates. The size evolution of the same experiments as a function of the cumulative dose is shown in b). c) Time evolution of the size of AAC spheres in a 100 mM NaOH aqueous solution under different electron dose rates. The size evolution of the same experiments as a function of the cumulative dose is shown in d). Each panel contains data of 4 to 5 different nanoparticles. The flow rate was 5 $\mu\text{L} \cdot \text{min}^{-1}$ in all experiments.

process remained different for different dose rates even if these were corrected for the total accumulated doses. At low dose rates ($31 \text{ e}^- \text{nm}^{-2}\text{s}^{-1}$), expansion was slow as few electrons were deposited per frame. This allowed the concurrent dissolution process to take place extensively during the expansion period, and therefore the overall expansion was not as high as in other cases. At a moderate electron dose rate ($520 \text{ e}^- \text{nm}^{-2}\text{s}^{-1}$), the expansion happened faster, and therefore the dissolution could not play a large role during the expansion phase. The dissolution of the particles happened faster for higher dose rates than for lower dose rates as the network is continuously affected by the electron beam irradiation. At a high electron dose rate ($2.3 \times 10^3 \text{ e}^- \text{nm}^{-2}\text{s}^{-1}$), the network was so strongly affected by the imaging that the dissolution was faster also

during particle expansion. This resulted in a slightly reduced expansion, but also in much accelerated dissolution. Finally, at a high electron dose rate ($3.4 \times 10^3 \text{ e}^- \text{nm}^{-2} \text{s}^{-1}$), expansion happened so fast that the dissolution process could not affect the expansion period. At such high electron dose rates, the scanning induced the deformation of silica particles, as was previously reported [129, 209]. Therefore, our results indicate that the expansion process of silica particles upon electron beam irradiation in presence of water appears to be completely driven by the cumulative electron dose rate on the particle and that the extent of such expansion depends on the media in which the particles are immersed in. On the other hand, the dissolution process was not directly related to the cumulative electron dose. The different dissolution rates are better understood when considering the direct interaction of the electron beam with the silica network, together with the passive dissolution process taking place between the nanoparticle and the surrounding liquid phase. In conclusion, the etching of AAC silica nanoparticles was best imaged by minimizing the cumulative electron dose. Considering this, the relative stability of AAC silica particles during the first hours exposed to an aqueous solution of NaOH was successfully characterized by using a low electron dose rate ($41 \text{ e}^- \text{nm}^{-2} \text{s}^{-1}$) and discontinuous imaging (30 minutes blanks) to reduce the number of electrons accumulated on the imaging area to approximately $2751 \text{ e}^- \text{nm}^{-2}$ (1024×1024 pixels, $16 \mu\text{s}$ dwell time, 1.58 nm pixel size) (Figure 4.2c, dark purple triangle data).

4.3.3. Monte-Carlo simulations of the electron trajectories during LC-(S)TEM imaging of silica particles in water

So far, the effects of electron beam irradiation on silica particles in LC-(S)TEM experiments discussed in literature were in terms of the radiolysis of the solvent. However, this interpretation does not fully explain the expansion/dissolution behavior. Our DLS results show that although a higher pH resulted in increased etching rates, this resulted in a small increase in the etching rate above 100 mM NaOH. Lower values of the pH resulted in slower etching. Therefore, changes in the concentration of OH^- ions cannot fully explain our observations. Additionally, the formation of reducing radicals is also supposed to be lower if the pH of the irradiated solution is high [125]. It is quite clear that chemical modifications of the siloxane structure as caused by the energy deposited by the electron beam also have to play an important role. If the expansion was mediated by such species, it would depend on the electron dose rate and it would be reduced at higher starting pH. Here we propose that the direct interaction between the electron beam and the silica network drives the expansion/dissolution behavior for an important part as well. The deposited energy in the particles during our LC-(S)TEM experiments was assessed. If the electron beam directly affects the structure of the silica network, silica solubility may increase and etching may be favored. The loss of condensation

all over the particles due to the beam-induced excitation of siloxane bonds could then explain their expansion.

The energy that was deposited per cubic nanometer (nm^3) of silica during a LC-(S)TEM experiment was modeled by means of Monte-Carlo simulations with the software CASINO 3.3 [223]. This software simulates the electron paths during (S)TEM imaging through a given sample. The elastic scattering interactions are treated as discrete events, and the inelastic interactions are treated with an energy loss model. Secondary electron generation is also considered. A 3D model of a simplified liquid cell environment was defined to model our experiments. The simulated geometry consisted of two silicon nitride windows of 50 nm thickness that enclosed a volume of 1 μm thick layer of water. In this water volume, we positioned a silica sphere with a 113 nm diameter to emulate our AAC silica particles. The position of the center of the particle was chosen such that the particle was attached to the top window (Figure 4.3a). From the pathways of all the simulated electrons, CASINO calculates the total energy absorbed by every component of the simulated volume. The beam parameters were matched with our experimental conditions: The distance between irradiated points was set to be the experimental pixel size, the number of electrons per scanned point was determined as previously done in literature from the beam current and the dwell time [110,224], the beam was focused on the particle and a beam convergence semi-angle of 20 mrad was used.

The energy absorbed per frame by the silica particle for the electrons used to generate a given pixel (1.58 nm pixel size, 1024×1024 pixels, 10 pA beam current, and 16 μs dwell time) (Figure 4.3b). The binding energy of the Si—O bond is 4.60 eV [225] and there are approximately 216 Si—O bonds in 1 nm^3 (if we assume the maximum density structure for silica which is not the case for all kind of silica nanoparticles). The following rule of thumb can be derived from CASINO simulations for small silica particles located on the top window of a liquid cell: around 12 eV of energy is deposited per nm^3 of silica, per pA of beam current for a frame acquired with 1 μs dwell time and with 1 nm^2 pixel size. However, for our experimental conditions mentioned in section 4.2.2, the total absorbed energy per frame per nm^3 could be ranged from several keV to several MeV (Figure 4.3c). Furthermore, we see that the deposited energy on the particle barely depended on the depth of the particles in the liquid cell and on whether the beam was focused on the particles or not (Figure 4.3d). Beam current, dwell time, and pixel size are therefore the main parameters that need to be optimized to reduce the cumulative dose per frame. This highlights the potential of direct electron detectors, which are nowadays routinely used in cryo-EM experiments because of their ability to gather information from a sample at much lower irradiation levels ($\sim 1 \text{ e}^- \cdot \text{A}^{-2}$) [226,227].

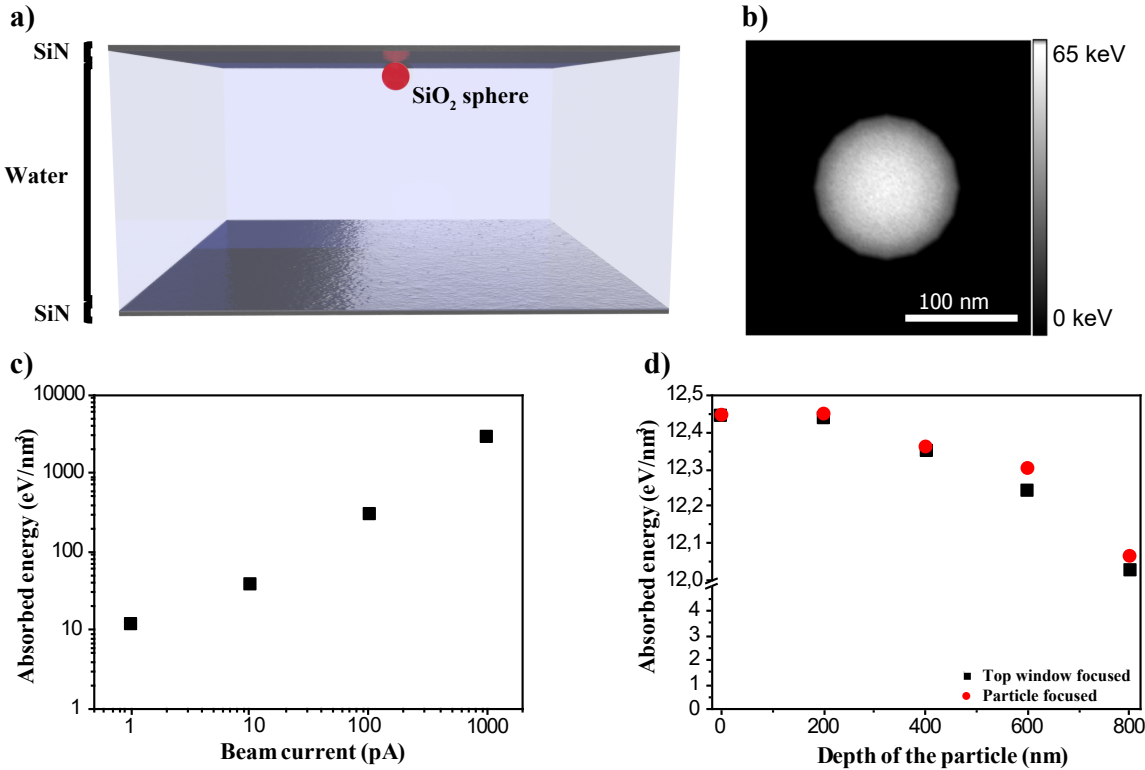


FIGURE 4.3. Simulation of pathways of electrons during (S)TEM imaging simulated with the CASINO software package. a) Schematic of the simulated geometry. A 1 μm water layer was placed between 50 nm silicon nitride spacers. A silica sphere of 113 nm of diameter was placed on the top window. b) Calculation of the energy deposited to the silica particle via elastic and inelastic interactions of the incident electrons (in keV) for a frame acquired with a (S)TEM operated at 200 keV with 1.58 nm pixel size, 10 pA of beam current and 16 μs dwell time. The pixel size of the energy distribution corresponds to the pixel size used during imaging, and the values indicate the deposited energy on the silica sphere from the electrons initially incident on that pixel. c) Absorbed energy per unit volume of a silica particle located at the top SiN window for a number of electron beam currents with the previous imaging conditions. d) Absorbed energy per unit volume of a silica particle located at different depths from the top SiN window for the case of 1 pA beam current.

The main contributions to the absorbed energy are the inelastic interactions between the electrons of the beam and those of the material, as the inelastic scattering cross-section is larger than the elastic scattering cross-section for Si and especially for O for 200 keV electrons [228]. The inelastic scattering of the electrons can promote radiolytic processes in the irradiated material [229, 230]. The decay of the electronic excitations caused by radiolysis can result in the breaking of chemical bonds and may result in atomic displacements in a network as energy can be transmitted to the atom nuclei

via phonons and excitons. Importantly, not every excitation decay results in atomic displacements, as a broken chemical bond does not directly imply a gain in energy sufficient to displace an atom over the surrounding energy barriers [229]. In silicates, the cross-section for radiolytic atom displacements is 10 times higher than that for direct elastic events [231]. In silica, electron irradiation promotes the excitation of siloxane bonds, which in turn can result in the formation of point defects and the loss of connectivity of the silica network [230, 232].

Radiolysis damage is typically assumed to be proportional to the energy deposited by radiation [233]. Deposited energies on quartz (crystalline silica) of a few hundred eV.nm⁻³ via ion beam bombardment have been shown to cause amorphization [234]. Ion bombardment has also been shown to induce the deformation of spherical particles [235], however, the energies involved are in the MeV range which is quite different from the electron beams used in TEM, and quartz amorphization has been well described for electron irradiation [232]. The energy absorbed by silica can be compared to the landscape of energies that have to be reached to displace an atom in the silica network. The energy needed to displace an O atom or a Si atom in the silica network is of the order of a few eV [236], and electron irradiation of SiO₂ films has been shown to displace O atoms, reducing the SiO₂ film into more pure Si areas through the formation of point defects [230, 237]. Therefore, during liquid cell experiments, the typical amounts of energy deposited into the silica network can be up to orders of magnitude higher than the energy needed to strongly affect the siloxane bonds. Such bond breaking (and atomic displacement) events taking place in a particle dispersed in an aqueous NaOH medium will no doubt lead to the easier dissolution of the silica network. Consequently, our results could be explained by an increase in the susceptibility of the silica network to etching by the aqueous base solution as a result of the direct electron beam effects on the material. Additionally, scavenging some of the reducing radicals that are produced by the electron beam was shown to slightly stabilize silica in liquid cell experiments [209]. However, it is likely that these effects are small compared to the increased solubility by the cleavage of siloxane bonds.

4.3.4. In-situ study of the wet etching of SiO₂ and metal@SiO₂ nanoparticles

We first characterized the etching of Stöber and WORM silica nanospheres (Figure 4.4) by exposing them to a solution of 100 mM NaOH (5 μL.min⁻¹). Stöber silica nanoparticles showed an inhomogeneous etching pattern, in accordance with their internal distribution of silica condensation levels (Figure 4.4a) [198]. This process happened at different time scales for different particles and was in contrast to the etching patterns of Stöber silica during LC-(S)TEM experiments under higher cumulative electron doses [209]. We minimized the cumulative electron dose by imaging with an electron dose rate of 61 e⁻nm⁻²s⁻¹, 1.58 nm pixels, 1024×1024 pixels frames, 24 μs dwell time and 30

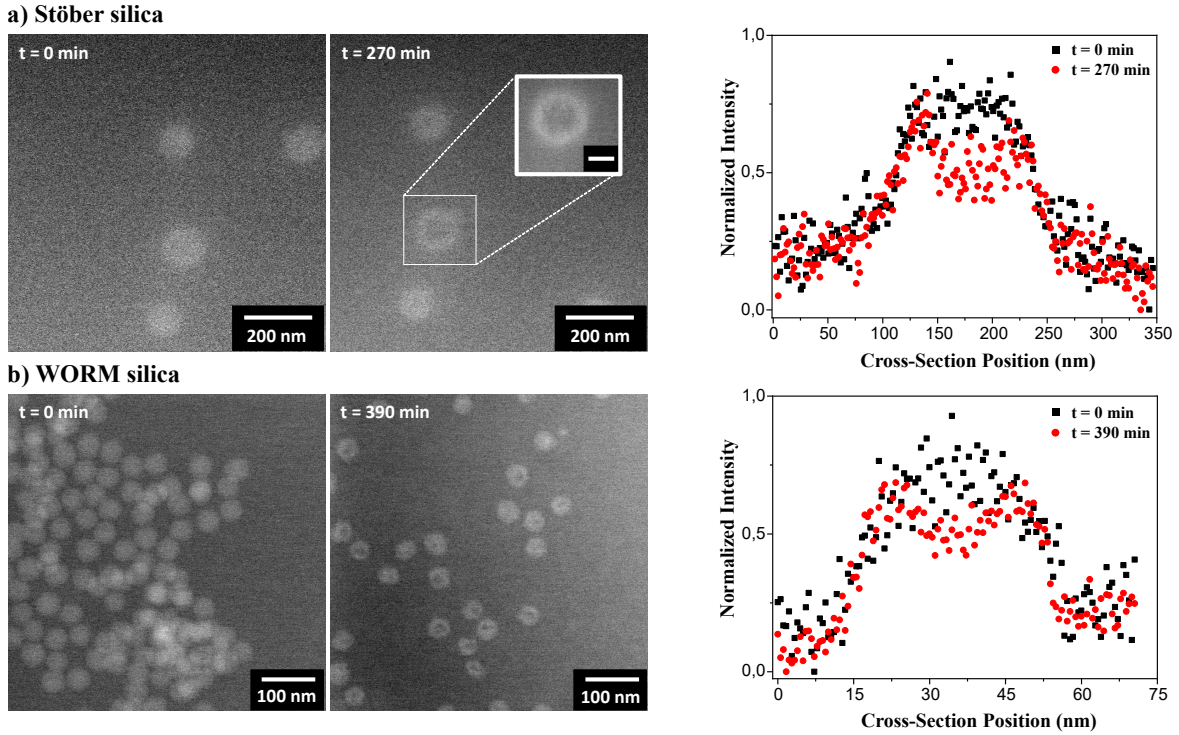


FIGURE 4.4. In-situ etching of silica model nanoparticles by exposure to a 100 mM NaOH aqueous solution with a flow rate of $5 \mu\text{L} \cdot \text{min}^{-1}$. a) Stöber silica. Particles became hollow when exposed to a flow of 100 mM NaOH. Right: The intensity profile along the nanoparticle shown in the inset. No expansion was observed. (total accumulated dose of $1.4 \times 10^4 \text{ e}^- \text{nm}^{-2}$). b) WORM silica nanospheres under a flow of 100 mM NaOH. Due to the small size of the particles (40 nm), our results indicate that the silica network was strongly affected even in a single frame (total accumulated dose of $1.5 \times 10^3 \text{ e}^- \text{nm}^{-2}$). Therefore, different areas needed to be imaged to study how WORM silica nanospheres etched under basic conditions. Particles showed hollowing after 390 minutes of exposure to the basic solution. Right: Intensity profiles of two selected nanoparticles showing the formation of a hollow volume inside the particle, with minimal change in the total size of the nanoparticle. Similarly as was reported before for these particles systems [198]

minutes blanks between frames (total accumulated dose of $1.4 \times 10^4 \text{ e}^- \text{nm}^{-2}$ for Stöber silica nanoparticles and $1.5 \times 10^3 \text{ e}^- \text{nm}^{-2}$ for WORM silica nanospheres). Once the hollow structures became evident, a final frame was taken with $260 \text{ e}^- \text{nm}^{-2} \text{s}^{-1}$ to get better detail (Figure 4.4a, inset). By comparing the intensity profile of a cross-section of a single particle it can be readily seen that these imaging conditions did not induce any expansion during the etching process, correctly characterizing the final product of the wet chemical etching of Stöber silica (Figure 4.4a, right panel).

Studying WORM silica was more difficult than studying AAC and Stöber silica spheres, as the size of the nanoparticles was smaller (40 nm). This made it more challenging to image such nanospheres at low total accumulated electron doses, and required both the dose rate and the magnification to be higher ($1.5 \times 10^3 \text{ e}^- \text{nm}^{-2}$, 0.55 nm pixel size, 24 μs dwell time). Therefore, for silica particles of this size range, it is advisable to image the same area only once. Making use of this knowledge, we followed the evolution of monodispersed WORM silica spheres under a flow of aqueous 100 mM NaOH ($5 \mu\text{L} \cdot \text{min}^{-1}$) by imaging different areas over time (Figure 4.4b). WORM silica spheres became hollow after 390 minutes of exposure to the basic solution, consistent with their behavior under hydrothermal treatments [203].

The formation of yolk-shell structures from metal(oxide)@silica core-shell nanoparticles can also be studied with the methods described previously. Yolk-shell nanoparticles consisting of a catalytically or surface-enhanced Raman scattering active cores surrounded by a void and encapsulated by porous support are known to show superior catalytic and sensing activity in many scenarios [238–241]. This increased efficiency comes from the role of the hollow shell as a micro/nanoreactor, offering several advantages such as prevention of particle sintering, controlled diffusion rates through the shell pores, and homogeneous environments in the void surrounding the catalyst or sensing particle. The synthesis of such particles usually consists of a hard template-based synthesis of core-shell particles and the subsequent removal of material to form a void between the core template and the shell. Here we investigate the void formation step for Au@Stöber silica and Fe₃O₄@WORM silica core-shell particles upon wet etching of the silica shell with a NaOH aqueous solution (Figure 4.5), both these two systems stand as a model for a broad range of nano core-silica-shell particles. We showed that by slightly etching the Stöber (Figure 4.5a) and the WORM (Figure 4.5b) silica shells with a basic solution, well-defined yolk-shell particles are obtained. Furthermore, the Au and Fe₃O₄ cores were found to diffuse in the void once such etching is completed. This opens the door to fully treat the surface of the catalyst once the yolk is formed, and also indicates that the behavior of the catalyst could be manipulated separately from the shell in liquid phase via external fields, as it has been reported for similar structures [120].

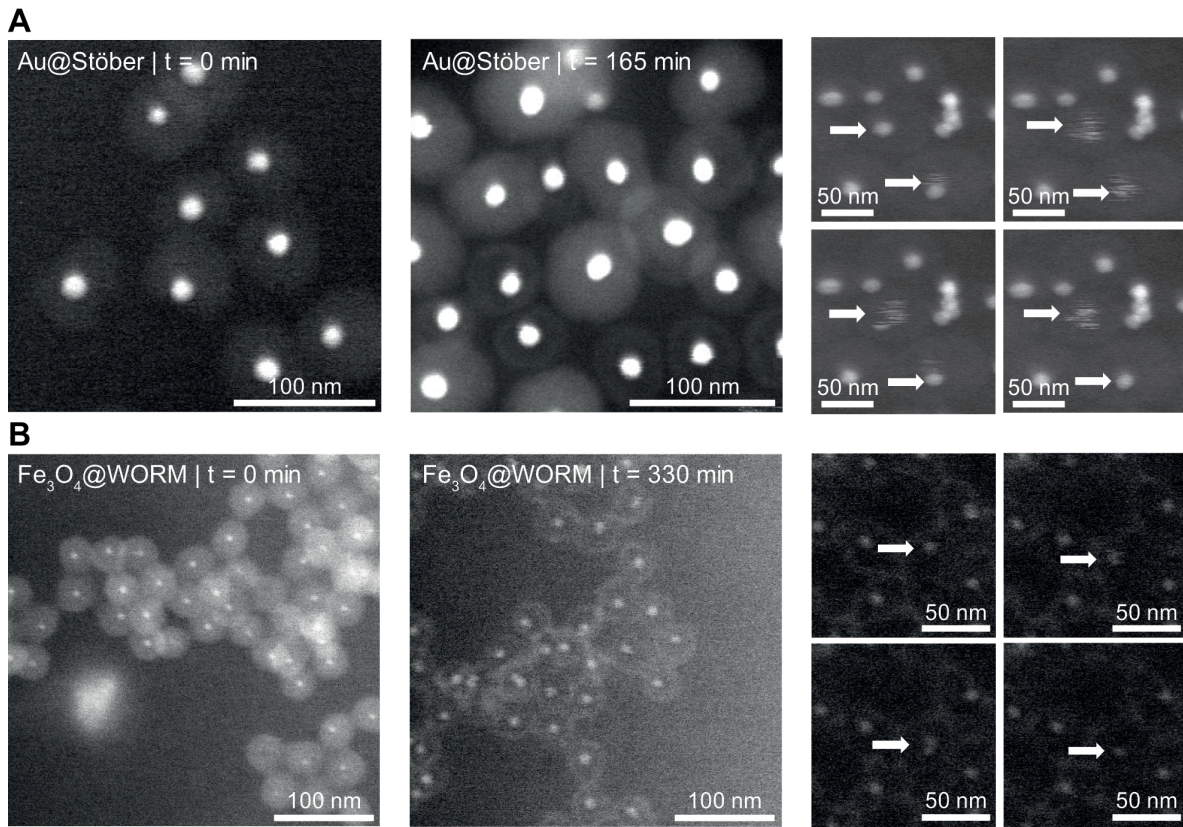


FIGURE 4.5. In-situ etching of core-shell metal(oxide)-silica nanoparticles by exposure to a 100 mM NaOH aqueous solution with a flow rate of 5 $\mu\text{L}\cdot\text{min}^{-1}$. A) Au-Silica. B) Wet etching of Fe_3O_4 core/WORM Silica Core/Shell nanospheres into yolk-shell particles under the flow of a basic aqueous solution. At the left, particles at the start of the experiment. At the center, yolk-shell particles formed after 165 minutes and 330 minutes of exposure to the basic solution by the etching of the silica shell. Different areas were imaged in both a), and b) due to beam sensitivity (total accumulated dose of $1.5 \times 10^3 \text{ e}^-\text{nm}^{-2}$). At the right, experimental observation of the ‘free’ diffusion of the catalytic cores. The white arrows highlight single cores rattling through the void of the yolk-shell particle.

4.4. CONCLUSIONS

The wet etching of silica and metal(oxide)@silica nanoparticles in an aqueous NaOH solution was studied employing in-situ LC-(S)TEM. We exploited the slow and gradual etching of AAC silica spheres in basic solutions to investigate and mitigate the electron beam effects during LC-(S)TEM studies of silica in aqueous and basic aqueous solutions. Our results pinpoint the importance of the cumulative electron dose on silica particles during in-situ LC-(S)TEM experiments as the critical parameter determining whether the observations will diverge from ex-situ etching behavior, but that conditions can be found where the effects can be neglected. Under the conditions where the effects of the electron beam do affect the etching, we report that silica first was found to expand and then dissolved when irradiated in an aqueous environment and that the extent of such expansion was directly correlated to the cumulative electron dose on the imaging area, independent of the used electron dose rate. We showed that this behavior is not the result of changes in the pH of the solution. Furthermore, the expansion and dissolution phenomena were more pronounced under basic conditions. The formation of reducing radicals is assumed to be lower at basic conditions [125], and therefore we conclude that the reported expansion cannot be explained by the presence of water radiolysis products. By performing simulations of the electron beam energy loss we conclude that the energy absorbed per unit volume, per frame by a silica nanoparticle of around a hundred nanometers on the top window of a liquid cell, to be up to orders of magnitude higher than the energy needed to directly break bonds in the silica siloxane network. We propose that the direct effects of the electron beam on the silica network make it more susceptible to etching by the OH⁻ ions in solution and the water radiolysis products. If the energy deposited on the nanoparticles during LC-(S)TEM experiments alters the rate of chemical processes happening between the nanoparticle and the solvent, then the cumulative electron dose (and the electron dose history prior to data acquisition) must be carefully controlled and reported to achieve reliable in-situ studies on chemical reactions in LC-(S)TEM experiments. Using this knowledge, we reliably characterized the wet etching behavior of multiple silica-based model systems: Stöber silica, WORM silica, and Au@Stöber silica and Fe₃O₄@WORM silica core-shell nanoparticles under conditions where the effects of the electron beam can be neglected. We showed that LC-(S)TEM can correctly reproduce the expected etching patterns for Stöber and WORM silica, as well as the formation of yolk-shell structures from Au@Stöber silica and Fe₃O₄@WORM silica core-shell nanoparticles as were reported before in literature [242,243]. Furthermore, we show how the catalyst core became a movable particle inside the shell as the yolk was formed, opening the door to extensive post-treatments of such core-silica-shell systems, as well as to manipulations of the movable core with external fields.

4.5. ACKNOWLEDGEMENTS

This research was done in collaboration with Albert Grau Carbonell. We thank Relinde Moes-van Dijk for the synthesis of AAC silica particles, Rama Kotni for the synthesis of the WORM silica and metal(oxide)@WORM silica particles, and Maarten Bransen for the synthesis of Au@Stöber particles. We also thank Tom Welling for the critical reading of the chapter. The authors also acknowledge the EM square center at Utrecht University for access to the microscopes.

APPENDIX 1: SUPPLEMENTARY FIGURES

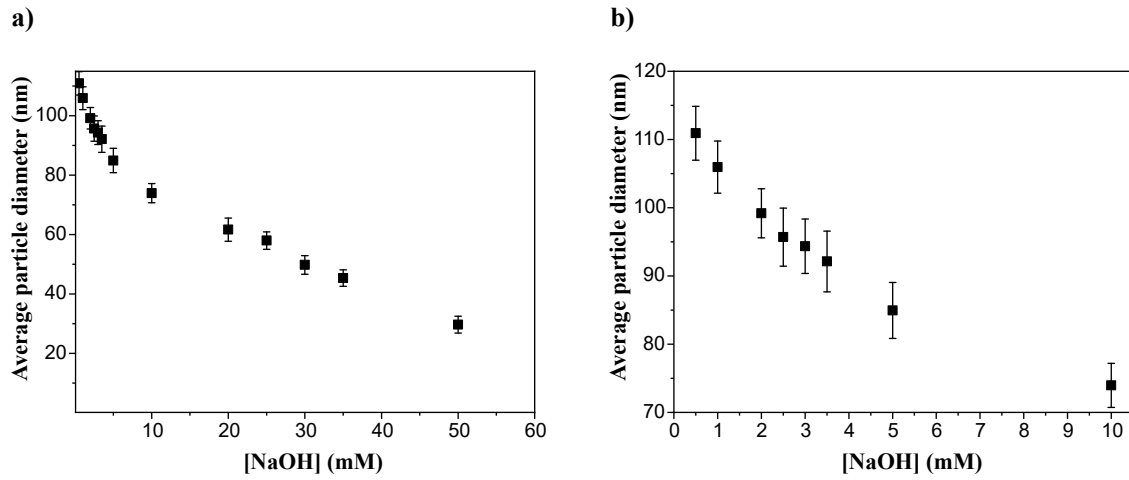


FIGURE S4.1. a) The Ex-situ (bulk) etching of AAC silica spheres spans over a period of days. The initial concentrations of base determine the extent of the etching, and thereby the duration of the process (the initial concentration of silica was 10 mM). The final diameter of the particles shows a strong and clear dependence on the initial NaOH concentration. b) Zoomed in the section up to 10 mM of etchant concentrations.

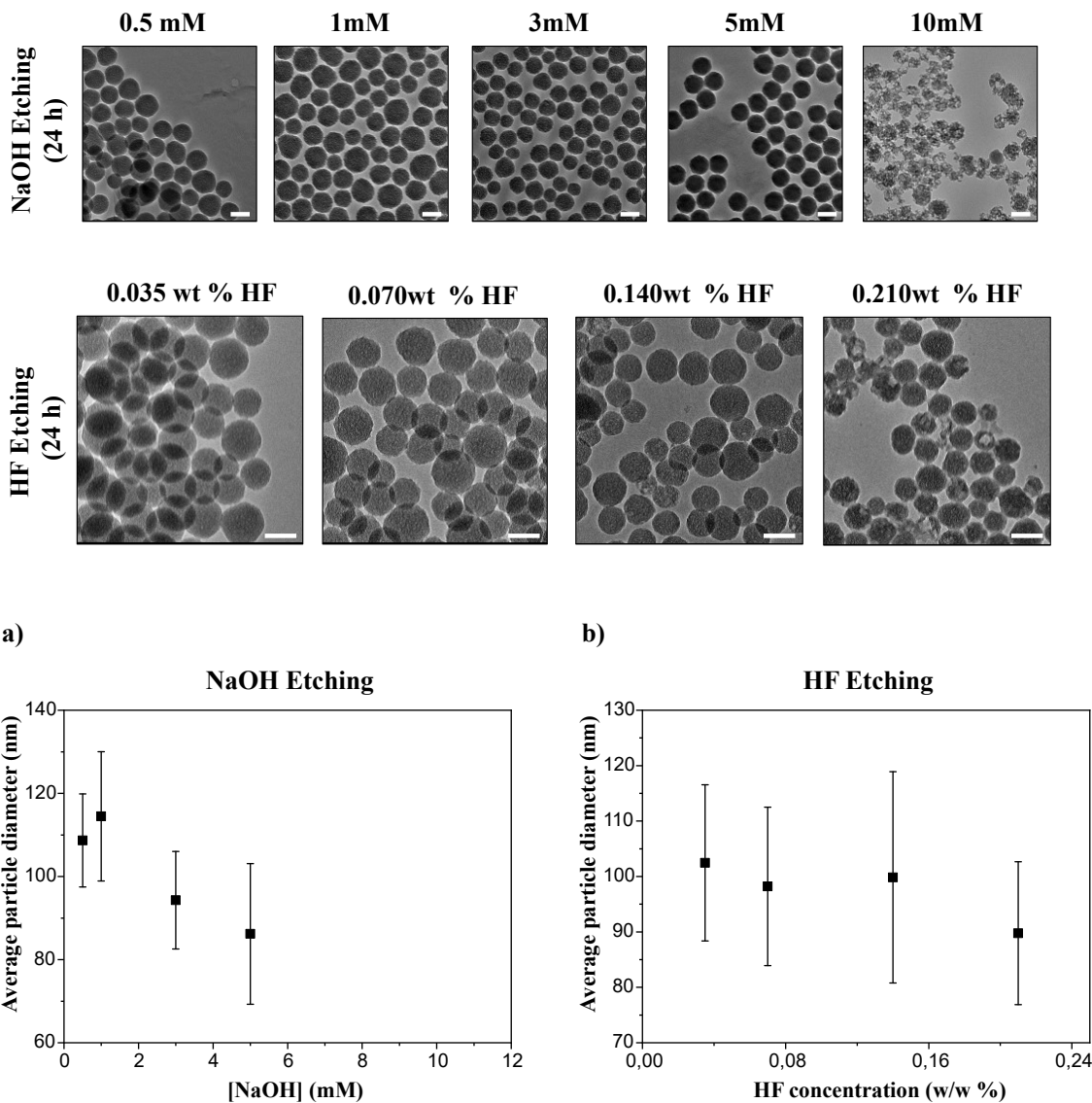


FIGURE S4.2. Etching of Stöber silica (diameter: 102 nm, concentration: 10 mM). Hollowing is observed when Stöber silica spheres are etched both with NaOH or HF aqueous solutions. a) and b) show the diameter of the different batches exposed to different etchant concentrations. The hollowing of Stöber silica was observed above 8 mM NaOH and 0.16 wt % HF. The scale bars indicate 100 nm

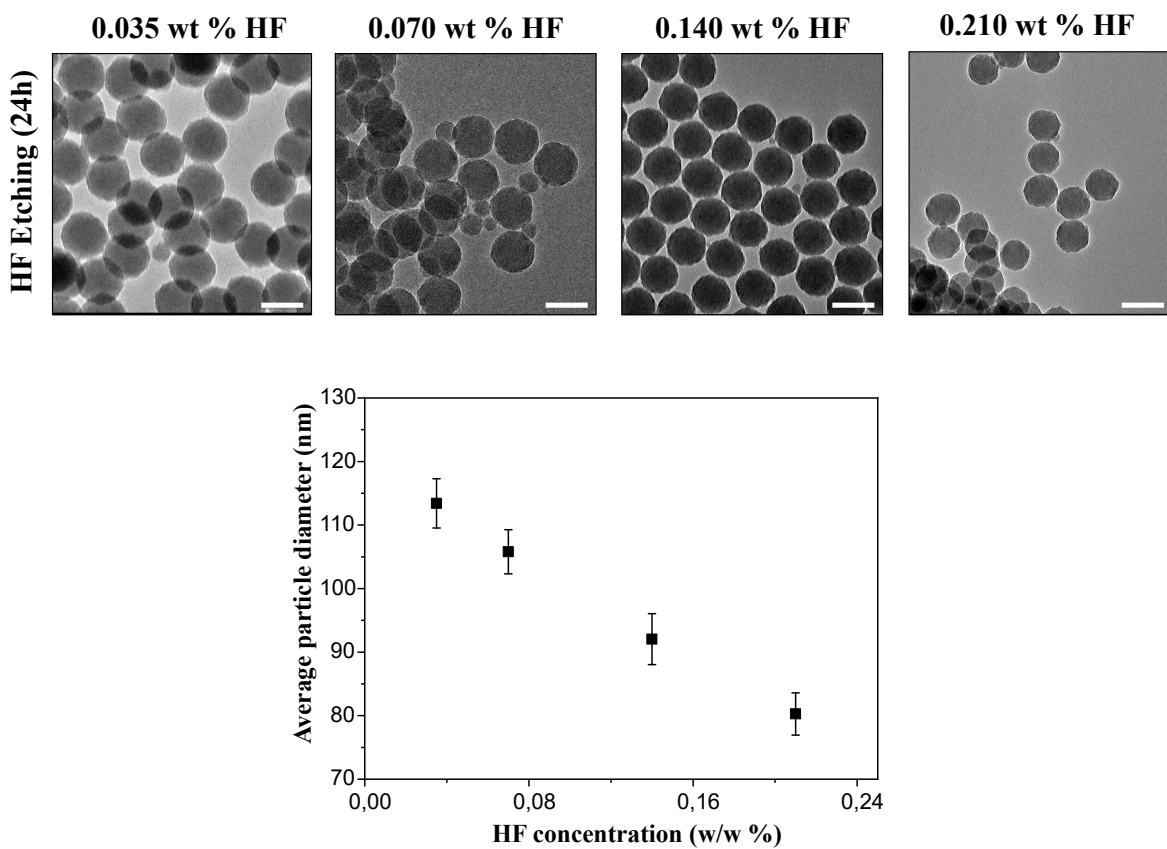


FIGURE S4.3. Etching of AAC silica (diameter: 113 nm, concentration: 10 mM) in HF aqueous solutions. The plot shows the diameter of the different batches exposed to different HF concentrations. The scale bars indicate 100 nm

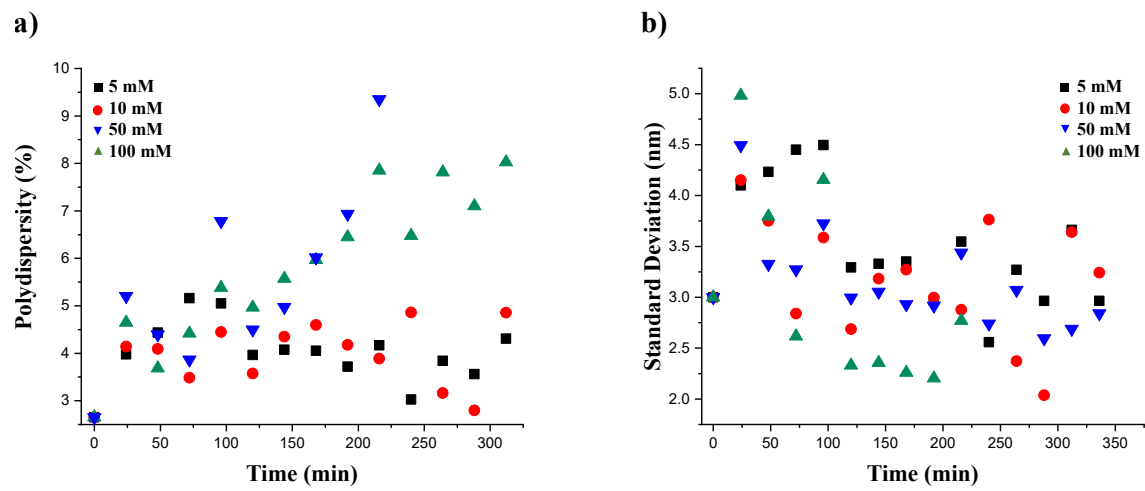


FIGURE S4.4. The progression of the a) polydispersity, and b) standard deviation in time during ex-situ etching of AAC silica particles with an initial diameter of 113 nm and polydispersity of 3%.

5

Complex internal chemical structures of rod-shaped silica colloids investigated by in-situ etching using low-dose liquid cell electron microscopy

ABSTRACT

Understanding the chemical structure of rod-shaped silica colloidal particles is attainable by investigating their etching mechanism in solution. Liquid Cell (Scanning) Transmission Electron Microscopy (LC-(S)TEM) is a promising technique through which the etching of these particles can be observed in real-time, and at the single-particle level without possible deformations induced by the surface tension of dried particles. However, the presence of high energy electrons and the different geometry in liquid cell (LC) experiments may alter the conditions of in-situ experiments compared to their ex-situ counterparts. Here we present a controlled low-dose LC-STEM study of the basic etching process of micron-sized rod-shaped silica particles that are immobilized on the SiN window of a liquid cell. The results show that using low-dose imaging conditions, combined with a low accumulated electron dose, and optimized flow rates of solutions allow for investigation of the chemical etching mechanism of silica colloidal particles using the LC-(S)TEM technique with negligible effects of the electron beam. LC-STEM observations revealed that the rod-shaped silica particles undergo an inhomogeneous etching along their length and finally turn into cone-shaped silica particles via a necking-breaking mechanism. A comparison of ex-situ etching experiments with LC-STEM observations showed

that the LC geometry can play a crucial role in LC-STEM experiments where the diffusion of the etching particles is important, which should be considered during the analysis and interpretations of LC-STEM results.

5.1. INTRODUCTION

The widespread application of anisotropic colloidal particles in the self-assembly of new materials is driven, amongst others, by the ability of such systems to also form colloidal liquid crystal phases. Due to the great potential of anisotropic particles in chemical, electrical, and optical applications, they have attracted much attention [244–252]. New complex functional materials are achievable by self-assembly of these colloidal building blocks [134–136]. Colloidal silica particles are also of interest because of their use in physio-chemical studies of colloidal model systems. The ease of chemical modification of colloidal silica particles’ surfaces by using various types of functional groups, allows for making a vast range of silica particles with different functionalities and interparticle interactions [39, 253, 254]. The recently developed model system of (fluorescent) silica rods by Kuijk *et al.* [83], is a powerful model system to study their self-assembly into various liquid crystalline phases in real space [83, 253, 255, 256]. The synthesis procedure of these rod-shaped silica particles is a simple one-pot synthesis in which ethanol, water, sodium citrate, and ammonia, are mixed with a solution of polyvinylpyrrolidone (PVP) in 1-pentanol to arrive at a dispersion of water with dissolved ammonia, PVP and citrate. Silica rods start to grow upon the addition of the strongly apolar tetraethyl orthosilicate (TEOS) to the pentanol oil phase. The growth of these rods takes place from the water-in-oil emulsion droplet which starts deposition of silica on the oil-water interface after which the rod grows from silica deposited from the watery droplet attached to the growing end of the rods resulting in an anisotropic bullet-shaped particle with a flat end where the watery droplet was attached and a rounded tip due to the anisotropic supply of hydrolyzed TEOS [39, 253]. Although the synthesis of these rod-shaped particles has been studied extensively, there are few studies on their chemical composition. Recently it has been revealed that these rod-shaped silica particles can be transformed into cone-shaped colloidal silica particles upon mild etching by NaOH in water [84]. Understanding the chemical structure of these particles is key to reveal the mechanism of this transformation, which also opens the way to obtain other novel particle shapes.

In order to obtain a fundamental understanding of the in-situ etching process of rod-shaped silica particles at the single-particle level, we have taken a direct approach of imaging this process using Liquid Cell Scanning Transmission Electron Microscopy (LC-STEM) [94, 95]. In this research, we wanted to determine if LC-(S)TEM could be used as a technique to study the chemical composition of these rod-shaped silica particles by monitoring the etching mechanism in a basic environment in real-time without affecting the process by the observation. However, the presence of high energy electrons as well as the confining geometry of the liquid cell (LC), combined with the fact that only particles stuck to the cell window can be continuously observed in time, could all significantly

modify the etching process as compared to etching which takes place while particles are dispersed and undergoing Brownian motion. It is known that the electron beam can affect the imaging area and its surroundings in both direct and indirect ways and chemical reactions could be significantly altered by the electron beam [125]. In order to validate the results in a LC-(S)TEM experiment, we need to control a large number of variables which affect the ongoing chemical and physical processes inside the cell [175, 218]. Therefore, for in-situ monitoring of a chemical process, we need to minimize the influence of the electron beam, optimize the flow rate of solutions, and understand the effect of the liquid cell geometry. A known effect of electron irradiation is the growth or degradation of nanomaterials induced by reducing or oxidizing environments due to the reactive radicals and molecular species formed by electron-solvent interactions [125, 175, 210]. So far, by utilizing different solvents and scavengers, the electron beam induced nucleation, growth and degradation of various types of nanomaterials were studied using the LC-(S)TEM technique [111, 170, 181, 207, 211, 214, 217, 257–265]. However, there are few studies on direct monitoring of a chemical reaction with LC-(S)TEM [266–269]. Etching of rod-shaped silica particles is a nice model system for investigating if the LC-(S)TEM technique can be used for in-situ monitoring of chemical processes. If the effects of the electron beam can be minimized, the etching mechanism and therefore the inhomogeneous chemical composition of these particles can be studied at the single-particle level in real-time at a high spatial resolution without important artifacts that can be induced by strong drying forces that occur if particles are dried on TEM grids without lengthy procedures such as supercritical drying.

Rod-shaped silica colloids prepared by ammonia-catalyzed hydrolysis and condensation of tetraethyl orthosilicate in water droplets, containing polyvinylpyrrolidone cross-linked by citrate ions in pentanol, were found to have an inhomogeneous chemical structure both along the length of the particle as in the perpendicular direction along the diameter of the particle [84]. Here, we show that by tuning the pH of the LC solution while the particles are stuck to a SiN window, while flowing NaOH basic solutions through the cell and optimizing the flow rate, together with using low-dose-rate imaging conditions ($1\text{--}10 \text{ e}^-\text{nm}^{-2}\text{s}^{-1}$), direct observation of the silica rods etching mechanism is achievable. Furthermore, using a discontinuous imaging technique by blanking the beam for a certain amount of time between recording the frames, we minimized the accumulated electron dose (e^-nm^{-2}) on the particle. The accumulated electron dose is also known to have a great impact on LC-(S)TEM results in certain cases (see Chapter 2 and 4) [212]. Comparison with ex-situ etching experiments showed that the low electron dose rate in combination with a low total electron dose, which was at least one order of magnitude lower than previous LC-(S)TEM studies, played a significant role in observing the ‘real’ chemical process with negligible effects of the electron beam. However, the effects of the confining geometry of LC in combination

with the fact that particles immobilized on the window were observed, where the Brownian motion of the particles was completely suppressed, should be taken into account since it can alter the accessibility and diffusion rates resulting in a different etching pathway of the particles in comparison to the conditions where the particles diffuse freely in the solution. The LC-STEM observations revealed how these rod-shaped silica particles undergo inhomogeneous etching along the length of the rod in an aqueous NaOH solution, and how rods with a certain internal morphology for certain NaOH concentrations finally turned into a cone-shaped silica particle. Further validation of the LC-STEM observation for etching of silica rod-shaped particles was carried out using even more complex structured segmented silica rods with known inhomogeneous chemical structure. Here, the degree of condensation along the silica rod was tuned in such a way that a desired part of the rod had a less condensed silica structure so that faster etching in that part was expected simply due to the smaller number of siloxane bonds that needed to be broken in that section as compared to the rest of the silica rods [45, 161]. This inhomogeneous silica structure could be obtained by changing the reaction temperature, precursor concentration, and/or ethanol concentration [86]. Finally, we used the information obtained to explore the chemical composition of newly developed, even more complexly structured silica rod-shaped particles known as crooked silica rods. Such crooked rods have been developed recently in our group [85] and that of others [270] as such particles can form interesting new colloid based liquid crystal phases [271].

5.2. EXPERIMENTAL

5.2.1. Synthesis

Rod-shaped silica particles. Rod-shaped silica particles with a length of $2.6 \pm 0.3 \mu\text{m}$ and a diameter of 300 nm were prepared as described by Kuijk *et al.* [83]. Figure 5.1 shows a typical STEM image of these rods. In a 1 L glass laboratory bottle, 80 g of polyvinylpyrrolidone (PVP, average molecular weight $M_n = 40 \text{ kg/mol}$, Sigma-Aldrich) was dissolved in 800 mL of 1-pentanol ($\geq 99\%$ reagentplus, Sigma-Aldrich) by sonication for 2 hours. After all, PVP had been dissolved in 2 hours, 80 mL of ethanol (100%, Interchema), 22.7 mL of ultrapure water (Millipore system) and 5.3 mL of a 0.18 M sodium citrate dihydrate (99% Sigma-Aldrich) solution in water were added to the mixture of pentanol-PVP. The mixture became turbid upon shaking the flask by hand, indicating that the emulsion was formed. Afterward, 18 mL of ammonia (25% (w/w) in water, Sigma-Aldrich) was added, followed by 6.7 tetraethyl orthosilicate (TEOS, 98%, Sigma-Aldrich). After mixing by shaking, the mixture was left to rest and the reaction was allowed to proceed overnight. Next, to remove the emulsion droplets from the flat end of the particles, the reaction mixture was centrifuged at 1500 g for 1 hour and after removing the supernatant the particles were redispersed in

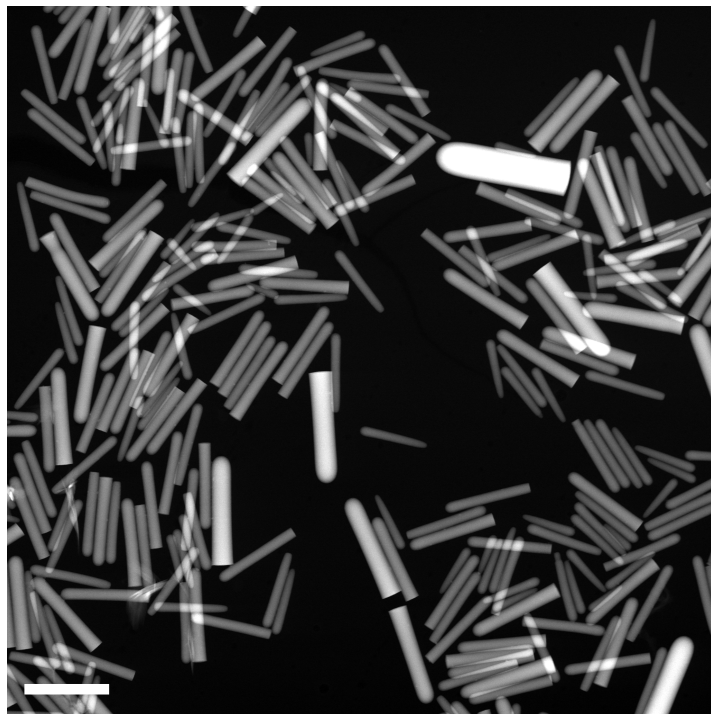


FIGURE 5.1. STEM image of typical, monodisperse, silica rod-shaped particles with a length of $2.6 \pm 0.3 \mu\text{m}$, directly after the synthesis and before the monodispersity was increased by centrifugation to remove the smallest rods recognizable by their lack of a flat end, meaning they lost the droplet early in the synthesis, and large bullet-shaped particles grown from the larger water droplets. The scale bar indicates $2 \mu\text{m}$.

ethanol. The cleaning procedure was repeated twice with water and ethanol where the reaction mixture was centrifuged at 1500 g for 15 minutes and finally, the particles were redispersed in ethanol. To further increase the monodispersity of rods, cleaning steps were carried out. The particles were centrifuged 3 times at 700 g for 15 minutes and the supernatant containing smaller rods was removed. As the last step of the cleaning procedure, the particles were centrifuged at 10 g for 1 hour to remove the larger rods and aggregates, by removing the sedimentation from the sample.

Segmented silica rods. Segmented silica rods were prepared using regulation of the growth temperature, as published in Ref [272], based on the original work of Kuijk *et al.* [83]. In order to vary the chemical composition along the length of the rods, we changed the temperature during the reaction. To this end, we performed the reaction at a scale of 40.0 mL of emulsion in a 40 mL vial. The vial was placed in a preheated hot air oven after the addition of TEOS. The bottles were cooled down at a slow rate to avoid strong convection in the bottle. The temperature was changed during the reaction in the following schemes [86]:

1. 50 °C (2 h), 5 °C (22 h) (nail-shaped)
2. 5 °C (2 h), 25 °C (22 h) (less-condensed tip)
3. 50 °C (1 h), 5 °C (4 h), 25 °C (22 h) (less-condensed middle part)

Specifically, for nail-shaped particles, 1 g of PVP (40000 g/mol) was dissolved in 10 mL of pentanol by sonication in a 20 mL glass vial (Wheaton). To this solution, 1 mL of ethanol, 0.28 mL of water, and 67 μ L of sodium citrate solution (0.18 M in water) were added. After shaking the vial by hand, 0.225 mL of ammonia was added and the vial was shaken again. Finally, 100 μ L of TEOS was added and the vial was shaken once more. The reaction mixture was immediately placed in an oven thermostated at 50 °C. Performing the reaction at elevated temperature reduces the rod diameter, as described in Ref [272]. After 2 h in the oven, the bottle was placed in a fridge at 4 °C to grow the nails' wider "head" After 6-18 h, ethanol was added to quench the reaction, and the nail-shaped particles were collected by centrifugation and redispersion in ethanol. This synthesis method was also successfully repeated on a larger scale (150 mL of PVP/pentanol mixture, in a 250 mL round-bottomed flask). This synthesis is published in Ref [273].

Crooked silica rods. In a typical synthesis, polyvinylpyrrolidone (PVP 0.5 g, Mn = 40 kg/mol, Sigma-Aldrich) was dissolved in 1-pentanol (5 mL, Sigma-Aldrich) using sonication or vortex mixing for 1 h. After complete dissolution of PVP in 1-pentanol, a clear solution was formed; to this solution ethanol (0.5 mL, Interchema, 100%), distilled water (0.14 mL, Millipore system) and an aqueous solution of sodium citrate (0.18 M, 35 μ L, Sigma-Aldrich, 99%) were added in sequence. The reactants were mixed gently. Then, ammonium hydroxide (0.115 mL, Sigma-Aldrich, 28% w/w) was added and mixed vigorously to make an emulsion. 0.05 mL TEOS was added and the reaction mixture was kept at 35 °C for the first hour. Then a small amount of partially-hydrolyzed TEOS (10 v%, 5 μ L) was added. The mixture was homogenized by shaking by hand and transferred to room temperature for 8 h. Eventually, the obtained rods were centrifuged at 1500 *g* for 10 minutes and dispersed in absolute ethanol. This washing step was repeated twice. The partially hydrolyzed TEOS was prepared as follows: 5 mL normal TEOS was mixed with 11 μ L HCl (37% ACS reagent) and 0.40 mL distilled water and vortex mixed for one minute. A detailed synthesis protocol can be found in Ref [274]

5.2.2. In-situ liquid cell etching experiments

A Hummingbird Scientific, (USA) Liquid Cell dedicated holder was used to perform the in-situ experiments. A Hamilton syringe pump equipped with a 1 mL glass syringe was used to flow solutions through the microfluidic tubing into the cell. To flow the 400 nm spherical particles, for measuring the flow velocity, a diluted suspension of the nanoparticles was loaded into the syringe and flowed into the cell. Silicon chips with SiN windows ($50 \times 200 \mu\text{m} \times 50 \text{ nm}$ thickness) were used to encapsulate the liquid

volume. In all experiments, 2 μm spacers were used between the top and bottom chips. The sample preparation started with glow discharging of the side of the chips which was in contact with liquid for 90 seconds to make them hydrophilic. 2 μL of a diluted sample with a volume fraction of 21 g. L^{-1} was drop-casted on the top chip and allowed to dry. This ensured that a number of particles were attached to the top window, where the STEM resolution for the LC experiment is the highest (see chapter 2). Next, the bottom chip was placed in the dedicated holder and 2 μL of deionized water was drop-casted onto it to ensure that the cell contained liquid, after which the top chip was placed in position.

5.2.3. Ex-situ etching experiments

Ex-situ etching of silica rods was carried out as follows. For the experiment on freely dispersed particles the sample volume fraction was fixed at 21 g. L^{-1} (350 mmol. L^{-1}) and 575 μL of this sample in ethanol was redispersed in 20 mL of the desired concentration of aqueous NaOH (reagent grade, $\geq 98\%$, pellets, Sigma-Aldrich) in plastic vials. For the concentrations 100 and 10 mM, NaOH samples were collected every 15 minutes for 8 hours. For the concentration 3 mM NaOH samples were collected every 1 hour for 8 hours and 2 final samples were collected after 20 and 24 hours. For the 0.50 mM NaOH concentration samples were collected every 1 hour for 8 hours and 3 final samples were collected after 24, 48, and 72 hours. All samples were prepared by drop-casting 5 μL of the sample solution on a Formvar/Carbon Film 200 Mesh Copper TEM grid. The grids were dried under a heating lamp to quickly stop the etching reaction on the grid.

For ex-situ experiments where the particles were attached to a SiN membrane of the LC chip the sample volume fraction was fixed at 21 g. L^{-1} and 2 μL of this sample was drop-casted on the LC chip and allowed to dry. The chip was then placed in a plastic vial containing 40 mL of the desired concentration of aqueous NaOH. The vials were left to stand on the table without stirring. The experiments were carried out with 100 mM and 10 mM NaOH concentrations. Samples were collected every 15 minutes for 8 hours and for each time interval a separate SiN chip was utilized.

All LC-STEM experiments and STEM measurements were carried out with a Tecnai-F20 transmission electron microscope (TEM, Thermo Fisher Scientific) equipped with a field emission gun and operating at 200 keV using an annular dark-field detector (ADF, E.A. Fischione Instruments Inc., Model 3000, USA) with a camera length of 120 mm.

5.3. RESULTS AND DISCUSSION

Rod-shaped silica particles were synthesized as described by Kuijk *et al.* [83] (Figure 5.1). In this process, the rod grows from a water-in-oil emulsion droplet which is rich in hydrolyzed TEOS, and because of this anisotropic supply of precursor, the particle grows in one direction. Since the precursor concentration is highest at the start of the

reaction, growth takes place fastest during that stage [84]. The high concentration of the silicon hydrolyzed alkoxide at the beginning of the reaction resulted in a porous structure by the addition of oligomers near the round tip of the rod, whereas the lower concentration near the end of the growth resulted in a more densely condensed structure by the addition of monomers [84,275]. Furthermore, in the radial direction, there was an inhomogeneous composition as well; a low concentration of silicon hydrolyzed alkoxide in the pentanol resulted in the formation of a condensed silica shell around the particle. This shell was thickest for the part that was grown first [84]. The dissolution of silica in alkaline solutions occurs when the hydroxide ion (OH^-) attacks the silicon atom and replaces one of the siloxane bonds in a transition state with coordination number five [45]. In addition, the free energy gain associated with the weakly acidic silanol groups that also strongly increases the solubility of silica at higher pH above ~ 10 .

To better understand the influence of the LC-STEM parameters on our in-situ etching experiments, we initially optimized these parameters to the extent where the effects of the electron beam can be neglected by investigating the effects of varying the flow rate, NaOH concentration, and accumulated electron dose on the resulting LC-STEM observations of the etching mechanism of silica rods. Furthermore, we investigated the effect of the liquid cell geometry on the etching mechanism of these rods by performing ex-situ counterpart experiments as well that could be more directly compared to etching experiments inside the liquid cell.

5.3.1. Static in-situ etching experiments

First, LC-STEM experiments were performed by dispersing the particles in a 100 mM NaOH aqueous solutions and preparing the liquid cell by drop-casting 2 μL of this solution on the SiN chips without flow through the cell. No etching was observed after 60 minutes of continuous imaging of one particle at this high NaOH concentration (Figure 5.2). This is surprising, as silica is expected to dissolve at such a high pH. There are two possible causes for this: The sample volume that we used to prepare the liquid cell was quite small (2 μL). It is likely that the solution became immediately saturated with silicate ions due to the presence of a large number of particles in the small volume of the basic solution, and etching did not take place as the pH decreased by the activity of the resulting silanol groups and the solubility limit was already reached. The higher initial concentration of silica particles (350 mM) compared to the NaOH concentration (100 mM) also roughly confirms this assumption. Another possible explanation is associated with pH changes upon electron beam irradiation in LC-(S)TEM experiments. Calculations involving many radiolysis products, which are always made for pure water and do not take the presence of the silica rods into account, indicated that the pH of the solution in the liquid cell drops upon electron beam irradiation, where alkaline solutions are most strongly affected by the electron beam irradiation [125]. Therefore, the pH

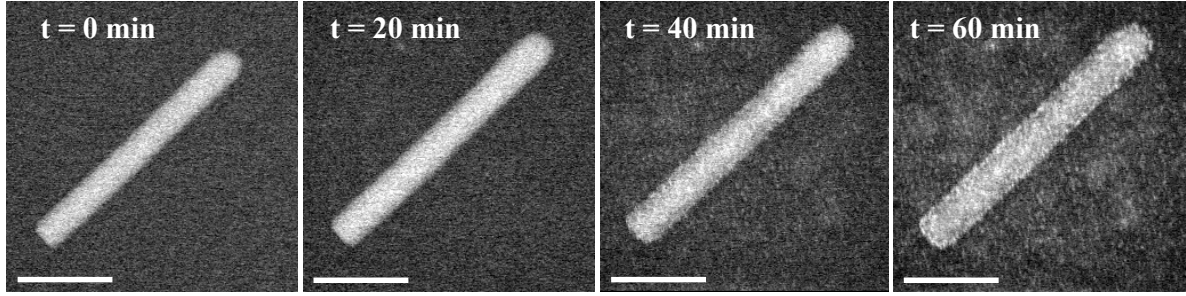


FIGURE 5.2. LC-(S)TEM images of the static etching experiment performed without flowing base inside the cell. The NaOH concentration was 100 mM. The electron dose rate used in this experiment was $18 \text{ e}^- \text{ nm}^{-2} \text{s}^{-1}$. The imaging was performed continuously using a frame time of 5 s. The total accumulated dose after 60 min of imaging was $6.4 \times 10^4 \text{ e}^- \text{ nm}^{-2}$. The scale bar indicates 1 μm .

of the solution could have decreased when it was continuously exposed to the electron beam, thereby inhibiting the etching process. Nevertheless, the LC-STEM observations also show that some dissolved silica redeposits on the surface of the particle and/or on the SiN window in the field of view. This can only have come from the dissolution of some of the rods, which clearly, therefore, is not always visible by looking at changes of the particles! It has been shown that the silica redeposition is strongly related to the electron beam irradiation [127].

5.3.2. Effect of flow rate on in-situ LC-STEM etching experiments

The ability to flow NaOH aqueous solution through the cell enabled us to overcome several of the issues associated with the previous LC-STEM experiment by continuously renewing the basic solution in the cell. We used a syringe pump to flow the NaOH solutions through the cell at a controlled flow rate within the range of $0.1 \mu\text{L} \cdot \text{min}^{-1}$ to $5 \mu\text{L} \cdot \text{min}^{-1}$. Figure 5.3 shows a few image series of the etching process of rod-shaped silica particles in time. In a 50 mM NaOH solution, the etching process was recorded for 6 hours while the solution was flowing through the cell with a flow rate of $0.3 \mu\text{L} \cdot \text{min}^{-1}$. The observations showed that some particles were passing through the field of view. These particles are assumed to be the ones that were diffusing inside the cell from the beginning of the experiment and by flowing the basic solution, they were dragged along the flow direction. However, the particles initially attached to the SiN window remained in the field of view during the complete etching process (6 hours), which enabled us to record the complete etching mechanism of silica rod-shaped particles. We will explain the etching mechanism in the further sections in detail. In order to investigate the effect of the flow rate, we performed several LC-STEM experiments using different flow rates. Supporting Movie 3 shows a video of a LC-STEM experiment using a flow rate of $5 \mu\text{L} \cdot \text{min}^{-1}$. These observations show particles initially attached to the SiN window

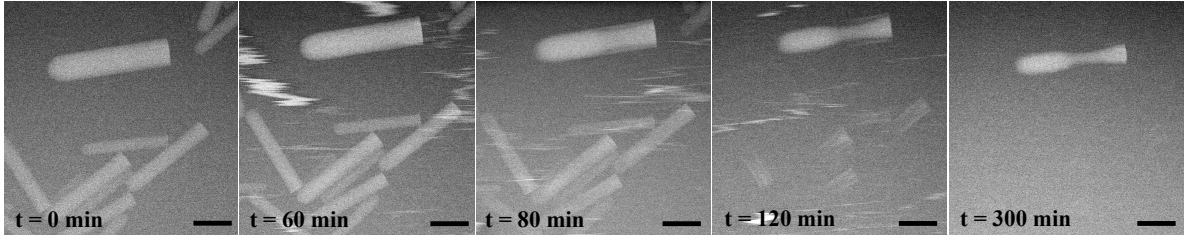


FIGURE 5.3. STEM image series showing an optimized flow rate of basic solutions in silica rods etching process in real-time. The particles were imaged for 6 hours while a 50 mM NaOH solution was flowing through the cell at $0.3 \mu\text{L}\cdot\text{min}^{-1}$. A total number of 94 frames were recorded with an electron dose rate of $7 \text{ e}^-\text{nm}^{-2}\text{s}^{-1}$ and a total accumulated electron dose of $1.1 \times 10^4 \text{ e}^-\text{nm}^{-2}$. Scale bars indicate $1 \mu\text{m}$

detaching from the window and moving out of the field of view 10 minutes after the flow was started. This indicates that a high flow rate can detach all the silica rods from the SiN window within a short time, and observation of the full etching process would not be possible. The NaOH solution slightly etched the particles and made them attach too loosely to the SiN window and the $5 \mu\text{L}\cdot\text{min}^{-1}$ flow rate was capable of detaching these particles from the window. The role of the base in the detachment was confirmed by a reference experiment, where after deionized water with the same flow rate did not detach particles even after 1 hour. Repeating the experiments with different flow rates revealed that observation of the etching process was feasible within the range of $0.1 \mu\text{L}\cdot\text{min}^{-1}$ to $1 \mu\text{L}\cdot\text{min}^{-1}$.

To better understand the effect of the flow rate on the etching process, the drag force on the silica rod-shaped particles was estimated by measuring the flow velocity in the main channel (window) of the liquid cell. To obtain the flow velocity, another LC-STEM experiment was conducted by flowing 400 nm spherical silica particles through the cell. The cell configuration was the same used for the etching of silica rod-shaped particles. The diluted sample was loaded in the syringe and the flow was started with a flow rate of $5 \mu\text{L}\cdot\text{min}^{-1}$. This experiment was repeated for flow rates of 4, 3, 2, and $1 \mu\text{L}\cdot\text{min}^{-1}$ with the same LC. To increase the accuracy of the experiment, image recording was started 20 minutes after changing the pump speed to stabilize the new flow rate. Sequences of images were recorded with a scanning time of 0.5 seconds per image, a total duration of 30 minutes for each flow rate. The image sequences were analyzed by tracking the positions of the particles from image to image (using the MTrackJ plug-in for Image J (Fiji version)). The trajectories recorded at different pump speeds were analyzed to obtain a relationship between the flow velocity v in the main channel and the flow rate setting on the syringe pump. Results shown in Figure 5.4a show that the flow velocity changes linearly with the flow speed setting of the pump. Therefore, for this microfluidic system, it can be concluded that the flow velocity is proportional to the pump speed

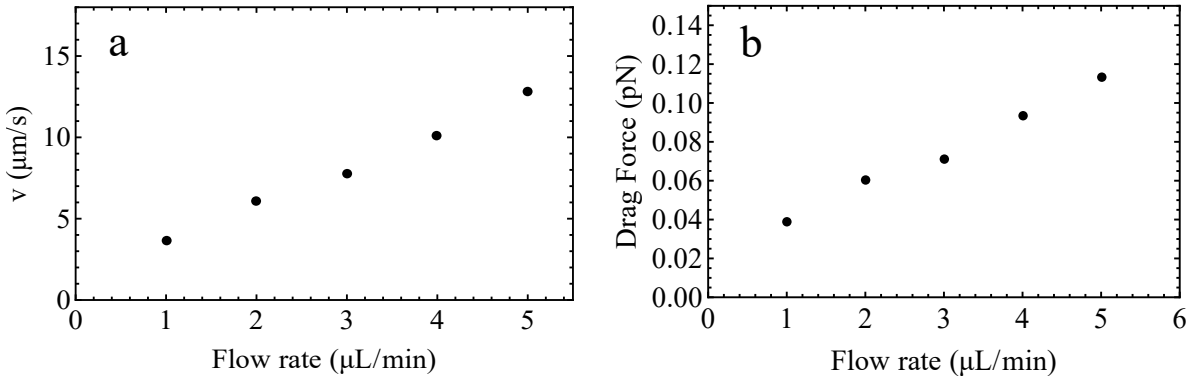


FIGURE 5.4. a) The linear relationship between the flow velocity and the flow rate b) The linear relationship between the drag force on a silica rod-shaped particle with dimensions: $L = 2.6 \mu\text{m}$ $D = 300 \text{ nm}$ and the flow rate. The drag force on the particle for $5 \mu\text{L}\cdot\text{min}^{-1}$ is 3 times bigger than the same for $1 \mu\text{L}\cdot\text{min}^{-1}$.

assuming that the velocity of the particles is a measure of the velocity of the liquid front in the main channel thus neglecting Brownian motion. Knowing the flow velocity the drag force on the rod-shaped silica particles can be estimated as follows:

$$\vec{F}_{drag} = -\xi \vec{v} \quad (5.1)$$

where ξ is the drag coefficient of the rods and \vec{v} is the velocity of the particle relative to the flow. ξ can be found from the expression for the translational diffusion coefficient D_t since the diffusion coefficient is equal to $k_B T \xi^{-1}$. For dilute suspensions, the expression for the translational diffusion coefficient of finite rods, modeled as cylinders, is [276]:

$$D_t = \frac{k_B T (\ln(\frac{L}{D}) + \gamma)}{3\pi\eta_0 L} \quad (5.2)$$

where $k_B T$ is the thermal energy, L the total head-to-tail length of the rod, D the diameter, and η_0 the viscosity of the solvent. The factor γ is the so-called end-effect correction which is a function of the rod dimensions [277] and should be applied when $2 < L/D < 30$:

$$\gamma = 0.312 + 0.565 \frac{D}{L} - 0.100 \left(\frac{D}{L} \right)^2 \quad (5.3)$$

If we derive the drag coefficient ξ from equation 5.2 and insert it in equation 5.1, the drag force for rod-shaped particles can be calculated as follows:

$$\vec{F}_{drag} = -\frac{3\pi\eta_0 L}{\ln(\frac{L}{D}) + \gamma} \vec{v} \quad (5.4)$$

calculations of drag forces for different flow velocities show that the drag force on the particle increases almost linearly with the flow rate (Figure 5.4b). Using a $5 \mu\text{L}\cdot\text{min}^{-1}$ flow rate the drag force is 3 times bigger than when using $1 \mu\text{L}\cdot\text{min}^{-1}$ which according to the LC-STEM observations is enough to wash all the particles away from the SiN

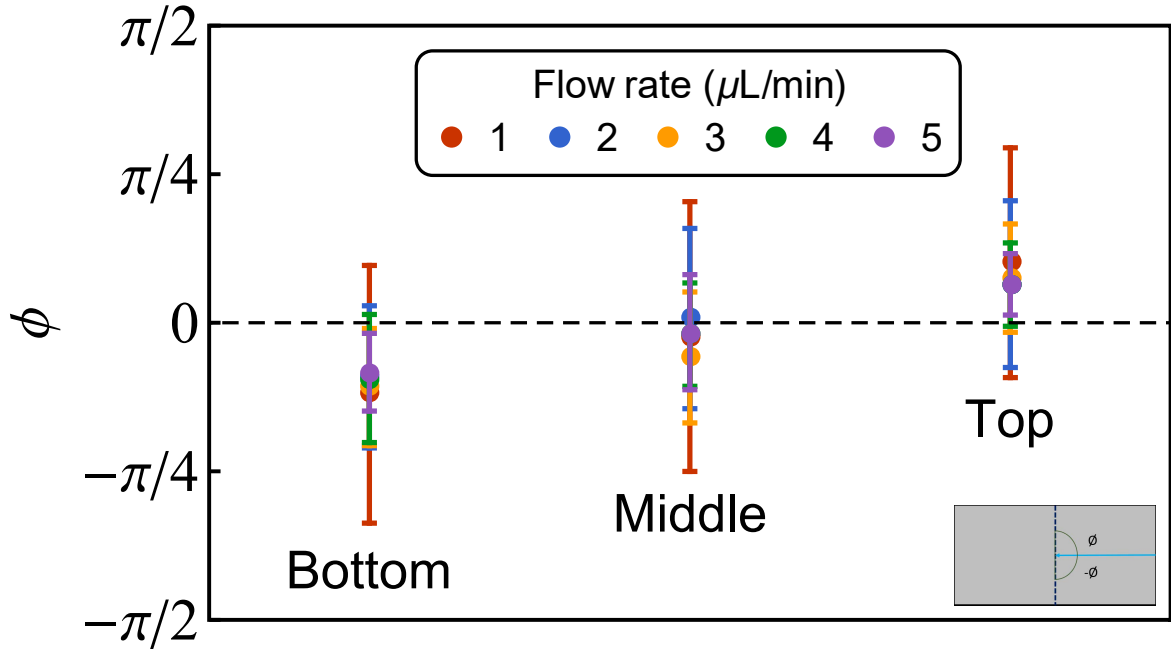


FIGURE 5.5. The direction of motion of particles flowed into the liquid cell

window. The calculations also confirm that the drag force on spherical nanoparticles is too low to remove them from the SiN window even for the highest flow rate in our system ($5 \mu\text{L}\cdot\text{min}^{-1}$). It is noteworthy that equation 5.1 does not take into account the hydrodynamic interactions between the particle and the cell wall. However, since the ratio between drag force for different flow rates is of importance in our study, we neglect this interaction, which is assumed to be proportional to the flow rate.

During the LC-STEM experiment with silica spheres to calculate the flow rate we found another interesting observation. The observation showed that the particles which were flowed into the cell tended to go out of the window (Figure 5.5). This was the case for particles that were coming in the field of view (window) from both the top and the bottom part of the field of view. This also happened regardless of the flow rate. This observation is important for the self-assembly experiments via LC-STEM because for these experiments the maximum number of particles is needed in the field of view.

5.3.3. Effect of base concentration on in-situ etching of silica rods

In order to analyze the dissolution kinetics of silica rod-shaped particles and also the effect of the base concentration on the final shape of the particle, we performed several LC-STEM experiments using three different NaOH concentrations (10 mM, 50 mM, 100 mM) at a fixed flow rate of $0.3 \mu\text{L}\cdot\text{min}^{-1}$ and a fixed electron dose rate of $7 \text{ e}^-\text{nm}^{-2}\text{s}^{-1}$ together with a fixed total accumulated electron dose of $\sim 1000 \text{ e}^-\text{nm}^{-2}$. Since the etching kinetics are strongly size-dependent, we analyzed particles with similar particle

sizes in each experiment. Figure 5.6 shows the effect of the three different NaOH concentrations on the etching mechanism and etching kinetics of silica rods. The time at which the etching became visible was different for each of these base concentrations. The first signs of etching, which happened at a region in the middle of the particle closer to the flat end, was observable after approximately 60 minutes for 100 mM NaOH concentration, observable after about 90 minutes for 50 mM NaOH concentration and after about 120 minutes for 10 mM NaOH concentration. We designate the region of the particle in which the etching started first as the sensitive part of the particle. LC-STEM observations show that initially, the etching rate was the highest at this sensitive part of the particle, while it gradually decreased as the etching proceeded in time. This could be due to the presence of a thin silica shell around the particle which has a higher cross-linked SiO₂ structure acting like a protective layer against etching [84]. This thin silica layer formed around the particle by condensation of TEOS coming from the oil-phase during the synthesis and is more prominent around the rounded tip of the particle since this part was exposed to the growth solution for a longer time and it stayed attached to the SiN membrane during the whole in-situ etching experiment. Furthermore, the flat end of the particle is the most condensed part of the particle due to the slow condensation of silica at this part. Therefore, the LC-STEM observations also suggested that the region in the middle of the particle closer to the flat end was the part of the particle most sensitive to the etchant. The etching process began from this part of the particle and that was the case for all particles with different sizes and for all base concentrations.

5.3.4. Etching mechanism of rod-shaped silica particles

Overall, we found that the etching mechanism of rod-shaped silica particles in a confining LC geometry took place in three main steps based on the LC-STEM observations (Figure 5.7 and supporting Movie 4). By flowing the NaOH solution into the cell, the etching process started and became observable after a certain period of time for each base concentration at the sensitive part of the particle where the silica shell is the weakest. As was mentioned before, it is likely that some silica was already dissolved without this being visible as a change in morphology and/or density of the particles. This starting region of dissolution was the same for all particles regardless of the size of the particle and the base concentration. Nevertheless, the time when the dissolution started to become visible did depend on the particle size. Second, the etching continued by the transport of silica from the inner core through the thin shell in the same region for a while, making this part of the rod thinner in time. Slight etching also happened at the rounded tip and the flat end of the particle, however, the etching rate at these regions was found to be significantly lower than the etching rate at the edge of the sensitive part of the particle, due to the stronger shell around the rounded tip of the particle and

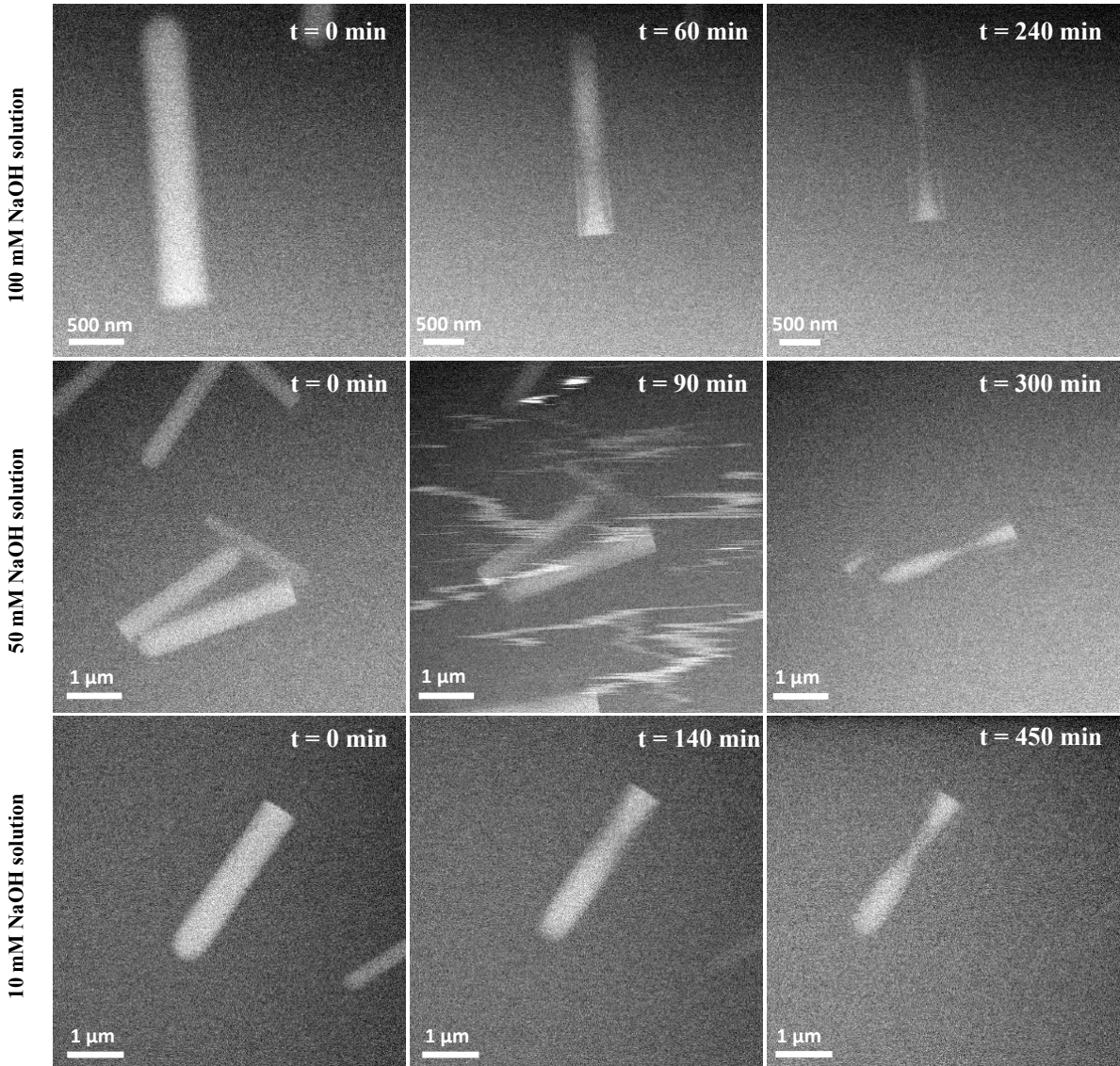


FIGURE 5.6. Etching mechanism of silica rods for different concentrations of NaOH solutions. The flow rate was $0.3 \mu\text{L}\cdot\text{min}^{-1}$, the electron dose rate was $7 \text{ e}^-\text{nm}^{-2}\text{s}^{-1}$, and the total accumulated electron dose was $\sim 1000 \text{ e}^-\text{nm}^{-2}$ for all experiments. The etching process time is different for different base concentrations, however the etching mechanism is the same.

the more condensed structure at the flat end. Finally, after a longer etching period, necking happened at the sensitive region of the particle eventually leading to break off at this point. The resulting shape after this step is a cone-shaped silica particle which has a smaller length compared to the initial rod-shaped particle (see also Supporting movie 4 for a LC-STEM demonstration of the final stage of the etching mechanism). The necking-and-breaking step of the etching process was not previously known from ex-situ experiments [84] and it was only revealed during the direct observation of the etching process at a single particle level using LC-STEM.

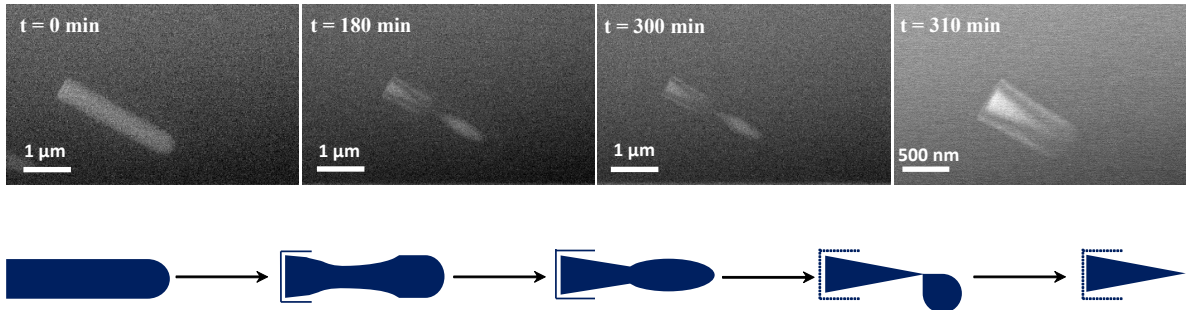


FIGURE 5.7. Three step etching mechanism of rod-shaped silica particles attached to the SiN window in basic solutions revealed by LC-STEM experiments (top), and its schematic representation (bottom). In this experiment the NaOH concentration was 100 mM, the flow rate was $0.3 \mu\text{L}\cdot\text{min}^{-1}$, the electron dose rate was $7 \text{ e}^-\text{nm}^{-2}\text{s}^{-1}$, and the total accumulated electron dose was $\sim 1000 \text{ e}^-\text{nm}^{-2}$

5.3.5. Effect of accumulated electron dose on the etching of silica rods

We also addressed the question concerning the extent to which the observed etching process was influenced by the electron beam irradiation. This influence can be revealed from a change in the rate and/or the mechanism of the etching during the LC-STEM observations. Using a discontinuous imaging approach, we modified the blanking time of the electron beam between recordings of the images of the particles to investigate the accumulated electron dose effects on the etching process. To this end, we exposed the particle to the electron beam irradiation for different periods of time by recording a different total number of frames for each particle while fixing the electron dose rate at $7 \text{ e}^-\text{nm}^{-2}\text{s}^{-1}$ with these imaging conditions: 1024×1024 pixels, $24 \mu\text{s}$ dwell time, and 6.12 nm pixel size. Figure 5.8 shows image series for four distinct particles imaged with different blanking times during the same LC-STEM experiment. During this experiment, a solution of 10 mM NaOH was flowed through the cell at a rate of $0.3 \mu\text{L}\cdot\text{min}^{-1}$. The observations showed that the rate and the mechanism of the etching are the same for all particles when they were imaged with low-dose imaging conditions, regardless of the blanking time duration between the recorded images. Furthermore, an overview of the cell after the etching has stopped showed that all the particles with similar sizes etched by the same mechanism and at the same rate. This indicates that imaging the etching process of rod-shaped silica particles with low accumulated electron dose did not alter the rate nor the mechanism of the etching process for total doses less than $3.4 \times 10^4 \text{ e}^-\text{nm}^{-2}$ since the accumulated electron dose never reached a threshold with the capability of affecting the chemical process. Therefore with a negligible effect of electron beam irradiation, investigations of the etching process of this system of particles were successfully achieved. It is noteworthy that the maximum accumulated

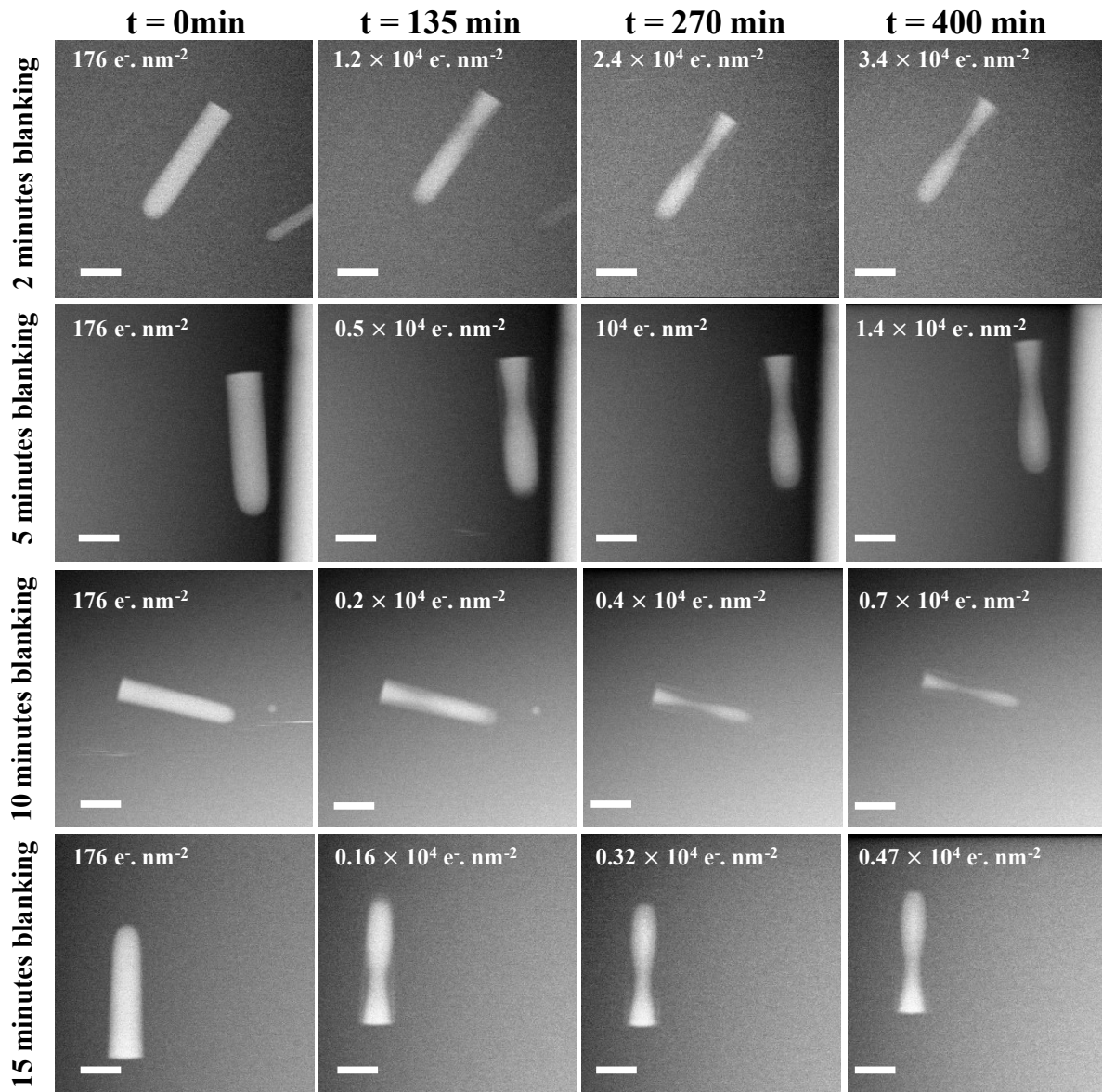


FIGURE 5.8. STEM image series of four distinct particles imaged with different beam blanking time indicating different accumulated electron dose ($\text{e}^- \text{nm}^{-2}$) on each particle. The corresponding total accumulated electron dose is shown on each frame.

electron dose used in this chapter was several order of magnitude lower than those used in chapter 2, where the particles were strongly affected by the electron beam irradiation.

5.3.6. Effect of confining geometry and sticking of particle as opposed to Brownian motion

Finally, ex-situ experiments with the same particles and the same etchant were performed in order to compare with the LC-STEM observations. The ex-situ part was carried out in two main experiments. First, the sample was prepared exactly like

the in-situ sample preparation: 2 μ L of the sample solution was drop-casted on one of the liquid cell chips and left to dry at room temperature to assure that a number of particles were attached to the SiN window. Subsequently, these chips were each placed in a plastic bottle filled with 40 mL of aqueous NaOH. 100 mM and 10 mM NaOH solutions were used for these experiments. The vials were left to stand without stirring. One sample was retrieved from its solution every 15 minutes for 7 hours after placing the chips in the bottle. For each etching time, a separate SiN chip was used in a separate bottle. Next, samples were inspected with STEM using a normal TEM holder. The STEM images confirmed that the mechanism of ex-situ etching for the particles that were attached to the SiN window is the same as the in-situ etching mechanism where the rod-shaped silica particles turned into cone-shaped silica particles via necking-and-breaking procedure. Figure 5.9, a and b, show the end result for this ex-situ etching experiment (data not shown for each etching time).

Next, the silica rods were redispersed in NaOH aqueous solutions. This ex-situ etching experiment was performed with 0.5, 3, 10, and 100 mM NaOH concentrations. The samples were collected by dipping a conventional TEM grid in each solution every 15 minutes and were subsequently imaged with STEM. Figure 5.9, c-f, show the end result of etching of rod-shaped silica particles that were freely dispersed during etching, for different base concentrations (data not shown for each etching time). Etching at low base concentrations (0.50 mM) showed the same mechanism as the LC observations for the etching of these particles. However, at higher base concentrations such as 10 and 100 mM, the etching mechanism was different from the mechanism observed in the LC experiments. The STEM images show that the particles at higher base concentrations turned into sharper cone-shaped silica particles with a larger length, indicating that the etching also occurred at the tip of these particles. Moreover, it is also observed that the ex-situ etching at moderate base concentrations such as 3 mM shows both mechanisms with a dependence on the particle size (Figure 5.9, d). We propose that this difference in final shape is due to the presence of a higher cross-linked SiO₂ shell around the particle along with the absence of diffusion inside the LC. The shell around the particle became thinner going from the rounded tip to the flat end because the exposure time to the growth solution decreased in this direction. Therefore, when the base concentration was high enough it completely etched this silica shell around the particle and etching took place at the tip of the particle at higher etching rates, resulting in a sharper cone-shaped particle. On the other hand, at lower base concentrations only the weakest part of the silica shell etched away and etching continued in the same region by the transport of silica from the inner core through the thin shell which caused the particle to break off at this point. The difference between LC etching and ex-situ etching where particles undergo free diffusion can be explained by the fact that the particles experience different local NaOH concentrations when they have Brownian motion in the basic solution. In

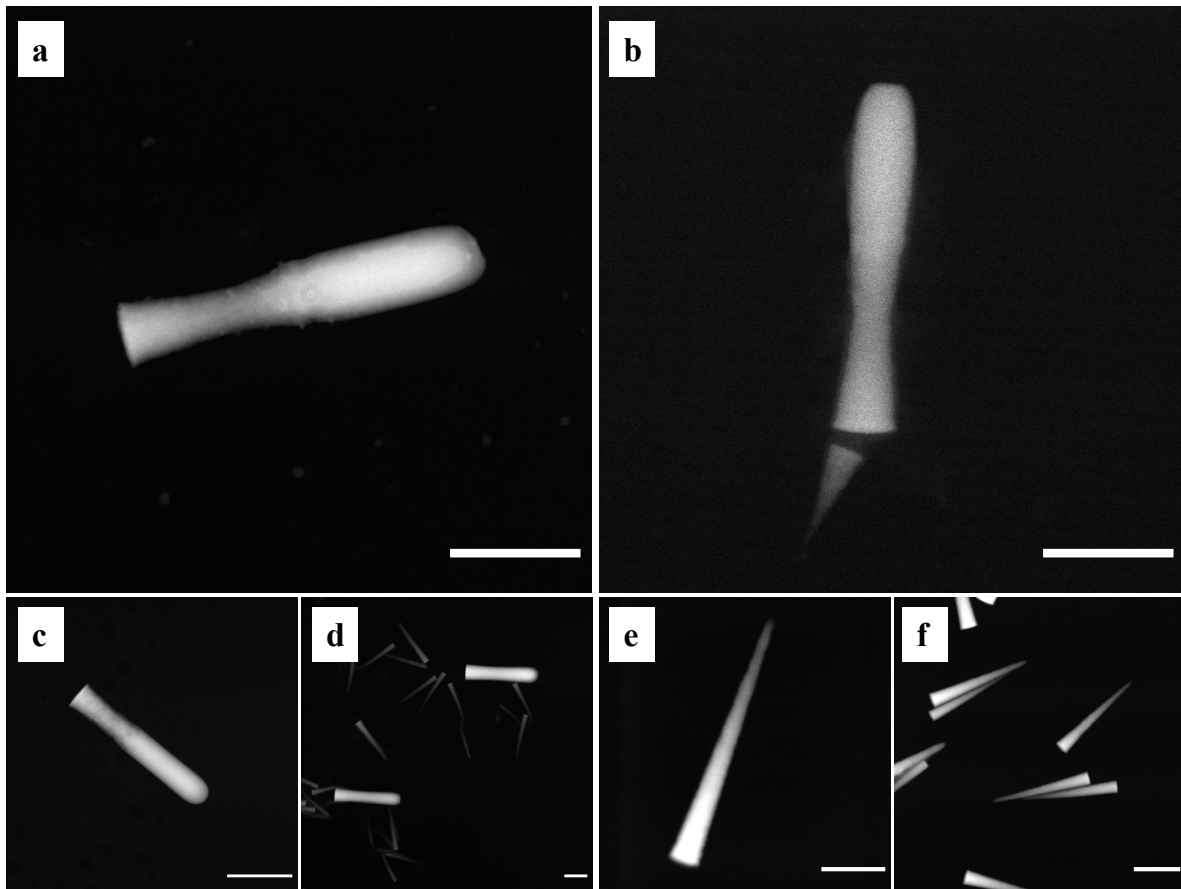


FIGURE 5.9. Ex-situ etching of silica rod-shaped particles in a basic solution. Particles were attached to the SiN window and placed in a bottle containing 40 mL of (a) 10 mM, and (b) 100 mM NaOH aqueous solutions without stirring. Particles not attached but freely dispersed in a bottle containing 20 mL of (c) 0.5 mM, (d) 3 mM, (e) 10 mM, and (f) 100 mM NaOH solutions. Scale bars indicate 1 μm for (a-d,f), and 500 nm for (e).

the LC experiments and ex-situ control experiment particles were attached to the SiN window and the etching reaction took place in a diffusion-limited regime. Since the highly cross-linked silica shell was always attached to the SiN window during the whole etching process NaOH always diffused from the weakest part of the shell and etching continued in that region with higher etching rates. However, in the ex-situ etching process where the particles diffused freely inside the basic solution the shell around the particle detached at some point due to the self-stirring effect of colloidal particles and etching continued at the tip of the particle with higher etching rates resulting in sharper cone-shaped silica particles. These results reveal that the final shape of the particles can be also tuned by immobilizing them through attachment to a substrate or having them move freely in the solution. However, the higher yields obtainable through bulk

etching makes the approach in which the base concentration is optimized for the desired geometries more appealing.

5.3.7. In-situ etching of segmented silica rods

As the last validation for LC-STEM parameters to perform an in-situ silica etching experiment, we analyzed segmented silica rods with a known, even more, complex internal inhomogeneous chemical composition by in-situ LC etching experiments. Segments of silica rods were grown under different temperature conditions. This adds differences in the internal siloxane condensation degree on top of those already discussed. Varying the temperature influences the degree of condensation of silica. A lower temperature resulted in a lower degree of condensation with a faster dissolution rate, whereas an increased temperature resulted in a higher degree of condensation and thus a network that dissolves more slowly [39, 275]. It is also known that silica particles grown at lower temperatures have an increased diameter as the solubility of water in the pentanol oil phase is reduced [86]. Nail-shaped silica rods consisting of a segment grown at 50 °C followed by a segment grown at 5 °C were etched by flowing 100 mM NaOH solution in to the LC with these experimental conditions: 0.3 $\mu\text{L}\cdot\text{min}^{-1}$ flow rate, 4 $\text{e}^-\text{nm}^{-2}\text{s}^{-1}$ electron dose rate, and $1.4 \times 10^4 \text{ e}^-\text{nm}^{-2}$ accumulated electron dose. As expected, etching took place at the less condensed silica part grown at low temperature even though it was initially thicker, whereas the segment grown at high temperature seems to have remained untouched [86] (Figure 5.10, panel a). As a further illustration, Using the same experimental conditions another LC experiment was performed with rods grown at 5 °C followed by a segment grown at 25 °C, and the tip of the particle was preferentially etched as expected [86]. (Figure 5.10, panel b). With a three-step growth of silica rods subsequently at 25 °C, 5 °C, and 25 °C, silica particles with a thicker but less condensed middle part were synthesized. The in-situ etching results for this kind of silica rods are shown in Figure 5.10, panel c. The LC-STEM observations with the same mentioned experimental conditions agree with the previous results shown by our group [86] for ex-situ etching of these particles in bulk. Consequently, the required conditions determined in this work for conducting LC-STEM chemical etching experiments of silica rods are applicable to similar systems with a negligible effect of the electron beam as well as of the LC geometry.

5.3.8. Chemical structure of crooked rod-shaped silica particles

Altering the reaction temperature of the rod-shaped silica particles and/or changing the hydrolysis rate of silica precursor by introducing partially hydrolyzed TEOS (pre-TEOS) into the reaction system result in bending of the rod-shaped silica particles. The synthesis procedure starts with synthesizing normal rod-shaped silica particles using standard existing procedures [83], however, the reaction was carried out above room temperature (35 °C). After one hour of reaction, pre-TEOS was added and the

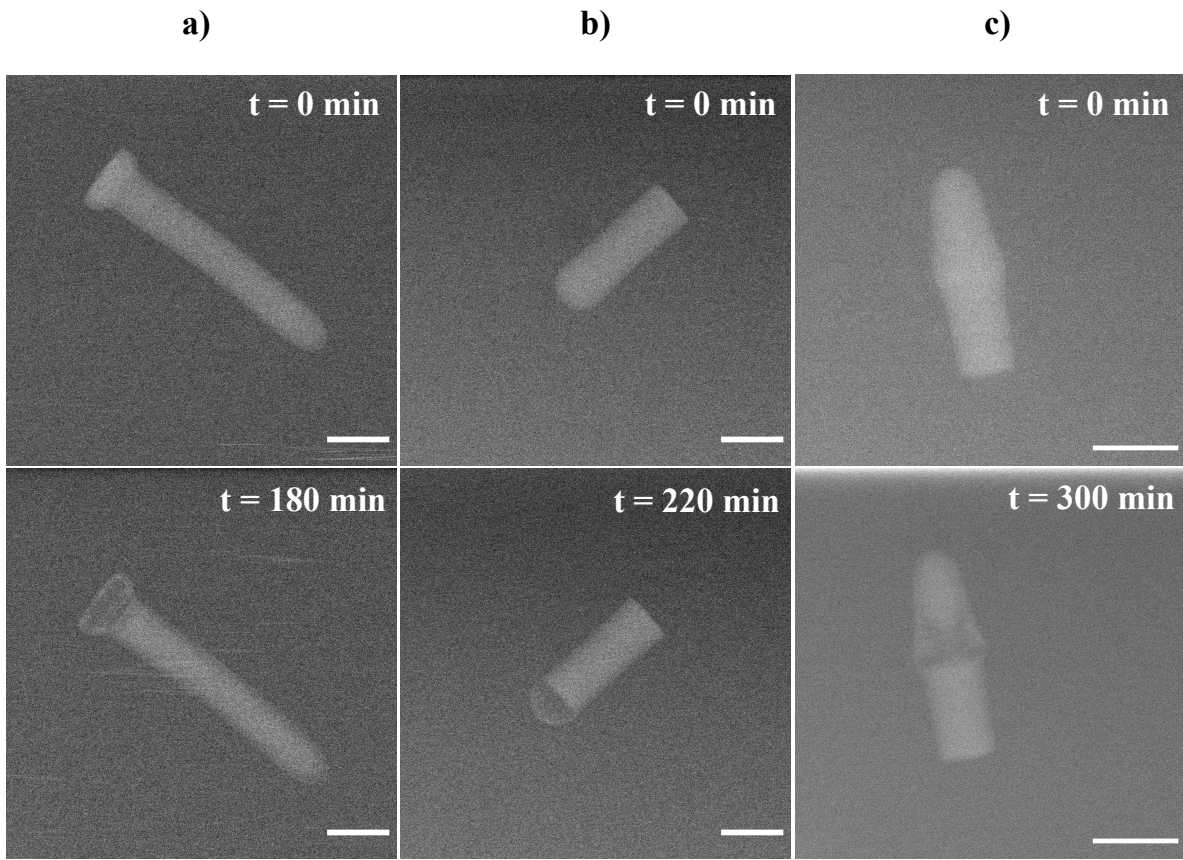


FIGURE 5.10. STEM image series of 3 types of silica rods with different chemical composition and their etched shape with 100 mM NaOH solution using low-dose LC-STEM technique. a) Silica rods consisting of a segment grown at 50 °C followed by a segment grown at 5 °C. b) Silica rods grown at 5 °C followed by a segment grown at 25 °C. c) Silica rods grown subsequently at 25 °C, 5 °C and 25 °C [273]. Details of synthesis in Methods section. The scale bars indicate 500 nm.

solution was homogenized by shaking for ~1 min. Five minutes after the addition of pre-TEOS, the reaction mixture was transferred to room temperature for 6–8 hours. As a result, the rods grew into two segments connected at an angle. It is assumed that the addition of pre-hydrolyzed TEOS initiates an interval of more rapid condensation and therefore was also seen [85] at the surface of the emulsion droplet and thereby the droplet was seen to shrink [274], and growth of the normal rod was interrupted. Most likely, the reaction temperature also enhanced the shrinking of the droplet by the increased dissolution of water in the pentanol phase and boosted the hydrolysis and condensation of the pre-TEOS. Later the content of the emulsion droplet was seen to move out and initiated the growth of the second segment in a different direction w.r.t. first part of the silica rod, thus forming a bent rod with interesting phase behavior [270, 271]. This

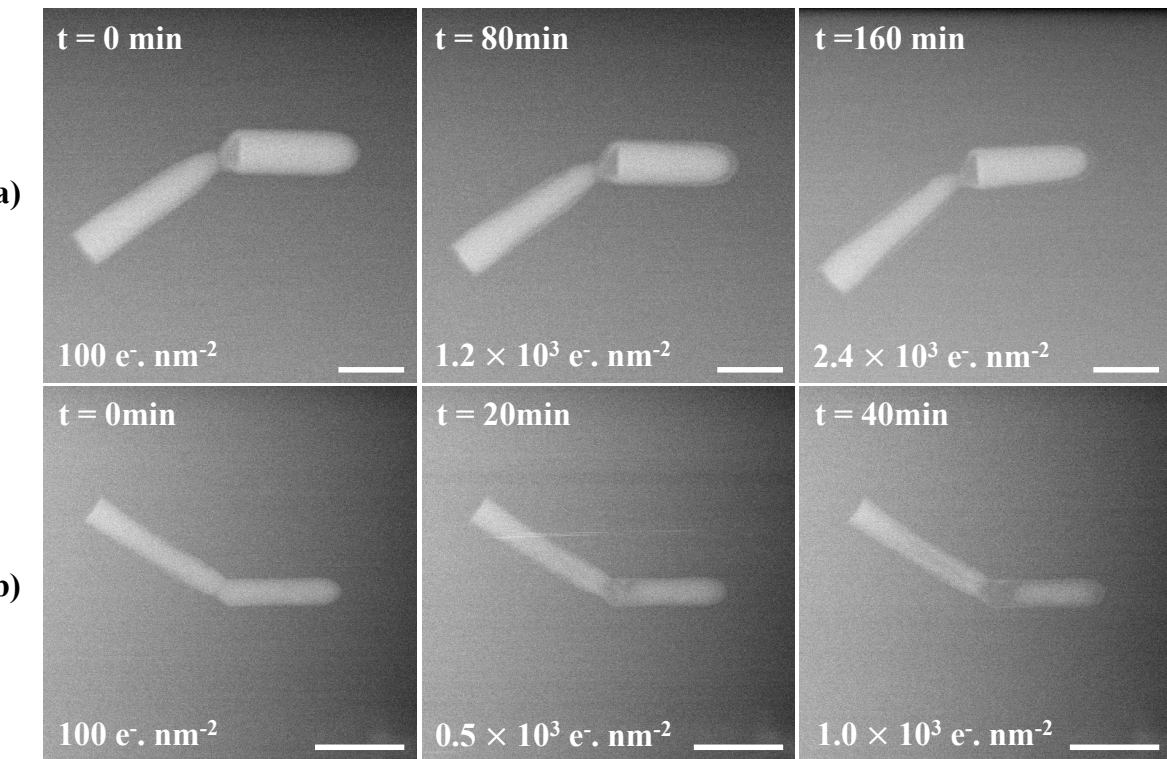


FIGURE 5.11. STEM image series of 2 types of bent silica rods and their etched shape with 100 mM NaOH solution using low-dose LC-STEM technique ($4 \text{ e}^- \text{ nm}^{-2} \text{s}^{-1}$ electron dose rate). The corresponding total accumulated electron dose is shown on each frame.a) The bent silica rods that were synthesized at 35°C with high concentration pre-TEOS. b) The bent silica rods that were synthesized at room temperature using low concentration pre-TEOS. See methods section for details. The scale bars indicate $1 \mu\text{m}$

reaction can also be carried out at room temperature with lower concentrations of pre-TEOS [274]. For synthesis details on the two types of crooked particles investigated see the methods section. Here, we investigated the chemical structure of these two types of crooked silica rods by in-situ etching of these particles in basic solutions via LC-STEM. The results help to better understand the effect of the temperature and the pre-TEOS concentration on the chemical structure of these intriguing particle systems and can be used to tune the bending angle of the two segments, which is important for self-assembly studies.

After finding the optimized LC-STEM conditions to study the in-situ etching of silica rod-shaped particles we applied these parameters to investigate the chemical structure of crooked rod-shaped particles. We flowed 100 mM NaOH solutions with a flow rate of $0.3 \mu\text{L} \cdot \text{min}^{-1}$ and imaged the particles using a $4 \text{ e}^- \text{ nm}^{-2} \text{s}^{-1}$ electron dose rate. with a total accumulated electron dose below $2.8 \times 10^3 \text{ e}^- \text{ nm}^{-2}$. Figure 5.11 shows the etching of crooked silica rods in time. The particle in panel (a) consists of two segments; the

first segment with a rounded tip was grown at 35 °C while the other segment with a flat end was grown at room temperature. The LC-STEM observations show that the etching of the segment with the flat end occurred faster than the other segment with the round tip. This is expected since the silica grown at elevated temperatures is more condensed compared to the silica which was grown at room temperature [45]. Interestingly no etching was observed at the neck of the particle where two segments were connected to each other. This can be explained by the fact that adding concentrated pre-TEOS at that point of reaction forms a condensed silica shell around the joint part of the particle which protected it from etching. The particle in panel (b) was grown completely at room temperature using less concentrated pre-TEOS. Although adding pre-TEOS caused the bending of the particle, the two segments were not completely separated. The in-situ etching of this particle showed that the least condensed part of the particle was the bending point. The etching was observable at the bent region of the particle in approximately 15 minutes after the flowing of the 100 mM NaOH solution. Then the etching continued in both sides of the particle indicating the same silica structure of the bent rod-shaped particle. Apparently having less concentrated pre-TEOS was not enough to protect the bent part of the particle from etching. Moreover, growing at room temperature made particles with less condensed silica structure that can be easily etched with 100 mM NaOH solution in a short time.

5.4. CONCLUSION

We present an optimized LC-STEM method to investigate the etching of micron-sized rod-shaped silica particles in real-time and at the single-particle level with high spatial resolution. A model system of rod-shaped silica colloidal particles was used to investigate the etching mechanism of these particles in basic conditions. By utilizing low-dose electron beam conditions and by optimizing the flow-rate of the NaOH solutions during the LC-STEM observations, we showed that investigation of the etching of rod-shaped silica particles is attainable with a negligible effect of the electron beam irradiation if also the total dose is kept below $3.4 \times 10^4 \text{ e}^- \text{ nm}^{-2}$ by only taking a limited number of images. LC-STEM observations revealed that the base-induced etching occurs inhomogeneously along the length of the rod due to its inhomogeneous chemical structure. Remarkably, the LC-STEM observations revealed a three-step etching mechanism which transformed the rod-shaped silica particles into cone-shaped silica particles. The mechanism started with etching at a region in the middle of the particle closer to the flat end which is the most etchant-sensitive part of the particle. The etching then continued at a faster rate in the sensitive part of the particle and finally necking-and-breaking occurred at the same point of the particle which yielded a cone-shaped silica particle. Comparison between the LC and the ex-situ etching experiments suggests that the geometry of the LC played a significant role in chemical reactions where diffusion of reactants and/or particles are important and with the current equipment for LC experiments the reactions studied in this chapter were in a diffusion-limited regime. The LC-STEM conditions were further validated by utilizing a new class of silica rod-shaped particles where the chemical structure of the rod was tailored deliberately. The etching of segmented silica rods happened as was expected, validating the LC-STEM optimized conditions found in this work. Finally, using these LC-STEM conditions we revealed the chemical composition of the recently developed rod-shaped silica particles known as crooked silica rods. We expect that using similar low-dose imaging conditions and optimized flow-rates of solutions as determined in this work, will allow for investigations of chemical reactions with colloids using the LC-(S)TEM technique with negligible effects of the electron beam, and will thus serve as a powerful new technique to probe the evolution of etching at the single-particle level. Furthermore, we are confident that, although the imaging conditions w.r.t. dose rates and accumulated doses were only possible with the relatively large particles used, future, and ongoing improvements of detectors and smart imaging routines will strongly push down the size and structures that can be imaged without major interference from the imaging itself! Especially, not taking continuous movies, but just a few frames is often enough to still obtain the necessary information.

5.5. ACKNOWLEDGEMENTS

We wish to thank Albert Grau Carbonell and Tom Welling for the critical reading of the chapter. We also thank Rama Kotni for synthesizing crooked silica rods and Fabian Hagemans for synthesizing segmented silica rods. We thank Marlous Kamp for synthesizing nail-shaped silica rods. The authors also acknowledge the EM square center at Utrecht University for access to the microscopes.

APPENDIX 1: SUPPLEMENTARY FIGURES

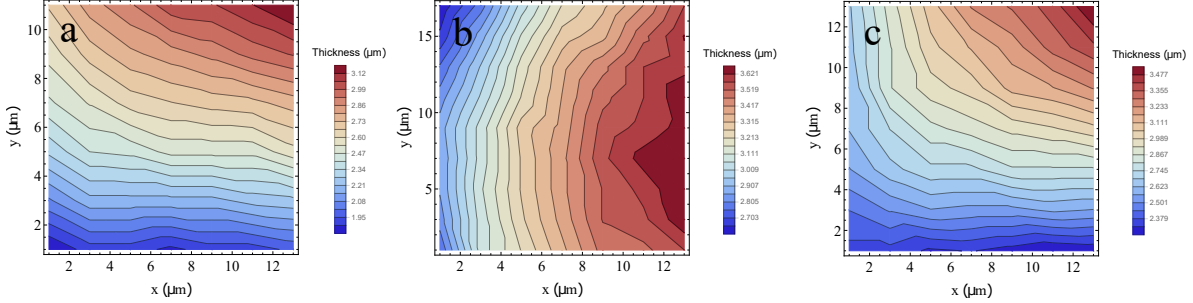


FIGURE S5.1. The thickness map of the LC window with a $2 \mu\text{m}$ spacer a) bottom right corner b) middle right c) top right corner. The liquid thickness was calculated via the method reported by Verch et al: [123]

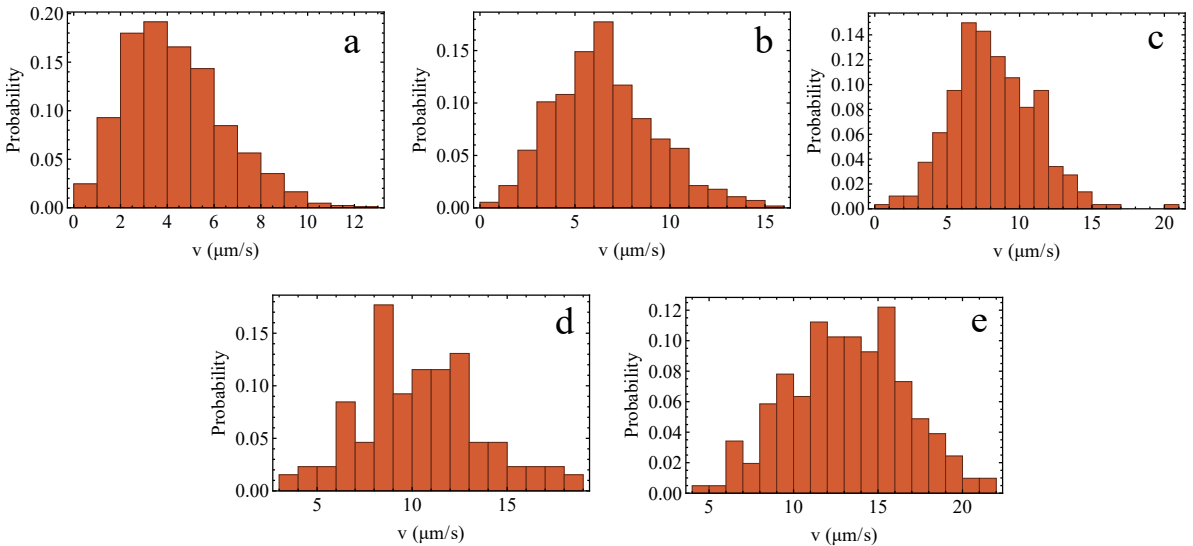
$$\frac{I_{\text{screen}}}{I_0} = \exp\left(-\left(\frac{t_{\text{SiN}}}{I_{\text{SiN}}} + \frac{t_{\text{liquid}}}{I_{\text{liquid}}}\right)\right).$$


FIGURE S5.2. Flow velocity histogram for various flow rates: a) $1 \mu\text{L}\cdot\text{min}^{-1}$, b) $2 \mu\text{L}\cdot\text{min}^{-1}$, c) $3 \mu\text{L}\cdot\text{min}^{-1}$, d) $4 \mu\text{L}\cdot\text{min}^{-1}$, e) $5 \mu\text{L}\cdot\text{min}^{-1}$. The frame time is 0.5 seconds.

APPENDIX 2: SUPPLEMENTARY MOVIES

Supporting Movie 3

LC-STEM movie showing particles initially attached to the SiN window detaching from the window and moving out of the field of view 10 minutes after the flow was started with a flow rate of $5 \mu\text{L}\cdot\text{min}^{-1}$. The movie is accelerated by a factor of 5 with respect to real-time.

[https://drive.google.com/file/d/1wIRWTUMs_pVjQ-3-mws2lz6tGleNVzju/view?
usp=sharing](https://drive.google.com/file/d/1wIRWTUMs_pVjQ-3-mws2lz6tGleNVzju/view?usp=sharing)



FIGURE S5.3. Corresponding QR code for supporting movie 3

Supporting Movie 4

LC-STEM demonstration of the final stage of the etching mechanism where the particle breaks off from the sensitive part of it after necking occurs from the same part due to basic etching. The movie is accelerated by a factor of 5 with respect to real-time.

[https://drive.google.com/file/d/1yzC6rLqL8mW88uUrnG31MwLwvxDDYRBw/view?
usp=sharing](https://drive.google.com/file/d/1yzC6rLqL8mW88uUrnG31MwLwvxDDYRBw/view?usp=sharing)



FIGURE S5.4. Corresponding QR code for supporting movie 4

Bibliography

- [1] W. B. Russel, D. A. Saville, and W. R. Schowalter. *Colloidal Dispersions*. Cambridge Monographs on Mechanics. Cambridge University Press, 1989.
- [2] I. W. Hamley. *Introduction to Soft Matter: Colloids*. John Wiley & Sons, Ltd, 2007.
- [3] I. W. Hamley. *Introduction to Soft Matter: Liquid Crystals*. John Wiley & Sons, Ltd, 2007.
- [4] A. P. Philipse. *Brownian Motion: Elements of Colloid Dynamics, Undergraduate Lecture Notes in Physics*. Springer International Publishing, New York, 2018.
- [5] D. H. Deutsch. Did Brown observe Brownian motion: probably not. *Bull. Amer. Phys. Soc.*, 36:1374, 1991.
- [6] G. Cadée. Brownian motion. *Nature*, 354:180, 1991.
- [7] R. Brown. A brief account of microscopical observations made in the months of June, July and August, 1827, on the particles contained in the pollen of plants and the general existence of active molecules. *printed privately*, London, 1828.
- [8] D. H. Deutsch. Brownian motion. *Nature*, 357:354, 1992.
- [9] B. J. Ford. Brown's observations confirmed. *Nature*, 359:265, 1992.
- [10] A. Einstein. Über die von der molekularkinetischen Theorie der Wärme geforderte Bewegung von in ruhenden Flüssigkeiten suspendierten Teilchen. *Annalen der Physik*, 322(8):549–560, 1905.
- [11] R. Newburgh, J. Peidle, and W. Rueckner. Einstein, Perrin, and the reality of atoms: 1905 revisited. *American Journal of Physics*, 74(6):478–481, 2006.
- [12] U. Gasser, E. R. Weeks, A. Schofield, P. N. Pusey, and D. A. Weitz. Real-space imaging of nucleation and growth in colloidal crystallization. *Science*, 292(5515):258–262, 2001.
- [13] D. G. Grier and C. A. Murray. The microscopic dynamics of freezing in supercooled colloidal fluids. *The Journal of Chemical Physics*, 100(12):9088–9095, 1994.
- [14] K. Sandomirski, S. Walta, J. Dubbert, E. Allahyarov, A. B. Schofield, H. Löwen, W. Richtering, and S. U. Egelhaaf. Heterogeneous crystallization of hard and soft spheres near flat and curved walls. *European Physical Journal: Special Topics*, 223(3):439–454, 2014.
- [15] P. N. Pusey. In *Liquids, Freezing and Glass Transition* (editors: J.P. Hansen, D. Levesque & J. Zinn-Justin). North-Holland, Amsterdam, 1991.
- [16] C. P. Royall, M. E. Leunissen, A. P. Hyyninen, M. Dijkstra, and A. van Blaaderen. Re-entrant melting and freezing in a model system of charged colloids. *Journal of Chemical Physics*, 124(24):1–8, 2006.
- [17] B.V. Derjaguin and L. Landau. Theory of the stability of strongly charged lyophobic sols and of the adhesion of strongly charged particles in solution of electrolytes. *Acta Phys. Chim.*, 14:633–662, 1941.
- [18] E.J.W. Verwey and J.T.G. Overbeek. *Theory of the stability of lyophobic colloids: the interaction of sol particles having an electric double layer*. New York, Elsevier Pub. Co, 1948.
- [19] J. N. Israelachvili. Van der Waals Forces. In Jacob N Israelachvili, editor, *Intermolecular and Surface Forces*, pages 107–132. Academic Press, Boston, third edition, 2011.
- [20] C. J. van Oss. A Review of: “Colloidal Hydrodynamics.” T. G. M. van de Ven. Academic Press, London and New York, 1989. *Journal of Dispersion Science and Technology*, 11(5):548–549, 1990.

- [21] J. W. Goodwin, R. H. Ottewill, and R. Pelton. Studies on the preparation and characterization of monodisperse polystyrene latices. V.: The preparation of cationic latices. *Colloid & Polymer Science*, 257(1):61–69, 1979.
- [22] G. Bosma, C. Pathmamanoharan, E. H. A. de Hoog, W. K. Kegel, A. van Blaaderen, and H. N. W. Lekkerkerker. Preparation of monodisperse, fluorescent PMMA-latex colloids by dispersion polymerization. *Journal of Colloid and Interface Science*, 245(2):292–300, 2002.
- [23] B. Peng, E. van der Wee, A. Imhof, and A. van Blaaderen. Synthesis of monodisperse, highly cross-linked, fluorescent PMMA particles by dispersion polymerization. *Langmuir*, 28(17):6776–6785, 2012.
- [24] A. van Blaaderen, J. van Geest, and A. Vrij. Monodisperse colloidal silica spheres from tetraalkoxysilanes: Particle formation and growth mechanism. *Journal of Colloid And Interface Science*, 154(2):481–501, 1992.
- [25] A. van Blaaderen and A. Vrij. Synthesis and Characterization of Colloidal Dispersions of Fluorescent, Monodisperse Silica Spheres. *Langmuir*, 8(12):2921–2931, 1992.
- [26] A. F. Demirörs, A. van Blaaderen, and A. Imhof. A general method to coat colloidal particles with titania. *Langmuir*, 26(12):9297–9303, 2010.
- [27] A. F. Demirörs, A. Jannasch, P. D. J. van Oostrum, E. Schäffer, A. Imhof, and A. van Blaaderen. Seeded growth of titania colloids with refractive index tunability and fluorophore-free luminescence. *Langmuir*, 27(5):1626–1634, 2011.
- [28] M. A. Haq, Y. Su, and D. Wang. Mechanical properties of PNIPAM based hydrogels: A review. *Materials Science and Engineering C*, 70:842–855, 2017.
- [29] W. Stöber, A. Fink, and E. Bohn. Controlled growth of monodisperse silica spheres in the micron size range. *Journal of Colloid and Interface Science*, 26(1):62–69, 1968.
- [30] K. Osseo-Asare and F. J. Arriagada. Preparation of SiO₂ nanoparticles in a non-ionic reverse micellar system. *Colloids and Surfaces*, 50(C):321–339, 1990.
- [31] T. Yokoi, Y. Sakamoto, O. Terasaki, Y. Kubota, T. Okubo, and T. Tatsumi. Periodic arrangement of silica nanospheres assisted by amino acids. *Journal of the American Chemical Society*, 128(42):13664–13665, 2006.
- [32] T. Yokoi, J. Wakabayashi, Y. Otsuka, W. Fan, M. Iwama, R. Watanabe, K. Aramaki, A. Shimojima, T. Tatsumi, and T. Okubo. Mechanism of formation of uniform-sized silica nanospheres catalyzed by basic amino acids. *Chemistry of Materials*, 21(15):3719–3729, 2009.
- [33] T. M. Davis, M. A. Snyder, J. E. Krohn, and M. Tsapatsis. Nanoparticles in Lysine-Silica Sols. *Chemistry of Materials*, 18(25):5814–5816, 2006.
- [34] M. A. Snyder, J. A. Lee, T. M. Davis, L. E. Scriven, and M. Tsapatsis. Silica Nanoparticle Crystals and Ordered Coatings Using Lys-Sil and a Novel Coating Device. *Langmuir*, 23(20):9924–9928, 2007.
- [35] T. W. Zerda and G. Hoang. High-pressure raman study of the hydrolysis reaction in tetramethylorthosilicate (TMOS). *Journal of Non-Crystalline Solids*, 109:9–17, 1989.
- [36] T. W. Zerda and G. Hoang. Effect of Solvents on the Hydrolysis Reaction of Tetramethyl Orthosilicate. *Chemistry of Materials*, 2(4):372–376, 1990.
- [37] Y. Han, Z. Lu, Z. Teng, J. Liang, Z. Guo, D. Wang, M. Y. Han, and W. Yang. Unraveling the growth mechanism of silica particles in the stöber method: In situ seeded growth model. *Langmuir*, 33(23):5879–5890, 2017.
- [38] G. H. Bogush, M. A. Tracy, and C. F. Zukoski IV. Preparation of monodisperse silica particles: control of size and mass fraction. . *Journal of Non-Crystalline Solids*, 104:95–106, 1988.

- [39] A. van Blaaderen and A. P. M. Kentgens. Particle morphology and chemical microstructure of colloidal silica spheres made from alkoxy silanes. *Journal of Non-Crystalline Solids*, 149:161–178, 1992.
- [40] S. Li, Q. Wan, Z. Qin, Y. Fu, and Y. Gu. Unraveling the Mystery of Stöber Silica's Microporosity. *Langmuir*, 32(36):9180–9187, 2016.
- [41] S. Li, Q. Wan, Z. Qin, Y. Fu, and Y. Gu. Stöber silica's microporosity: Insights from thermal analysis studies. *Journal of Thermal Analysis and Calorimetry*, 136(5):1895–1904, 2019.
- [42] J. Rouquerol, D. Avnir, C.W. Fairbridge, D.H. Everett, J.H. Haynes, N. Pernicone, J.D.F. Ramsay, K.S.W. Sing, and K.K. Unger. Recommendations for the characterization of porous solids (Technical Report). *Pure & Appl. Chem*, 66(8):1739–1758, 1994.
- [43] C. L. Chang and H. S. Fogler. Kinetics of Silica Particle Formation in Nonionic w/o Microemulsions from TEOS. *AICHE Journal*, 42(11):3153–3163, 1996.
- [44] F. J. Arriagada and K. Osseo-Asare. Phase and dispersion stability effects in the synthesis of silica nanoparticles in a non-ionic reverse microemulsion. *Colloids and Surfaces*, 69(2-3):105–115, 1992.
- [45] C.J. Brinker. Hydrolysis and Condensation of Silicates: Effects on structure. *Journal of Non-Crystalline Solid*, 100(130):31–50, 1988.
- [46] F. J. Arriagada and K. Osseo-Asare. Synthesis of Nanosize Silica in a Nonionic Water-in-Oil Microemulsion: Effects of the Water/Surfactant Molar Ratio and Ammonia Concentration. *Journal of colloid and interface science*, 211(2):210–220, 1999.
- [47] C. Chang and H. S. Fogler. Controlled Formation of Silica Particles from Tetraethyl Orthosilicate in Nonionic Water-in-Oil Microemulsions. *Langmuir*, 13(13):3295–3307, 1997.
- [48] R. P. Bagwe, C. Yang, L. R. Hilliard, and W. Tan. Optimization of dye-doped silica nanoparticles prepared using a reverse microemulsion method. *Langmuir*, 20(19):8336–8342, 2004.
- [49] F. Gao, L. Tang, L. Dai, and L. Wang. A fluorescence ratiometric nano-pH sensor based on dual-fluorophore-doped silica nanoparticles. *Spectrochimica Acta - Part A: Molecular and Biomolecular Spectroscopy*, 67(2):517–521, 2007.
- [50] K. S. Finnie, J. R. Bartlett, C. J. A. Barbé, and L. Kong. Formation of silica nanoparticles in microemulsions. *Langmuir*, 23(6):3017–3024, 2007.
- [51] R. Watanabe, T. Yokoi, E. Kobayashi, Y. Otsuka, A. Shimojima, T. Okubo, and T. Tatsumi. Extension of size of monodisperse silica nanospheres and their well-ordered assembly. *Journal of Colloid and Interface Science*, 360(1):1–7, 2011.
- [52] T. Yokoi, T. Karouji, S. Ohta, J. N. Kondo, and T. Tatsumi. Synthesis of mesoporous silica nanospheres promoted by basic amino acids and their catalytic application. *Chemistry of Materials*, 22(13):3900–3908, 2010.
- [53] S. Shahabi, L. Treccani, and K. Rezwan. Amino acid-catalyzed seed regrowth synthesis of photostable high fluorescent silica nanoparticles with tunable sizes for intracellular studies. *Journal of Nanoparticle Research*, 17(6):270, 2015.
- [54] J. Liu, S. Z. Qiao, J. S. Chen, X. W. (David) Lou, X. Xing, and G. Q. (Max) Lu. Yolk/shell nanoparticles: new platforms for nanoreactors, drug delivery and lithium-ion batteries. *Chemical Communications*, 47(47):12578, 2011.
- [55] R. Purbia and S. Paria. Yolk/shell nanoparticles: Classifications, synthesis, properties, and applications. *Nanoscale*, 7(47):19789–19873, 2015.

- [56] Y. Chen, H. R. Chen, and J. L. Shi. Construction of homogenous/heterogeneous hollow mesoporous silica nanostructures by silica-etching chemistry: Principles, synthesis, and applications. *Accounts of Chemical Research*, 47(1):125–137, 2014.
- [57] J. Lee, S. M. Kim, and I. S. Lee. Functionalization of hollow nanoparticles for nanoreactor applications. *Nano Today*, 9(5):631–667, 2014.
- [58] Q. Zhang, J. Ge, J. Goebel, Y. Hu, Z. Lu, and Y. Yin. Rattle-Type Silica Colloidal Particles Prepared by a Surface-Protected Etching Process. *Nano Research*, 2(7):583–591, 2009.
- [59] Y. Chen, H. Chen, L. Guo, Q. He, F. Chen, J. Zhou, J. Feng, and J. Shi. Hollow / Rattle-Type Mesoporous Nanostructures by a Structural Difference-Based Selective Etching Strategy. *ACS Nano*, 4(1):529–539, 2010.
- [60] Y. Chen, H. Chen, M. Ma, F. Chen, L. Guo, L. Zhang, and J. Shi. Double mesoporous silica shelled spherical/ellipsoidal nanostructures: Synthesis and hydrophilic/hydrophobic anticancer drug delivery. *Journal of Materials Chemistry*, 21(14):5290, 2011.
- [61] C. M. Fan, L. F. Zhang, S. S. Wang, D. H. Wang, L. Q. Lu, and A. W. Xu. Novel CeO₂ yolk-shell structures loaded with tiny Au nanoparticles for superior catalytic reduction of p-nitrophenol. *Nanoscale*, 4(21):6835–6840, 2012.
- [62] J. Lee, J. C. Park, and H. Song. A Nanoreactor framework of a Au@SiO₂ yolk/shell structure for catalytic reduction of p-nitrophenol. *Advanced Materials*, 20(8):1523–1528, 2008.
- [63] Z. W. Seh, W. Li, J. J. Cha, G. Zheng, Y. Yang, M. T. McDowell, P. C. Hsu, and Y. Cui. Sulphur-TiO₂ yolk-shell nanoarchitecture with internal void space for long-cycle lithium-sulphur batteries. *Nature Communications*, 4(13):1–6, 2013.
- [64] N. Liu, Z. Lu, J. Zhao, M. T. McDowell, H. W. Lee, W. Zhao, and Y. Cui. A pomegranate-inspired nanoscale design for large-volume-change lithium battery anodes. *Nature Nanotechnology*, 9(3):187–192, 2014.
- [65] L. Wang, H. Dou, Z. Lou, and T. Zhang. Encapsulated nanoreactors (Au@SnO₂): A new sensing material for chemical sensors. *Nanoscale*, 5(7):2686–2691, 2013.
- [66] P. Rai, J. W. Yoon, H. M. Jeong, S. J. Hwang, C. H. Kwak, and J. H. Lee. Design of highly sensitive and selective Au@NiO yolk-shell nanoreactors for gas sensor applications. *Nanoscale*, 6(14):8292–8299, 2014.
- [67] A. A. Volkert, M. C. S. Pierre, B. Shrestha, and A. J. Haes. Implications of sample aging on the formation of internally etched silica coated gold nanoparticles. *RSC Adv.*, 5:3774–3780, 2015.
- [68] X. Xie, M. A. van Huis, and A. van Blaaderen. Single-Step Coating of Mesoporous SiO₂ onto Nanoparticles: Growth of Yolk-Shell Structures from Core-Shell Structures. *Submitted*.
- [69] D. Nagao, C. M. van Kats, K. Hayasaka, M. Sugimoto, M. Konno, A. Imhof, and A. van Blaaderen. Synthesis of Hollow Asymmetrical Silica Dumbbells with a Movable Inner Core. *Langmuir*, 26(19):5208–5212, 2010.
- [70] B. Liu, W. Zhang, H. Feng, and X. Yang. Rattle-type microspheres as a support of tiny gold nanoparticles for highly efficient catalysis. *Chemical Communications*, 47(42):11727–11729, 2011.
- [71] F. Tang, L. Li, and D. Chen. Mesoporous silica nanoparticles: Synthesis, biocompatibility and drug delivery. *Advanced Materials*, 24(12):1504–1534, 2012.
- [72] I. I. Slowing, J. L. Vivero-Escoto, C. W. Wu, and V. S.Y. Lin. Mesoporous silica nanoparticles as controlled release drug delivery and gene transfection carriers. *Advanced Drug Delivery Reviews*, 60(11):1278–1288, 2008.
- [73] S. J. Tauster, S. C. Fung, R. T. K. Baker, and J. A. Horsley. Strong Interactions in Catalysts. *Science*, 211(4487):1121–1125, 1981.

- [74] D. Chen, L. Li, F. Tang, and S. Qi. Facile and Scalable Synthesis of Tailored Silica “Nanorattle” Structures. *Advanced Materials*, 21:3804–3807, 2009.
- [75] G. Li, E. T. Kang, K. G. Neoh, and X. Yang. Concentric hollow nanospheres of mesoporous silica shell-titania core from combined inorganic and polymer syntheses. *Langmuir*, 25(8):4361–4364, 2009.
- [76] X. Fang, C. Chen, Z. Liu, P. Liu, and N. Zheng. A cationic surfactant assisted selective etching strategy to hollow mesoporous silica spheres. *Nanoscale*, 3(4):1632–1639, 2011.
- [77] L. Scarabelli, M. Coronado-Puchau, J. J. Giner-Casares, J. Langer, and L. M. Liz-Marzán. Monodisperse gold nanotriangles: Size control, large-scale self-assembly, and performance in surface-enhanced raman scattering. *ACS Nano*, 8(6):5833–5842, 2014.
- [78] H. R. Vutukuri, F. Smallenburg, S. Badaire, A. Imhof, M. Dijkstra, and A. van Blaaderen. An experimental and simulation study on the self-assembly of colloidal cubes in external electric fields. *Soft Matter*, 10(45):9110–9119, 2014.
- [79] H. R. Vutukuri, S. Badaire, D. A. M. de Winter, A. Imhof, and A. van Blaaderen. Directed Self-Assembly of Micron-Sized Gold Nanoplatelets into Oriented Flexible Stacks with Tunable Interplate Distance. *Nano Letters*, 15(8):5617–5623, 2015.
- [80] A. M. Wierenga, T. A. J. Lenstra, and A. P. Philipse. Aqueous dispersions of colloidal gibbsite platelets: Synthesis, characterisation and intrinsic viscosity measurements. *Colloids and Surfaces A: Physicochemical and Engineering Aspects*, 134(3):359–371, 1998.
- [81] C. J. Desantis and S. E. Skrabalak. Size-controlled synthesis of Au/Pd octopods with high refractive index sensitivity. *Langmuir*, 28(24):9055–9062, 2012.
- [82] M. P. Arciniegas, M. R. Kim, J. de Graaf, R. Brescia, S. Marras, K. Miszta, M. Dijkstra, R. van Roij, and L. Manna. Self-assembly of octapod-shaped colloidal nanocrystals into a hexagonal ballerina network embedded in a thin polymer film. *Nano Letters*, 14(2):1056–1063, 2014.
- [83] A. Kuijk, A. van Blaaderen, and A. Imhof. Synthesis of monodisperse, rodlike silica colloids with tunable aspect ratio. *Journal of the American Chemical Society*, 133(8):2346–2349, 2011.
- [84] F. Hagemans, E. B. van der Wee, A. van Blaaderen, and A. Imhof. Synthesis of Cone-Shaped Colloids from Rod-Like Silica Colloids with a Gradient in the Etching Rate. *Langmuir*, 32(16):3970–3976, 2016.
- [85] F. Hagemans, R. K. Pujala, D. S. Hotie, D. M.E. Thies-Weesie, D. A.M. de Winter, J. D. Meeldijk, A. van Blaaderen, and A. Imhof. Shaping Silica Rods by Tuning Hydrolysis and Condensation of Silica Precursors. *Chemistry of Materials*, 31(2):521–531, 2019.
- [86] F. Hagemans, W. Vlug, C. Raffaelli, A. van Blaaderen, and A. Imhof. Sculpting Silica Colloids by Etching Particles with Nonuniform Compositions. *Chemistry of Materials*, 29(7):3304–3313, 2017.
- [87] Y. Hu, Q. Zhang, J. Goebel, T. Zhang, and Y. Yin. Control over the permeation of silica nanoshells by surface-protected etching with water. *Physical Chemistry Chemical Physics*, 12(38):11836–11842, 2010.
- [88] Y. J. Wong, L. Zhu, W. S. Teo, Y. W. Tan, Y. Yang, C. Wang, and H. Chen. Revisiting the Stöber method: Inhomogeneity in silica shells. *Journal of the American Chemical Society*, 133(30):11422–11425, 2011.
- [89] G. A.C.M. Spierings. Wet chemical etching of silicate glasses in hydrofluoric acid based solutions. *Journal of Materials Science*, 28(23):6261–6273, 1993.

- [90] D. J. Monk, D. S. Soane, and R. T. Howe. A review of the chemical reaction mechanism and kinetics for hydrofluoric acid etching of silicon dioxide for surface micromachining applications. *Thin Solid Films*, 232(1):1–12, 1993.
- [91] Q. Zhang, T. Zhang, J. Ge, and Y. Yin. Permeable Silica Shell through Surface-Protected Etching. *NANO Letters*, 8:2867–2871, 2008.
- [92] T. Zhang, J. Ge, Y. Hu, Q. Zhang, S. Aloni, and Y. Yin. Formation of hollow silica colloids through a spontaneous dissolution-regrowth process. *Angewandte Chemie - International Edition*, 47(31):5806–5811, 2008.
- [93] N. de Jonge, L. Houben, R. E. Dunin-Borkowski, and F. M. Ross. Resolution and aberration correction in liquid cell transmission electron microscopy. *Nature Reviews Materials*, 4:61–78, 2019.
- [94] N. de Jonge and F. M. Ross. Electron microscopy of specimens in liquid. *Nature nanotechnology*, 6:695–704, 2011.
- [95] F. M. Ross. Opportunities and challenges in liquid cell electron microscopy. *Science*, 350(6267), 2015.
- [96] S. W. Hell, K. I. Willig, M. Dyba, S. Jakobs, L. Kastrup, and V. Westphal. *Nanoscale Resolution with Focused Light: Stimulated Emission Depletion and Other Reversible Saturable Optical Fluorescence Transitions Microscopy Concepts*, pages 571–579. Springer US, Boston, MA, 2006.
- [97] S. Pujals, N. Feiner- Gracia, P. Delcanale, I. Voets, and L. Albertazzi. Super-resolution microscopy as a powerful tool to study complex synthetic materials. *Nature Reviews Chemistry*, 3:68–84, 2019.
- [98] L. Schermelleh, A. Ferrand, T. Huser, C. Eggeling, M. Sauer, O. Biehlmaier, and G. P. C. Drumen. Super-resolution microscopy demystified. *Nature Cell Biology*, 21(January):72–84, 2019.
- [99] G. Vicidomini, P. Bianchini, and A. Diaspro. STED super-resolved microscopy. *Nature Methods*, 15(3):173–182, 2018.
- [100] H. Blom and J. Widengren. Stimulated Emission Depletion Microscopy. *Chemical Reviews*, 117:7377–7427, 2017.
- [101] S. J. Sahl, S. W. Hell, and S. Jakobs. Fluorescence nanoscopy in cell biology. *Nature Reviews Molecular Cell Biology*, 18(11):685–701, 2017.
- [102] Y. M. Sigal, R. Zhou, and X. Zhuang. Visualizing and discovering cellular structures with super-resolution microscopy. *Science*, 361(August):880–887, 2018.
- [103] R. Horodecki. De broglie wave and its dual wave. *Physics Letters*, 87(3):95–97, 1981.
- [104] R. Ru, H. G. Rudenberg, P. G. Rudenberg, and R. Ru. *Chapter 6 - Origin and Background of the Invention of the Electron Microscope: Commentary and Expanded Notes on Memoir of Reinhold Rüdenberg*, volume 160. Elsevier Inc., 1 edition, 2010.
- [105] D. B. Williams and C. B. Carter. *Transmission Electron Microscopy, A Textbook for Materials Science*. Springer, New York, 2008.
- [106] P. E. Batson, N. Dellby, and O. L. Krivanek. Sub-angstrom resolution using aberration corrected electron optics. *Nature*, 418:617–619, 2002.
- [107] R. F. Egerton. Choice of operating voltage for a transmission electron microscope. *Ultramicroscopy*, 145:85–93, 2014.
- [108] D. Contarato, P. Denes, D. Doering, J. Joseph, and B. Krieger. High Speed, Radiation Hard CMOS Pixel Sensors for Transmission Electron Microscopy. *Physics Procedia*, 37:1504–1510, 2012.

- [109] G. McMullan, A. R. Faruqi, D. Clare, and R. Henderson. Comparison of optimal performance at 300 keV of three direct electron detectors for use in low dose electron microscopy. *Ultramicroscopy*, 147:156–163, 2014.
- [110] N. de Jonge, N. Poirier-Demers, H. Demers, D. B. Peckys, and D. Drouin. Nanometer-resolution electron microscopy through micrometers-thick water layers. *Ultramicroscopy*, 110(9):1114–1119, 2010.
- [111] J. M. Yuk, J. Park, P. Ercius, K. Kim, D. J. Hellebusch, M. F. Crommie, J. Y. Lee, A. Zettl, and A. P. Alivisatos. High-Resolution EM of Colloidal Nanocrystal Growth Using Graphene Liquid Cells. *Science*, 336(April):61–65, 2012.
- [112] M. R. Hauwiller, J. C. Ondry, C. M. Chan, P. Khandekar, and J. Yu. Gold Nanocrystal Etching as a Means of Probing the Dynamic Chemical Environment in Graphene Liquid Cell Electron Microscopy. *JACS*, 141:4428–4437, 2019.
- [113] M. R. Hauwiller, L. B. Frechette, M. R. Jones, J. C. Ondry, G. M. Rotsko, P. Geissler, and A. P. Alivisatos. Unraveling Kinetically-Driven Mechanisms of Gold Nanocrystal Shape Transformations Using Graphene Liquid Cell Electron Microscopy. *Nano Letters*, 18:5731–5737, 2018.
- [114] J. Park, H. Park, P. Ercius, A. F. Pegoraro, C. Xu, J. W. Kim, S. H. Han, and D. A. Weitz. Direct Observation of Wet Biological Samples by Graphene Liquid Cell Transmission Electron Microscopy. *Nano Letters*, 15(7):4737–4744, 2015.
- [115] L. Zhang, M. D. Acunzi, M. Kappl, A. Imhof, D. Vollmer, and A. van Blaaderen. Tuning the mechanical properties of silica microcapsules. *Physical Chemistry Chemical Physics*, 12:15392–15398, 2010.
- [116] S. Romeis, J. Paul, M. Hanisch, V. R. R. Marthala, M. Hartmann, R. N. K. Taylor, J. Schmidt, and W. Peukert. Correlation of enhanced strength and internal structure for heat-treated submicron Stöber silica particles. *Particle and Particle Systems Characterization*, 31(6):664–674, 2014.
- [117] A. A. Chabanov, Y. Jun, D. J. Norris, A. A. Chabanov, Y. Jun, and D. J. Norris. Avoiding cracks in self-assembled photonic band-gap crystals. *Applied Physics Letters*, 84(18):3573–3575, 2004.
- [118] H. Míguez, F. Meseguer, C. López, A. Blanco, J. S. Moya, and J. Requena. Control of the Photonic Crystal Properties of fcc-Packed Submicrometer SiO₂ Spheres by Sintering. *Advanced Materials*, 10(6):480–483, 1998.
- [119] F. García-Santamaría, H. Míguez, M. Ibáñez, F. Meseguer, and C. López. Refractive Index Properties of Calcined Silica Submicrometer Spheres. *Langmuir*, 18(11):1942–1944, 2002.
- [120] K. Watanabe, H. Ishii, M. Konno, A. Imhof, A. van Blaaderen, and D. Nagao. Yolk/Shell Colloidal Crystals Incorporating Movable Cores with Their Motion Controlled by an External Electric Field. *Langmuir*, 33:296–302, 2017.
- [121] J. Turkevich, P. C. Stevenson, and J. Hillier. A study of the nucleation and growth processes in the synthesis of colloidal gold. *Discussions of the Faraday Society*, 11(c):55–75, 1951.
- [122] C. Graf, D. L. J. Vossen, A. Imhof, and A. van Blaaderen. A General Method To Coat Colloidal Particles with Silica. *Langmuir*, 19:6693–6700, 2003.
- [123] A. Verch, M. Pfaff, and N. de Jonge. Exceptionally Slow Movement of Gold Nanoparticles at a Solid/Liquid Interface Investigated by Scanning Transmission Electron Microscopy. *Langmuir*, 31(25):6956–6964, 2015.

- [124] R. F. Egerton, P. Li, and M. Malac. Radiation damage in the TEM and SEM. *Micron*, 35(6):399–409, 2004.
- [125] N. M. Schneider, M. M. Norton, B. J. Mendel, J. M. Grogan, F. M. Ross, and H. H. Bau. Electron-Water Interactions and Implications for Liquid Cell Electron Microscopy. *J. Phys. Chem. C*, 118:22373–22382, 2014.
- [126] M. Maćković, F. Niekiel, L. Wondraczek, and E. Speecker. Direct observation of electron-beam-induced densification and hardening of silica nanoballs by in situ transmission electron microscopy and finite element method simulations. *Acta Materialia*, 79:363–373, 2014.
- [127] M. W. P. van de Put, C. C M. C. Carcouët, P. H. H. Bomans, H. Friedrich, N. de Jonge, and N. A. J. M. Sommerdijk. Writing silica structures in liquid with scanning transmission electron microscopy. *Small*, 11(5):585–590, 2015.
- [128] K. Zheng, C. Wang, Y. Cheng, Y. Yue, X. Han, Z. Zhang, Z. Shan, S. X. Mao, M. Ye, Y. Yin, and E. Ma. Electron-beam-assisted superplastic shaping of nanoscale amorphous silica. *Nature communications*, 1(3):24, 2010.
- [129] J. Zečević, J. Hermannsdorfer, T. Schuh, K. P. de Jong, and N. de Jonge. Anisotropic Shape Changes of Silica Nanoparticles Induced in Liquid with Scanning Transmission Electron Microscopy. *Small*, 13:1602466, 2017.
- [130] W. Vlug. *Balls, beams and blocks: In situ observation of colloidal particles in confinement and under electron irradiation*. Phd thesis, Utrecht University, 2018.
- [131] N. Jiang. Note on in situ (scanning) transmission electron microscopy study of liquid samples. *Ultramicroscopy*, 179:81–83, 2017.
- [132] D. Sarker, S. Bhattacharya, H. Kumar, P. Srivastava, and S. Ghosh. Evidence of local structural influence on the shape driven magnetic anisotropy in electronically excited Ni nanoparticles embedded in SiO₂ matrix. *Scientific Reports*, 8(1):1–10, 2018.
- [133] R. E. Baumer and M. J. Demkowicz. A “figure of merit” for susceptibility of irradiated amorphous metal alloys to thermal spike-induced plasticity. *Acta Materialia*, 102:251–262, 2016.
- [134] F. Li, D. P. Josephson, and A. Stein. Colloidal assembly: The road from particles to colloidal molecules and crystals. *Angewandte Chemie - International Edition*, 50(2):360–388, 2011.
- [135] A. van Blaaderen. Colloids get complex. *Nature*, 439:545–546, 2006.
- [136] S. Sacanna, D. J. Pine, and G. R. Yi. Engineering shape: The novel geometries of colloidal self-assembly. *Soft Matter*, 9(34):8096–8106, 2013.
- [137] R. G. Chaudhuri and S. Paria. Core/Shell Nanoparticles : Classes, Properties, Synthesis Mechanisms, Characterization, and Applications. *Chemical Reviews*, 112:2373–2433, 2012.
- [138] R. Narayan and U. Y. Nayak. Mesoporous Silica Nanoparticles : A Comprehensive Review on Synthesis and Recent Advances. *Pharmaceutics*, 10(18):1–49, 2018.
- [139] G. Nägele. On the dynamics and structure of charge-stabilized suspensions. *Physics Report*, 272(5-6):215–372, 1996.
- [140] M. C. Jenkins and S. U. Egelhaaf. Confocal microscopy of colloidal particles: Towards reliable, optimum coordinates. *Advances in Colloid and Interface Science*, 136:65–92, 2008.
- [141] B. D. Leahy, N. Y. C. Lin, and I. Cohen. Quantitative light microscopy of dense suspensions: Colloid science at the next decimal place. *Current Opinion in Colloid and Interface Science*, 34:32–46, 2018.
- [142] M. A. Bevan and S. L. Eichmann. Optical microscopy measurements of kT-scale colloidal interactions. *Current Opinion in Colloid and Interface Science*, 16(2):149–157, 2011.

- [143] J. C. Crocker. Measurement of the hydrodynamic corrections to the Brownian motion of two colloidal spheres. *The Journal of Chemical Physics*, 106(7):2837–2840, 1997.
- [144] W. Sutherland. A dynamical theory of diffusion for non-electrolytes and the molecular mass of albumin. *The London, Edinburgh, and Dublin Philosophical Magazine and Journal of Science*, 9(54):781–785, 1905.
- [145] M. D. Carbajal-Tinoco, R. Lopez-Fernandez, and J. L. Arauz-Lara. Asymmetry in colloidal diffusion near a rigid wall. *Physical Review Letters*, 99(13):1–4, 2007.
- [146] D. C. Prieve. Measurement of colloidal forces with TIRM. *Advances in Colloid and Interface Science*, 82(1):93–125, 1999.
- [147] P. Holmqvist, J. K. G. Dhont, and P. R. Lang. Anisotropy of Brownian motion caused only by hydrodynamic interaction with a wall. *Physical Review E - Statistical, Nonlinear, and Soft Matter Physics*, 74(2):1–5, 2006.
- [148] H. Brenner. The slow motion of a sphere through a viscous fluid towards a plane surface. *Chemical Engineering Science*, 16(3-4):242–251, 1961.
- [149] A. J. Goldman, R. G. Cox, and H. Brenner. Slow viscous motion of a sphere parallel to a plane wall-I Motion through a quiescent fluid. *Chemical Engineering Science*, 22(4):637–651, 1967.
- [150] B. Cichocki and R.B. Jones. Image representation of a spherical particle near a hard wall. *Physica A: Statistical Mechanics and its Applications*, 258(3-4):273–302, 1998.
- [151] L. Lobry and N. Ostrowsky. Diffusion of Brownian particles trapped between two walls: Theory and dynamic-light-scattering measurements. *Physical Review B*, 53(18):12050–12056, 1996.
- [152] E. R. Dufresne, D. Altman, and D. G. Grier. Brownian dynamics of a sphere between parallel walls. *Europhysics Letters*, 53(2):264–270, 2001.
- [153] S. L. Eichmann, S. G. Anekal, and M. A. Bevan. Electrostatically confined nanoparticle interactions and dynamics. *Langmuir*, 24(3):714–721, 2008.
- [154] M. A. Bevan and D. C. Prieve. Hindered diffusion of colloidal particles very near to a wall: revisited. *Journal of Chemical Physics*, 113(3):1228–1236, 2000.
- [155] H. B. Eral, J. M. Oh, D. van den Ende, F. Mugele, and M. H. G. Duits. Anisotropic and hindered diffusion of colloidal particles in a closed cylinder. *Langmuir*, 26(22):16722–16729, 2010.
- [156] A. Imperio, J. T. Padding, and W. J. Briels. Diffusion of spherical particles in microcavities. *Journal of Chemical Physics*, 134(15):1–9, 2011.
- [157] A. E. Cervantes-Martínez, A. Ramírez-Saito, R. Armenta-Calderón, M. A. Ojeda-López, and J. L. Arauz-Lara. Colloidal diffusion inside a spherical cell. *Physical Review E - Statistical, Nonlinear, and Soft Matter Physics*, 83(3):1–4, 2011.
- [158] C. Aponte-Rivera and R. N. Zia. Simulations of hydrodynamically interacting particles confined by a spherical cavity. *Physical Review Fluids*, 1(2):1–61, 2016.
- [159] K. Kamata, Y. Lu, and Y. Xia. Synthesis and characterization of monodispersed core-shell spherical colloids with movable cores. *Journal of the American Chemical Society*, 125(9):2384–2385, 2003.
- [160] Q. Chen, J. M. Smith, J. Park, K. Kim, D. Ho, H. I. Rasool, A. Zettl, and A. P. Alivisatos. 3D motion of DNA-Au nanoconjugates in graphene liquid cell electron microscopy. *Nano Letters*, 13(9):4556–4561, 2013.
- [161] R. K. Iler. *The Chemistry of silica, Solubility, Polymerization, Colloid and Surface Properties, and Biochemistry*. John Wiley & Sons, Ltd, New York, Chichester, Brisbane, Toronto, Singapore, 1979.

- [162] J. Liu, Z. Wang, A. Sheng, F. Liu, F. Qin, and Z. L. Wang. In Situ Observation of Hematite Nanoparticle Aggregates Using Liquid Cell Transmission Electron Microscopy. *Environmental Science and Technology*, 50(11):5606–5613, 2016.
- [163] S. W. Chee, Z. Baraissov, N. D. Loh, P. T. Matsudaira, and U. Mirsaidov. Desorption-mediated motion of nanoparticles at the liquid-solid interface. *Journal of Physical Chemistry C*, 120(36):20462–20470, 2016.
- [164] M. T. Proetto, A. M. Rush, M. P. Chien, P. Abellan Baeza, J. P. Patterson, M. P. Thompson, N. H. Olson, C. E. Moore, A. L. Rheingold, C. Andolina, J. Millstone, S. B. Howell, N. D. Browning, J. E. Evans, and N. C. Gianneschi. Dynamics of soft nanomaterials captured by transmission electron microscopy in liquid water. *Journal of the American Chemical Society*, 136(4):1162–1165, 2014.
- [165] E. A. Ring and N. de Jonge. Video-frequency scanning transmission electron microscopy of moving gold nanoparticles in liquid. *Micron*, 43(11):1078–1084, 2012.
- [166] J. Lu, Z. Aabdin, N. D. Loh, D. Bhattacharya, and U. Mirsaidov. Nanoparticle dynamics in a nanodroplet. *Nano Letters*, 14(4):2111–2115, 2014.
- [167] Y. Liu, X. M. Lin, Y. Sun, and T. Rajh. In situ visualization of self-assembly of charged gold nanoparticles. *Journal of the American Chemical Society*, 135(10):3764–3767, 2013.
- [168] A. S. Powers, H. G. Liao, S. N. Raja, N. D. Bronstein, A. P. Alivisatos, and H. Zheng. Tracking Nanoparticle diffusion and interaction during self-assembly in a liquid cell. *Nano Letters*, 17(1):15–20, 2017.
- [169] E. R. White, M. Mecklenburg, B. Shevitski, S. B. Singer, and B. C. Regan. Charged nanoparticle dynamics in water induced by scanning transmission electron microscopy. *Langmuir*, 28(8):3695–3698, 2012.
- [170] L. R. Parent, E. Bakalis, A. Ramírez-Hernández, J. K. Kammeyer, C. Park, J. De Pablo, F. Zerbetto, J. P. Patterson, and N. C. Gianneschi. Directly Observing Micelle Fusion and Growth in Solution by Liquid-Cell Transmission Electron Microscopy. *Journal of the American Chemical Society*, 139(47):17140–17151, 2017.
- [171] T. J. Woehl and T. Prozorov. The Mechanisms for Nanoparticle Surface Diffusion and Chain Self-Assembly Determined from Real-Time Nanoscale Kinetics in Liquid. *Journal of Physical Chemistry C*, 119(36):21261–21269, 2015.
- [172] G. Lin, S. W. Chee, S. Raj, P. Král, and U. Mirsaidov. Linker-Mediated Self-Assembly Dynamics of Charged Nanoparticles. *ACS Nano*, 10(8):7443–7450, 2016.
- [173] G. Lin, X. Zhu, U. Anand, Q. Liu, J. Lu, Z. Aabdin, H. Su, and U. Mirsaidov. Nanodroplet-Mediated Assembly of Platinum Nanoparticle Rings in Solution. *Nano Letters*, 16(2):1092–1096, 2016.
- [174] H. Zheng, S. A. Claridge, A. M. Minor, A. P. Alivisatos, and U. Dahmen. Nanocrystal diffusion in a liquid thin film observed by in situ transmission electron microscopy. *Nano Letters*, 9(6):2460–2465, 2009.
- [175] T. J. Woehl, K. L. Jungjohann, J. E. Evans, I. Arslan, W. D. Ristenpart, and N. D. Browning. Experimental procedures to mitigate electron beam induced artifacts during in situ fluid imaging of nanomaterials. *Ultramicroscopy*, 127:53–63, 2013.
- [176] S. F. Tan, U. Anand, and U. Mirsaidov. Interactions and Attachment Pathways between Functionalized Gold Nanorods. *ACS Nano*, 11(2):1633–1640, 2017.
- [177] X. Tian, H. Zheng, and U. Mirsaidov. Aggregation dynamics of nanoparticles at solid-liquid interfaces. *Nanoscale*, 9(28):10044–10050, 2017.

- [178] G. Zhu, Y. Jiang, W. Huang, H. Zhang, F. Lin, and C. Jin. Atomic resolution liquid-cell transmission electron microscopy investigations of the dynamics of nanoparticles in ultrathin liquids. *Chemical Communications*, 49(93):10944–10946, 2013.
- [179] S. F. Tan, S. W. Chee, G. Lin, and U. Mirsaidov. Direct Observation of Interactions between Nanoparticles and Nanoparticle Self-Assembly in Solution. *Accounts of Chemical Research*, 50(6):1303–1312, 2017.
- [180] E. Sutter. In situ microscopy of the self-assembly of branched nanocrystals in solution-SI. *Nature Communications*, 7:11213, 2016.
- [181] M. Piffoux, N. Ahmad, J. Nelayah, C. Wilhelm, A. Silva, F. Gazeau, and D. Alloyeau. Monitoring the dynamics of cell-derived extracellular vesicles at the nanoscale by liquid-cell transmission electron microscopy. *Nanoscale*, 10:1234–1244, 2018.
- [182] D. J. Kelly, M. Zhou, N. Clark, M. J. Hamer, E. A. Lewis, A. M. Rakowski, S. J. Haigh, and R. V. Gorbachev. Nanometer Resolution Elemental Mapping in Graphene-Based TEM Liquid Cells. *Nano Letters*, 18(2):1168–1174, 2018.
- [183] J. Kim, Z. Ou, M. R. Jones, X. Song, and Q. Chen. Imaging the polymerization of multivalent nanoparticles in solution. *Nature Communications*, 8(761):1–10, 2017.
- [184] M. A. Boles, M. Engel, and D. V. Talapin. Self-assembly of colloidal nanocrystals: From intricate structures to functional materials. *Chemical Reviews*, 116(18):11220–11289, 2016.
- [185] J. Crocker and D. Grier. Methods of Digital Video Microscopy for Colloidal Studies. *Journal of Colloid and Interface Science*, 179(1):298–310, 1996.
- [186] T. Palberg. Crystallization kinetics of colloidal model suspensions: recent achievements and new perspectives. *Journal of Physics: Condensed Matter*, 26(33):333101, jul 2014.
- [187] T. Palberg. Crystallization kinetics of repulsive colloidal spheres. *Journal of Physics: Condensed Matter*, 11(28):R323–R360, jan 1999.
- [188] V. Lobaskin, B. Dünweg, M. Medebach, T. Palberg, and C. Holm. Electrophoresis of Colloidal Dispersions in the Low-Salt Regime. *Physical Review Letters*, 98:176105 (1–4), 2007.
- [189] H. E. Bergna. *The Colloid Chemistry of Silica*. American Chemical Society, Washington D.C., 1994.
- [190] P. Nakroshis, M. Amoroso, J. Legere, and C. Smith. Measuring Boltzmann’s constant using video microscopy of Brownian motion. *American Journal of Physics*, 71(6):568–573, 2003.
- [191] X. Gao, J. He, L. Deng, and H. Cao. Synthesis and characterization of functionalized rhodamine B-doped silica nanoparticles. *Optical Materials*, 31(11):1715–1719, 2009.
- [192] O. G. Tovmachenko, C. Graf, D. J. van den Heuvel, A. van Blaaderen, and H. C. Gerritsen. Fluorescence enhancement by metal-core/silica-shell nanoparticles. *Advanced Materials*, 18(1):91–95, 2006.
- [193] T. S. Horozov, R. Aveyard, B. P. Binks, and J. H. Clint. Structure and stability of silica particle monolayers at horizontal and vertical octane-water interfaces. *Langmuir*, 21(16):7405–7412, 2005.
- [194] M. Nakamura, M. Shono, and K. Ishimura. Synthesis, characterization, and biological applications of multifluorescent silica nanoparticles. *Analytical Chemistry*, 79(17):6507–6514, 2007.
- [195] H. Giesche. Synthesis of monodispersed silica powders I. Particle properties and reaction kinetics. *Journal of the European Ceramic Society*, 14(3):189–204, 1994.
- [196] R. Koole, M. M. van Schooneveld, J. Hilhorst, C. M. de Donegal, D. C. ’t Hart, A. van Blaaderen, D. Vanmaekelbergh, and A. Meijerink. On the incorporation mechanism of hydrophobic quantum

- dots in silica spheres by a reverse microemulsion method. *Chemistry of Materials*, 20(7):2503–2512, 2008.
- [197] S. Shahabi, L. Treccani, and K. Rezwan. A comparative study of three different synthesis routes for hydrophilic fluorophore-doped silica nanoparticles. *Journal of Nanoparticle Research*, 18(1):1–13, 2016.
- [198] Y. J. Wong, L. Zhu, W. S. Teo, Y. W. Tan, Y. Yang, C. Wang, and H. Chen. Revisiting the Stöber method: Inhomogeneity in silica shells. *Journal of the American Chemical Society*, 133(30):11422–11425, 2011.
- [199] K. D. Hartlen, A. P. T. Athanasopoulos, and V. Kitaev. Facile Preparation of Highly Monodisperse Small Silica Spheres (15 to > 200 nm) Suitable for Colloidal Templating and Formation of Ordered Arrays. *Langmuir*, 24(16):1714–1720, 2008.
- [200] S. Fouilloux, O. Tach, O. Spalla, and A. Thill. Nucleation of Silica Nanoparticles Measured in Situ during Controlled Supersaturation Increase . Restructuring toward a Monodisperse Nonspherical Shape. *Langmuir*, 27:12304–12311, 2011.
- [201] C. C. M. C. Carcouët, M. W. P. van de Put, B. Mezari, P. C. M. M. Magusin, J. Laven, P. H. H. Bomans, H. Friedrich, A. C. C. Esteves, N. A. J. M. Sommerdijk, R. A. T. M. van Benthem, and W. de Gijsbertus. Nucleation and Growth of Monodisperse Silica Nanoparticles. *Nano Letters*, 14:1433–1438, 2014.
- [202] P. A. Bazuła, P. M. Arnal, C. Galeano, B. Zibrowius, W. Schmidt, and F. Schüth. Highly microporous monodisperse silica spheres synthesized by the stöber process. *Microporous and Mesoporous Materials*, 200:317 – 325, 2014.
- [203] C. H. Lin, J. H. Chang, Y. Q. Yeh, S. H. Wu, Y. H. Liu, and C. Y. Mou. Formation of hollow silica nanospheres by reverse microemulsion. *Nanoscale*, 7(21):9614–9626, 2015.
- [204] S. Sjöberg. Silica in aqueous environments. *Journal of Non-Crystalline Solids*, 196:51–57, 1996.
- [205] J. Farrando-Pérez, C. López, J. Silvestre-Albero, and F. Gallego-Gómez. Direct Measurement of Microporosity and Molecular Accessibility in Stöber Spheres by Adsorption Isotherms. *Journal of Physical Chemistry C*, 122(38):22008–22017, 2018.
- [206] Z. Aabdin, X. M. Xu, S. Sen, U. Anand, P. Král, F. Holsteyns, and U. Mirsaidov. Transient Clustering of Reaction Intermediates during Wet Etching of Silicon Nanostructures. *Nano Letters*, 17(5):2953–2958, 2017.
- [207] Y. Jiang, G. Zhu, F. Lin, H. Zhang, C. Jin, J. Yuan, D. Yang, and Z. Zhang. In situ study of oxidative etching of palladium nanocrystals by liquid cell electron microscopy. *Nano Letters*, 14(7):3761–3765, 2014.
- [208] Y. Jiang, G. Zhu, G. Dong, F. Lin, H. Zhang, J. Yuan, Z. Zhang, and C. Jin. Probing the oxidative etching induced dissolution of palladium nanocrystals in solution by liquid cell transmission electron microscopy. *Micron*, 97:22–28, 2017.
- [209] M. J. Meijerink, C. Spiga, T. W. Hansen, C. D. Damsgaard, K. P. de Jong, and J. Zečević. Nanoscale Imaging and Stabilization of Silica Nanospheres in Liquid Phase Transmission Electron Microscopy. *Particle and Particle Systems Characterization*, 36(1):1–8, 2019.
- [210] T. J. Woehl and P. Abellán. Defining the radiation chemistry during liquid cell electron microscopy to enable visualization of nanomaterial growth and degradation dynamics. *Journal of Microscopy*, 265(2):135–147, 2017.
- [211] H. Liao, L. Cui, S. Whitelam, and H. Zheng. Real-Time Imaging of Pt₃Fe Nanorod Growth in Solution. *Science*, 336(May):1011–1015, 2012.

- [212] T. H. Moser, H. Mehta, C. Park, R. T. Kelly, T. Shokuhfar, and J. E. Evans. The role of electron irradiation history in liquid cell transmission electron microscopy. *Science Advances*, 4(4):eaaq1202, 2018.
- [213] M. Wang, C. Park, and T. J. Woehl. Quantifying the Nucleation and Growth Kinetics of Electron Beam Nanochemistry with Liquid Cell Scanning Transmission Electron Microscopy. *Chemistry of Materials*, 30(21):7727–7736, 2018.
- [214] K. L. Jungjohann, S. Bliznakov, P. W. Sutter, E. A. Stach, and E. A. Sutter. In Situ Liquid Cell Electron Microscopy of the Solution Growth of Au-Pd Core-Shell Nanostructures. *Nano Letters*, 13:2964–2970, 2013.
- [215] D. Keller, T. R. Henninen, and R. Erni. Formation of gold nanoparticles in a free-standing ionic liquid triggered by heat and electron irradiation. *Micron*, 117(October 2018):16–21, 2019.
- [216] D. Alloyeau, W. Dachraoui, Y. Javed, H. Belkahla, G. Wang, H. Lecoq, S. Ammar, O. Ersen, A. Wisnet, F. Gazeau, and C. Ricolleau. Unravelling Kinetic and Thermodynamic Effects on the Growth of Gold Nanoplates by Liquid Transmission Electron Microscopy. *Nano Letters*, 15(4):2574–2581, 2015.
- [217] P. Abellan, T. H. Moser, I. T. Lucas, J. W. Grate, J. E. Evans, and N. D. Browning. The formation of cerium(III) hydroxide nanoparticles by a radiation mediated increase in local pH. *RSC Adv.*, 7(7):3831–3837, 2017.
- [218] P. Abellan, T. J. Woehl, L. R. Parent, N. D. Browning, J. E. Evans, and I. Arslan. Factors influencing quantitative liquid (scanning) transmission electron microscopy. *Chemical Communications*, 50(38):4873–4880, 2014.
- [219] Y. Han, J. Jiang, S. S. Lee, and J. Y. Ying. Reverse Microemulsion-Mediated Synthesis of Silica-Coated Gold and Silver Nanoparticles. *Langmuir*, 24:5842–5848, 2008.
- [220] J. E. Park, E. D. Grayfer, Y. Jung, K. Kim, K. K. Wang, Y. R. Kim, D. Yoon, H. Cheong, H. E. Chung, S. J. Choi, J. H. Choy, and S. J. Kim. Photoluminescent nanographitic/nitrogen-doped graphitic hollow shells as a potential candidate for biological applications. *Journal of Materials Chemistry B*, 1(9):1229–1234, 2013.
- [221] J. Park, K. An, Y. Hwang, J. E. G. Park, H. J. Noh, J. Y. Kim, J. H. Park, N. M. Hwang, and T. Hyeon. Ultra-large-scale syntheses of monodisperse nanocrystals. *Nature Materials*, 3(12):891–895, 2004.
- [222] L. Rossi, S. Sacanna, W. T. M. Irvine, P. M. Chaikin, D. J. Pine, and A. P. Philipse. Cubic crystals from cubic colloids. *Soft Matter*, 7:4139–4142, 2011.
- [223] H. Demers, N. Poirier-Demers, A. R. Couture, D. Joly, M. Guilmain, N. de Jonge, and D. Drouin. Three-dimensional electron microscopy simulation with the CASINO Monte Carlo software. *The Journal of Scanning Microscopies*, 33(3):135–146, 2011.
- [224] H. Demers, N. Poirier-Demers, D. Drouin, and N. de Jonge. Simulating STEM imaging of nanoparticles in micrometers-thick substrates. *Microscopy and Microanalysis*, 16:795–804, 2010.
- [225] A. F. Holleman, E. Wiberg, N. Wiberg, William Brewer, and M. L. Eagleson. *Textbook of Inorganic Chemistry*. Academic Press, 2001.
- [226] G. McMullan, A. R. Faruqi, and R. Henderson. *Direct Electron Detectors*, volume 579. Elsevier Inc., 1 edition, 2016.
- [227] Y. Fujiyoshi. *Low Dose Techniques and Cryo-Electron Microscopy*, pages 103–118. Humana Press, Totowa, NJ, 2013.
- [228] N. Jiang. Electron beam damage in oxides: A review. *Reports on Progress in Physics*, 79(1):1–33, 2016.

- [229] M. N. Kabler Williams and R. T. Vacancy-interstitial pair production via electron-hole recombination in halide crystals. *Physical Review B*, 18(4):1948–1960, 1978.
- [230] L. W. Hobbs. Electron-beam sensitivity in inorganic specimens. *Ultramicroscopy*, 23(3-4):339–344, 1987.
- [231] R. F. Egerton. Mechanisms of radiation damage in beam-sensitive specimens, for TEM accelerating voltages between 10 and 300 kV. *Microscopy Research and Technique*, 75(11):1550–1556, 2012.
- [232] H. Inui, H. Mori, T. Sakata, and H. Fujita. Electron irradiation induced crystalline-to-amorphous transition in quartz single crystals. *Journal of Non-Crystalline Solids*, 116(1):1–15, 1990.
- [233] R. F. Egerton. Radiation damage to organic and inorganic specimens in the TEM. *Micron*, 119(January):72–87, 2019.
- [234] R. K. Eby, R. C. Ewing, and R. C. Birtcher. The amorphization of complex silicates by ion-beam irradiation. *Journal of Materials Research*, 7(11):3080–3102, 1992.
- [235] D. L. J. Vossen, D. Fific, J. Penninkhof, T. van Dillen, A. Polman, and A. van Blaaderen. Combined optical tweezers/ion beam technique to tune colloidal masks for nanolithography. *Nano Letters*, 5(6):1175–1179, 2005.
- [236] S. K. Estreicher, D. J. Backlund, C. Carbogno, and M. Scheffler. Activation energies for diffusion of defects in silicon: The role of the exchange-correlation functional. *Angewandte Chemie - International Edition*, 50(43):10221–10225, 2011.
- [237] K. K. Neelisetty, X. Mu, S. Gutsch, A. Vahl, A. Molinari, F. von Seggern, M. Hansen, T. Scherer, M. Zacharias, L. Kienle, V. S. K. Chakravadhanula, and C. Kübel. Electron Beam Effects on Oxide Thin Films-Structure and Electrical Property Correlations. *Microscopy and Microanalysis*, 25(3):592–600, 2019.
- [238] X. Wang, J. Feng, Q. Zhang, Y. Yin, and Y. Bai. Synthesis, Properties, and Applications of Hollow Micro-/Nanostructures. *Chemical Reviews*, 116(18):10983–11060, 2016.
- [239] J. C. Park and H. Song. Metal@Silica yolk-shell nanostructures as versatile bifunctional nanocatalysts. *Nano Research*, 4(1):33–49, 2011.
- [240] C. H. Lin, X. Liu, S. H. Wu, K. H. Liu, and C. Y. Mou. Corking and uncorking a catalytic yolk-shell nanoreactor: Stable gold catalyst in hollow silica nanosphere. *Journal of Physical Chemistry Letters*, 2(23):2984–2988, 2011.
- [241] M. Roca and A. J. Haes. Silica - Void - Gold Nanoparticles : Temporally Stable Surface-Enhanced Raman Scattering Substrates. *JACS*, 130:14273–14279, 2008.
- [242] Y. Yao, X. Zhang, J. Peng, and Q. Yang. One-pot fabrication of yolk–shell nanospheres with ultra-small au nanoparticles for catalysis. *Chem. Commun.*, 51:3750–3753, 2015.
- [243] H. Ding, Y. Zhang, S. Xu, and G. Li. A wrinkle to sub-100 nm yolk/shell $\text{Fe}_3\text{O}_4@\text{SiO}_2$ nanoparticles. *Nano Research*, 9(12):3632–3643, 2016.
- [244] S. C. Glotzer and M. J. Solomon. Anisotropy of building blocks and their assembly into complex structures. *Nature Materials*, 6(8):557–562, 2007.
- [245] S. M. Yang, S. H. Kim, J. M. Lim, and G. R. Yi. Synthesis and assembly of structured colloidal particles. *Journal of Materials Chemistry*, 18(19):2177–2190, 2008.
- [246] A. Perro, S. Reculusa, S. Ravaine, E. Bourgeat-Lami, and E. Duguet. Design and synthesis of Janus micro- and nanoparticles. *Journal of Materials Chemistry*, 15(35-36):3745–3760, 2005.
- [247] G. J. Vroege and H. N. W. Lekkerkerker. Phase transitions in lyotropic colloidal and polymer liquid crystals. *Reports on Progress in Physics*, 55(8):1241–1309, aug 1992.

- [248] M. Bär, R. Großmann, S. Heidenreich, and F. Peruani. Self-propelled rods: Insights and perspectives for active matter. *Annual Review of Condensed Matter Physics*, 11(1):441–466, 2020.
- [249] C. J. Murphy, A. M. Gole, S. E. Hunyadi, J. W. Stone, P. N. Sisco, A. Alkilany, B. E. Kinard, and P. Hankins. Chemical sensing and imaging with metallic nanorods. *Chem. Commun.*, pages 544–557, 2008.
- [250] S. Y. Zhang, M. D. Regulacio, and M. Y. Han. Self-assembly of colloidal one-dimensional nanocrystals. *Chem. Soc. Rev.*, 43:2301–2323, 2014.
- [251] K. Thorkelsson, P. Bai, and T. Xu. Self-assembly and applications of anisotropic nanomaterials: A review. *Nano Today*, 10(1), 2 2015.
- [252] A. S. Sonin, N. A. Churochkina, A. V. Kaznacheev, and A. V. Golovanov. Mineral liquid crystals. *Colloid J*, 79:421–450, 2017.
- [253] A. Kuijk, A. Imhof, M. H. W. Verkuijlen, T. H. Besseling, E. R. H. van Eck, and A. van Blaaderen. Colloidal silica rods: Material properties and fluorescent labeling. *Particle and Particle Systems Characterization*, 31(6):706–713, 2014.
- [254] J. W. Park, Y. J. Park, and C. H. Jun. Post-grafting of silica surfaces with pre-functionalized organosilanes: New synthetic equivalents of conventional trialkoxysilanes. *Chemical Communications*, 47(17):4860–4871, 2011.
- [255] A. Kuijk, D. V. Byelov, A. V. Petukhov, A. van Blaaderen, and A. Imhof. Phase behavior of colloidal silica rods. *Faraday Discussions*, 159:181–199, 2012.
- [256] A. Kuijk, T. Troppenz, L. Filion, A. Imhof, R. van Roij, M. Dijkstra, and A. van Blaaderen. Effect of external electric fields on the phase behavior of colloidal silica rods. *Soft Matter*, 10(33):6249–6255, 2014.
- [257] R. G. Weiner, D. P. Chen, R. R. Unocic, and S. E. Skrabalak. Impact of Membrane-Induced Particle Immobilization on Seeded Growth Monitored by in Situ Liquid Scanning Transmission Electron Microscopy. *Small*, 12(20):2701–2706, 2016.
- [258] J. H. Park, N. M. Schneider, J. M. Grogan, M. C. Reuter, H. H. Bau, S. Kodambaka, and F. M. Ross. Control of Electron Beam-Induced Au Nanocrystal Growth Kinetics through Solution Chemistry. *Nano Letters*, 15(8):5314–5320, 2015.
- [259] S. F. Tan, G. Lin, M. Bosman, U. Mirsaidov, and C. A. Nijhuis. Real-Time Dynamics of Galvanic Replacement Reactions of Silver Nanocubes and Au Studied by Liquid-Cell Transmission Electron Microscopy. *ACS Nano*, 10(8):7689–7695, 2016.
- [260] T. J. Woehl, J. E. Evans, I. Arslan, W. D. Ristenpart, and N. D. Browning. Direct in situ determination of the mechanisms controlling nanoparticle nucleation and growth. *ACS Nano*, 6(10):8599–8610, 2012.
- [261] J. Hermannsdörfer, N. de Jonge, and A. Verch. Electron beam induced chemistry of gold nanoparticles in saline solution. *Chem. Commun.*, 51(91):16393–16396, 2015.
- [262] G. Zhu, Y. Jiang, F. Lin, H. Zhang, C. Jin, J. Yuan, D. Yang, and Z. Zhang. In situ study of the growth of two-dimensional palladium dendritic nanostructures using liquid-cell electron microscopy. *Chemical Communications*, 50(67):9447–9450, 2014.
- [263] K. W. Noh, Y. Liu, L. Sun, and S. J. Dillon. Challenges associated with in-situ TEM in environmental systems: The case of silver in aqueous solutions. *Ultramicroscopy*, 116:34–38, 2012.
- [264] T. Kraus and N. Jonge. Dendritic Gold Nanowire Growth Observed in Liquid with Transmission Electron Microscopy. *Langmuir*, 29:8427–8432, 2013.

- [265] J. P. Patterson, P. Abellan, M. S. Denny, C. Park, N. D. Browning, S. M. Cohen, J. E. Evans, and N. C. Gianneschi. Observing the Growth of Metal-Organic Frameworks by in Situ Liquid Cell Transmission Electron Microscopy. *J. Am. Chem. Soc.*, 137:7322–7328, 2015.
- [266] Z. Aabdin, X. M. Xu, S. Sen, U. Anand, P. Král, F. Holsteyns, and U. Mirsaidov. Transient Clustering of Reaction Intermediates during Wet Etching of Silicon Nanostructures. *Nano Letters*, 17(5):2953–2958, 2017.
- [267] K. Y. Niu, J. Park, H. Zheng, and A. P. Alivisatos. Revealing bismuth oxide hollow nanoparticle formation by the Kirkendall effect. *Nano Letters*, 13(11):5715–5719, 2013.
- [268] S. W. Chee, S. F. Tan, Z. Baraissov, M. Bosman, and U. Mirsaidov. Direct observation of the nanoscale Kirkendall effect during galvanic replacement reactions. *Nature Communications*, 8(1):1–8, 2017.
- [269] Z. Zeng, X. Zhang, K. Bustillo, K. Y. Niu, C. Gammer, J. Xu, and H. Zheng. In Situ Study of Lithiation and Delithiation of MoS₂ Nanosheets Using Electrochemical Liquid Cell Transmission Electron Microscopy. *Nano Letters*, 15:5214–5220, 2015.
- [270] Y. Yang, G. Chen, L. J. Martinez-miranda, H. Yu, K. Liu, and Z. Nie. Synthesis and Liquid-Crystal Behavior of Bent Colloidal Silica Rods. *JACS*, 138:68–71, 2016.
- [271] Y. Yang, H. Pei, G. Chen, K. T. Webb, L. J. Martinez-Miranda, I. K. Lloyd, Z. Lu, K. Liu, and Z. Nie. Phase behaviors of colloidal analogs of bent-core liquid crystals. *Science Advances*, 4(5), 2018.
- [272] P. Datskos and J. Sharma. Synthesis of segmented silica rods by regulation of the growth temperature. *Angewandte Chemie International Edition*, 53(2):451–454, 2014.
- [273] M. Kamp, G. Soligno, F. Hagemans, B. Peng, A. Imhof, R. van Roij, and A. van Blaaderen. Regiospecific Nucleation and Growth of Silane Coupling Agent Droplets onto Colloidal Particles. *Journal of Physical Chemistry C*, 121(36):19989–19998, 2017.
- [274] R. Kotni. *Composite colloids (a study on self-assembly and self-propulsion)*. Phd thesis, Utrecht University, 2020.
- [275] C. J. Brinker, R. Sehgal, S. L. Hietala, R. Deshpande, D. M. Smith, D. Loy, and C. S. Ashley. Sol-gel strategies for controlled porosity inorganic materials. *Journal of Membrane Science*, 94(1):85–102, 1994.
- [276] S. Broersma. Viscous Force Constant for a Closed Cylinder. *Journal of Chemical Physics*, 32:1632–1635, 1960.
- [277] M. M. Tirado, C. L. Martínez, J. García, and D. Torre. Comparison of theories for the translational and rotational diffusion coefficients of rod like macromolecules. Application to short DNA fragments. *Journal of Chemical Physics*, 81:2047–2052, 1984.

Summary

In a nutshell, the work described in this Thesis is expressed by its title “*Chemistry and interactions of silica based particles studied by liquid cell electron microscopy*”. In order to investigate the physio-chemical properties of silica based particles, we synthesized various types of silica particles with different shapes and different chemical structures. The particle size range used in this work varied from nanometers to approximately two micrometers, which falls within the colloidal particle size domain. The charged colloidal particles as immersed in an electrolyte solution are all surrounded by an ionic ‘cloud’ formed by mobile electrolyte ions. This generates an electric double layer around the charged particles, causing colloidal particles to directly interact with each other through electrostatic interaction. In addition, the particles also interact in an indirect way due to their movement through the dispersion. This interaction is known as hydrodynamic interactions and induces a force on the colloidal particles due to solution displacement. We used the upcoming and relatively new technique ‘Liquid Phase Electron Microscopy’ (LPEM) to investigate the electrostatic and hydrodynamic interactions between charged colloidal particles at the single-particle level in real-time. Synthesizing silica nanoparticles by different methods results in particles having different chemical structures. Different shapes of silica nanoparticles typically also incorporate different chemical structures. Understanding the chemical structure of silica nanoparticles is an important step for synthesizing them with different shapes. These different shapes eventually lead to new materials with novel physical properties, also by self-assembly of these nanoparticles leading to novel collective properties. In this work, we utilized the LPEM technique to investigate the chemical structure of various types of silica nanoparticles. To this end, we monitored the etching mechanism of silica nanoparticles in basic solutions in real-time and at a single particle level as well.

In **Chapter 2**, the effects of the electron beam on silica particles in water is described. The presence of a high energy electron beam strongly affects the sample under study through direct effects on the particles and/or indirect effects through the solutions in which the particles are dispersed. We used a new class of silica particles known as rattles together with Stöber silica nanoparticles to investigate the electron beam effects on silica particles in water. Rattles are a relatively new class of particles with a distinctive core@void@shell configuration where the encapsulated core particle ‘freely’ moves within a hollow shell. In this work, we used rattles with a silica core within a silica shell. We used silica rattles with a fully condensed SiO₂ structure by heating them

to 900 °C. Upon electron beam irradiation the particles underwent a drastic expansion with an increase in particle diameter by 10%. An identical system of particles but having a lower material density achieved by pre-heating these to only 500 °C, exhibited less expansion of only 2%. In both cases, the particles underwent a more gradual shrinkage where they maintained their spherical shape even after a reduction of their diameter by 50%. This indicates that the initial expansion of the particle was related to a decrease in the density of the silica. The presence of water plays a crucial role in the expansion and shrinkage of the silica particles under electron beam irradiation. The bond breaking in the silica matrix upon electron beam irradiation at the initial stages induced the transformation from a fully condensed structure to a less condensed structure, accompanied by an increase in particle size. The continued exposure to electron beam irradiation resulted in the further breaking of bonds and loss of material, resulting in shrinkage of the particle. Without water present, the particles were only found to condense to higher density (~15% decrease in radius) upon electron irradiation under the same dose and energy. The fact that the particle maintained its spherical shape during the drastic shrinkage indicates that a considerable internal restructuring occurred in the silica matrix. This may also explain another observation where the silica particle became elongated along the scanning direction. The shape deformation of silica particles was found to be induced by the scanning electron beam, as only the particles in the field of view underwent this drastic shape deformation and it was found to be dependent on the accumulated electron dose. These observations showed that it is extremely important to understand the electron beam effects on the sample under study in an LC-STEM experiment. Furthermore, we showed that the optimization of the LC-STEM parameters is a prerequisite for conducting any LC-STEM experiment.

The optimized LC-STEM parameters determined in Chapter 2 were used in **Chapter 3** to investigate the electrostatic and hydrodynamic interactions between charged colloidal particles. Rattle particles having silica or a titania core within a silica shell with two distinct shell sizes were used to study the diffusion of colloidal particles confined in a spherical shell. By increasing the electron dose rate, the core particle was found to move closer to the shell when particles were dispersed in water. When the electron dose rate was increased to a certain value, the core particle became irreversibly attached to the shell. Among multiple effects of the electron beam that may explain this observation, the effect of the increase in ionic strength is not that significant for our system because we did not try to keep the ionic strength as low as it possibly can be in water ($\sim 10^{-5}$ M); changes in pH and direct charging effects were more likely to play an important role. We used glycerol carbonate as a solution to slow down the movement of the core particle in order to perform a quantitative analysis of the diffusion of the colloidal particles confined in spherical geometry. We found that the diffusion coefficient of the silica core particle was largely unaffected by increasing the electron dose rate, whereas it decreased

for titania core particle. We also showed that the diffusion coefficient was larger for the particles diffusing within bigger shells. Moreover, we showed the asymmetrical behavior of the diffusion of the particles as the mobility should be decoupled into two components: a component in the radial direction and a component along the shell wall. We showed that the radial diffusion coefficient decreased as the core particle moved closer to the shell, while the diffusion coefficient of the component along the shell wall remained constant within most of the shell. Additionally, we showed that the diffusion of the core particle in the center of the shell was already slower in comparison to free Brownian diffusion of an identical particle; This is due to the long-range character of the hydrodynamic interactions.

In **Chapter 4**, we synthesized silica nanoparticles using different methods which resulted in nanoparticles having different chemical structures. We used three main procedures to synthesize spherical silica nanoparticles; Stöber, water-in-oil microemulsion, and Amino Acid-Catalyzed (AAC) syntheses. We performed in-situ and ex-situ etching of silica nanoparticles in basic solutions to study their chemical structures. Ex-situ etching of AAC silica nanoparticles showed a slow and gradual etching in basic solutions. We exploited this property of AAC silica nanoparticles to characterize the electron beam effects during LC-(S)TEM studies of silica in aqueous and basic aqueous solutions. We found that the cumulative electron dose was the most important factor in observing the etching of silica particles and this determined whether the observed etching process was compatible with its ex-situ counterpart or not. We showed that silica expanded prior to etching and that the extent of that expansion was directly correlated with the cumulative electron dose on the imaging area, independent of the used electron dose rate. Moreover, we found that the expansion of silica nanoparticles was more pronounced in basic solutions. However, our findings suggested that the expansion observed cannot be completely explained by the presence of water radiolysis products. Therefore, we performed Monte-Carlo simulations to investigate the energy absorbed per unit volume by a silica nanoparticle of around a hundred nanometers on the top window of a liquid cell, due to the exposure during the acquisition of one frame. The absorbed energy was found to be always similar, or up to orders of magnitude higher, than the energy needed to directly disturb the silica network. This revealed the importance of optimizing the cumulative electron dose when performing in-situ studies on chemical reactions in LC (S)TEM experiments. After we determined and fine-tuned optimized conditions, we reliably characterized the wet etching behavior of Stöber silica, silica made by water-in-oil microemulsion method (WORM silica), and Au@Stöber silica and Fe₃O₄@WORM silica core-shell nanoparticles. We successfully showed the formation of nano-rattle particles from Au@Stöber silica and Fe₃O₄@WORM silica core-shell nanoparticles at the single-particle level where the catalyst core became a movable particle inside the shell.

Finally, in **Chapter 5** we utilized a recently developed shape of silica particles to study their chemical structure. These rod-shaped silica particles can be used as an initial template for other rod-shaped silica particles such as cones. By understanding the chemical structure of rod-shaped particles one can etch these particles in a controlled manner to obtain particles with new shapes. Therefore, we used LC-STEM to monitor the etching behavior of rod-shaped silica particles in basic solutions in time. Using the knowledge of Chapter 4 we performed in-situ etching experiments. We showed that the electron beam effects were minimized and that the in-situ etching was comparable with its ex-situ counterpart for particles freely floating in solution and for an etched system where the particles were stuck onto LC window. The LC-STEM observations revealed an inhomogeneous chemical structure along with the rod-shaped silica particles. Moreover, in real-time, we showed a three-step etching mechanism that transformed the rod-shaped silica particle to a cone-shaped silica particle. Furthermore, we found that the confined geometry of the liquid cell significantly altered the etching behavior of rod-shaped silica particles. The observations showed that the etching mechanism of silica rods when they were attached to the SiN window was different from the etching mechanism for identical particles when these underwent Brownian motion while diffusing in solution. We further validated our LC-STEM conditions using a new class of silica rod-shaped particles where the chemical structure of the rod was tailored deliberately. The etching of segmented silica rods took place as expected which indicated the LC-STEM optimized conditions found in this work indeed enable the in-situ monitoring of such processes. Finally, we used the optimized condition found in this chapter to investigate the chemical structure of crooked silica rods which were developed in the last two years. The results revealed that the synthesis procedure greatly affects the chemical structure of the crooked silica rods. The LC-STEM results helped to optimize the synthesis parameters to obtain particles with the desired shape and chemical structure.

In general, in this work, we showed that the LC-STEM technique can be made into a reliable method to study the chemical reactions as well as the physical properties of colloidal nanoparticles at the single-particle level in real-time with a high spatial resolution.

Samenvatting

Het werk dat wordt beschreven in dit proefschrift wordt kort maar krachtig samengevat in de titel: “*Chemie en interacties van silica-gebaseerde deeltjes bestudeerd met behulp van vloeistofcel-elektronenmicroscopie*”. Om de fysiochemische eigenschappen van silica-gebaseerde deeltjes te bestuderen hebben we verschillende types silicadeeltjes gesynthetiseerd met verschillende vormen en chemische structuren. De deeltjesgroottes die in dit werk zijn gebruikt liggen tussen een paar nanometer en ongeveer twee micrometer, hetgeen binnen het domein van colloïdale deeltjes valt. Geladen colloïdale deeltjes in een elektrolytische vloeistof worden omringd door een ionische “wolk” die gevormd wordt door mobiele ionen. Hierdoor wordt een elektrische dubbellaag gevormd rondom de geladen deeltjes, waardoor colloïdale deeltjes elkaar direct beïnvloeden door elektrostatische interacties. Bovendien beïnvloeden deeltjes elkaar ook op een indirecte manier door hun beweging in de vloeistof. Deze interactie die bekend staat als hydrodynamische interactie wordt veroorzaakt door een kracht op de colloïdale deeltjes door de verplaatsing van de vloeistof. We gebruiken de recent opgekomen en relatief nieuwe methode die Vloeistoffase Elektronenmicroscopie wordt genoemd om elektrostatische en hydrodynamische interacties tussen geladen colloïdale deeltjes *live* te bestuderen op het niveau van een enkel deeltje. De synthese van silica nanodeeltjes door verschillende methodes resulteert in deeltjes met verschillende chemische structuren. Verschillende vormen van silica nanodeeltjes hebben doorgaans ook verschillende chemische structuren. Het begrijpen van de chemische structuur van silica nanodeeltjes is een belangrijke stap om synthese van verschillende vormen te realiseren, hetgeen uiteindelijk kan leiden tot nieuwe materialen met nieuwe fysische eigenschappen. Ook zelforganisatie van deze nanodeeltjes kan leiden tot nieuwe collectieve eigenschappen. In dit werk gebruiken we Vloeistoffase Elektronenmicroscopie om de chemische structuur van verschillende types silica nanodeeltjes te onderzoeken. Hiervoor hebben we het etsen van silica nanodeeltjes in basische oplossingen *live* bekeken op het niveau van een enkel deeltje.

In **Hoofdstuk 2** worden de effecten van de elektronenbundel op silica deeltjes in water beschreven. De aanwezigheid van de hoog-energetische elektronenbundel beïnvloedt het monster dat onderzocht wordt hevig door directe effecten op het deeltje en/of indirecte effecten door de vloeistof waarin de deeltjes zich bevinden. We gebruikten een relatief nieuwe klasse van silica deeltjes die bekend staan als ‘rammelaardeeltjes’ en ook Stöber silica nanodeeltjes om de effecten veroorzaakt door de elektronenbundel

op silica nanodeeltjes in water te onderzoeken. Rammelaardeeltjes zijn een nieuwe klasse van deeltjes met een kern@holte@schil configuratie waar het kerndeeltje ‘vrij’ kan bewegen binnen de holle schil. In dit werk hebben we rammelaardeeltjes gebruikt die bestaan uit een silica kern en een silica schil. We hebben silica rammelaardeeltjes gebruikt met een volledig gecondenseerde SiO₂ structuur door ze te verhitten tot 900 °C. Wanneer deze werden beschenen met de elektronenbundel groeiden de deeltjes drastisch met een toename van wel 10% in diameter. Een identiek systeem van deeltjes, behalve dat ze een lagere specifieke dichtheid hadden door ze van te voren maar tot 500 °C te verhitten, groeiden maar 2% in diameter. In beide gevallen slonken de deeltjes na het groeien langzaam terwijl ze hun bolvorm behielden, zelfs nadat ze geslonken waren tot slechts 50% van hun originele diameter. Dit geeft aan dat de initiële groei van de deeltjes gerelateerd was aan het afnemen van de dichtheid van het silica deeltje. De aanwezigheid van water vervult een cruciale rol in het laten groeien en slinken van de silica deeltjes tijdens het beschijnen met de elektronenbundel. Het breken van bindingen in de silica matrix door het beschijnen met de elektronenbundel in het begin van het proces zorgde voor een transformatie van een volledige gecondenseerde structuur naar een minder gecondenseerde structuur, wat zich uit in een groei van de deeltjesgrootte. Het langer beschijnen met de elektronenbundel resulterde in het breken van meer verbindingen waardoor materiaal verloren ging, hetgeen zich uitte in het slinken van het deeltje. Als de deeltjes zich niet in water bevonden kregen de deeltjes alleen een hogere dichtheid (15% vermindering in de straal) door het beschijnen met de elektronenbundel met dezelfde dosis en energie. Het feit dat het deeltje zijn bolvorm behield tijdens het drastische slinken wijst erop dat interne herstructurering plaatsvond in de silica matrix. Dit zou ook een andere observatie kunnen verklaren waarbij het silica deeltje uitgerekt werd in de scan richting van de elektronenbundel. Het veranderen van de vorm van silica deeltjes werd veroorzaakt door het scannen met de elektronenbundel, omdat alleen de deeltjes die in het gescande gebied aanwezig waren deze drastische vormverandering ondergingen. Deze vormverandering bleek afhankelijk te zijn van de geaccumuleerde elektronendosis. Deze observaties laten zien dat het extreem belangrijk is om de effecten van de elektronenbundel op het bestudeerde monster te begrijpen in een vloeistofcel-elektronenmicroscopieëxperiment. Bovendien hebben we laten zien dat het optimaliseren van elektronenmicroscopieparameters een vereiste is om een vloeistofcel-elektronenmicroscopieëxperiment uit te voeren.

De geoptimaliseerde elektronenmicroscopieparameters die werden vastgesteld in Hoofdstuk 2 zijn in **Hoofdstuk 3** gebruikt om de elektrostatische en hydrodynamische interacties tussen geladen colloïdale deeltjes te onderzoeken. Rammelaardeeltjes met een silica of titania kern in een silica schil met twee duidelijk verschillende schilgroottes werden gebruikt om de diffusie van colloïdale deeltjes binnen in een bolvormige schil te bestuderen. Door de elektronendosis per seconde te verhogen kon de kern dichter bij de

schil komen wanneer de deeltjes in water zaten. Wanneer de elektronen dosis per seconde verhoogd werd tot een bepaald niveau bleef het kerndeeltje irreversibel vastzitten aan de schil. Onder de vele effecten van de elektronenbundel die deze observatie zouden kunnen verklaren is het effect van een verhoogde ionenconcentratie in ons systeem niet significant omdat we niet hebben geprobeerd de ionen concentratie zo laag mogelijk te houden als deze kan zijn in water ($\sim 10^{-5}$ M). Veranderingen in de pH en directe opladingseffecten spelen waarschijnlijk een belangrijkere rol. We hebben glycerolcarbonaat gebruikt als vloeistof om het kerndeeltje langzamer te laten bewegen opdat we een kwantitatieve analyse konden doen voor de diffusie van een colloïdaal deeltje opgesloten in een bolvormige geometrie. We kwamen erachter dat de diffusiecoëfficiënt van het silica kerndeeltje niet veel veranderde door de elektronendosis per seconde te verhogen, terwijl de diffusiecoëfficiënt van het titania kerndeeltje afnam bij hogere elektronendosis per seconde. We lieten ook zien dat de diffusiecoëfficiënt groter was voor deeltjes die in een grotere schil bewegen. Bovendien lieten we de asymmetrie zien in de diffusie van de kerndeeltjes omdat de mobiliteit in twee componenten moet worden opgedeeld: een radiale component en een component langs de schilwand. We lieten zien dat de radiale component van de diffusiecoëfficiënt afneemt wanneer het kerndeeltje dichter bij het schilletje komt, terwijl de component langs de schilwand constant blijft in het grootste gebied binnen de schil. We lieten ook zien dat de diffusie van het kerndeeltje in het midden van de bolvormige geometrie al langzamer was dan een deeltje dat zich niet in een schil bevindt. Dit komt doordat hydrodynamische interacties over vrij lange afstanden tot uiting komen.

In **Hoofdstuk 4** hebben we silica nanodeeltjes gemaakt met verschillende methodes die ervoor zorgen dat de nanodeeltjes een verschillende chemische structuur hebben. We hebben drie procedures gebruikt om bolvormige silicadeeltjes te maken; Stöber, water-in-olie micro-emulsie, en Amino Acid Catalyzed (AAC) syntheses. We hebben silica nanodeeltjes in-situ en ex-situ geëtst in basische oplossingen om de chemische structuur van deze deeltjes te onderzoeken. Het ex-situ etsen van AAC silica nanodeeltjes liet zien dat het etsen langzaam en geleidelijk ging in basische oplossingen. We gebruikten deze eigenschap van AAC silica nanodeeltjes om de effecten van de elektronenbundel te karakteriseren tijdens vloeistofcel-experimenten van silica in water en basische oplossingen. We kwamen erachter dat de cumulatieve elektronendosis de belangrijkste factor was in het observeren van het etsen van silica nanodeeltjes en dit bepaalde of het geobserveerde proces van etsen overeenkwam met het ex-situ proces van etsen of niet. We lieten zien dat silica deeltjes uitzetten voordat het etsen begint en dat de mate van uitzetten direct correleerde met de cumulatieve elektronendosis over het gebied dat bekken wordt, onafhankelijk van de gebruikte elektronendosis per seconde. Bovendien kwamen we erachter dat het uitzetten van de silica nanodeeltjes meer tot uiting kwam in basische oplossingen. Onze bevindingen suggereren dat het

uitzetten van de deeltjes niet volledig kan worden uitgelegd door de aanwezigheid van radiolyseproducten. Daarom hebben we Monte-Carlo simulaties gedaan om de energie per volume die geabsorbeerd wordt door een silica nanodeeltje van ongeveer honderd nanometer die vastzit aan de bovenkant van de vloeistofcel te onderzoeken tijdens het maken van één frame met de elektronenbundel. De geabsorbeerde energie was altijd ongeveer gelijk, of zelfs ordegroottes hoger, dan de energie die benodigd was om de silica matrix direct te verstoren. Dit liet zien hoe belangrijk het is om de cumulatieve elektronendosis te optimaliseren wanneer een *in-situ* studie van chemische reacties in vloeistofcel-elektronenmicroscopie gedaan wordt. Nadat we de condities bepaald en geoptimaliseerd hadden, hebben we op een betrouwbare manier het natte etsen van Stöber silica, silica gemaakt met de water-in-olie microemulsie methode (WORM silica), en Au@Stöber silica en Fe₃O₄@WORM silica kern-schil nanodeeltjes, gekarakteriseerd. We hebben met succes laten zien hoe de formatie van nano-rammelaardeeltjes plaatsvindt van Au@Stöber silica en Fe₃O₄@WORM silica kern-schil nanodeeltjes op het niveau van één deeltje waar de katalysatorkern een bewegend deeltje binnen het schilletje werd.

Tenslotte gebruikten we in **Hoofdstuk 5** een recent ontwikkelde vorm van silica deeltjes en bestudeerden hun chemische structuur. Deze staafvormige silica deeltjes kunnen gebruikt worden als een initiële vorm voor andere staafvormige silica deeltjes zoals een ijshoorntjesvorm. Door de chemische structuur van staafvormige deeltjes te begrijpen kunnen we deze deeltjes op een gecontroleerde manier etsen om deeltjes met nieuwe vormen te verkrijgen. Daartoe gebruiken we vloeistofcel-elektronenmicroscopie om het gedrag van etsen van staafvormige silica deeltjes in basische oplossingen in de tijd te bekijken. Met de kennis van Hoofdstuk 4 hebben we *in-situ* experimenten gedaan waarbij we deeltjes etsten. We lieten zien dat de effecten van de elektronenbundel geminimaliseerd waren en dat het etsen van deeltjes *in-situ* vergelijkbaar was met het etsen van deeltjes *ex situ* wanneer de deeltjes vrij in de vloeistof bewegen en voor een systeem waar de deeltjes vastzaten aan de wand van de vloeistofcel. De observaties gedaan met vloeistofcel-elektronenmicroscopie onthulden dat de staafvormige silica deeltjes een inhomogene chemische structuur hadden. Bovendien konden we *live* laten zien dat een drie-staps etsmechanisme zorgde voor een transformatie van de staafvormige silica deeltjes naar silica deeltjes met een ijshoorntjesvorm. Ook kwamen we erachter dat de beperkende geometrie van de vloeistofcel het gedrag qua etsen van staafvormige silica deeltjes significant beïnvloedt. De observaties laten zien dat het mechanisme van het etsen van silica staafjes die aan de bovenkant van de vloeistofcel vastzaten anders was dan het mechanisme van etsen van identieke deeltjes die via Browniaanse beweging door de vloeistof bewogen. We valideerden onze vloeistofcel-elektronenmicroscopie condities verder door een nieuwe klasse van staafvormige silica deeltjes te gebruiken waar de chemische structuur van het staafje bewust op maat gemaakt was. Het etsen

van gesegmenteerde silica staafjes vond plaats als verwacht, hetgeen aangaf dat de geoptimaliseerde condities voor vloeistofcel-elektronenmicroscopieëxperimenten die in dit werk gevonden zijn, het mogelijk maken om zulke processen in-situ te bekijken. Tenslotte gebruikten we de geoptimaliseerde condities die gevonden zijn in dit hoofdstuk om de chemische structuur van kromme silica staafjes die in de laatste twee jaar ontwikkeld zijn te onderzoeken. De resultaten lieten zien dat de syntheseprocedure de chemische structuur van kromme silica staafjes zeer sterk beïnvloedt. De resultaten verkregen met vloeistofcel-elektronenmicroscopie hebben geholpen om de syntheseparameters te optimaliseren en zodoende deeltjes met de verlangde vorm en chemische structuur te verkrijgen.

In het algemeen hebben we in dit werk laten zien dat vloeistofcel-elektronenmicroscopie een betrouwbare methode kan zijn om zowel chemische reacties als fysische eigenschappen van colloïdale nanodeeltjes *live* te bestuderen op het niveau van een enkel deeltje met een hoge plaatsresolutie.

Acknowledgments

“As you start to walk on the way, the way appears.” I always tried to stick to this poem from ‘Rumi’ during my Ph.D. journey and during all those tough moments that I was asking myself “how do I get out of it!” And here I am, on my way to completing my Ph.D. When I look back to this complicated and intriguing journey, I realize it was not only about delving and solving scientific problems, but also a journey to improve different aspects of my personality and my life. I am happy that I have this opportunity to sit before my laptop and recall how much I have been helped by so many people in the last four years. I would like to take this opportunity to thank the people who supported and helped me during these years without whom it was not possible to complete this journey.

First of all, I would like to express my sincere gratitude towards Marijn, and Alfons, my supervisors. Thank you for providing me an opportunity to complete my Ph.D. thesis in your research group. To my daily supervisor Marijn, your support during all these years has been invaluable. You always helped me with my scientific and non-scientific queries and you were always the first person that addressed my doubts and encouraged me in this way. Thank you for always being supportive and helpful. Alfons, I have been extremely lucky to have you as my supervisor and I could not speak more highly of you as a group leader. You were full of new scientific ideas about my research project and your feedback in every meeting guided me and the project in a successful direction. I cannot express how much I learned from you during my Ph.D. life. I thank both of you for giving me the necessary freedom in my scientific research.

The next goes to my collaborators, liquid cell team, Chefs, Tom, and Albert. Definitely, I am not willing to reduce our valuable relationship to collaborators. Your friendship and support during these years have been priceless for me. My Ph.D. wouldn’t be as successful as it is now without your help and contribution. Tom, I still recall the day you entered my office and asked me to do liquid cell experiments together with great enthusiasm. Your eagerness in performing new experiments together with your great knowledge and intelligence inspired me through these years. I enjoyed a lot working with you. Thank you for our in-depth football discussions and debates and thank you for enlightening me that the greatest club in the Netherlands is ‘PSV’, although in whole my life I preferred ‘PSV’ to ‘Ajax’. Thank you for our ps4 game nights and all those tasty Indonesian food that you prepared. I greatly appreciate your effort in reading all my chapters and papers and even this acknowledgment and your fruitful

comments. Also, thank you for carefully translating my thesis summary in Dutch. Albert, you are a true friend also with great knowledge and intelligence who has been positive encountering difficult challenges. You were always there to help me with my experiments and countless unknown issues with liquid cell. Your can-do spirit inspired me through these years. I also enjoyed all our discussions about politics, games, series, Arabic language, and so many other topics. I admire your great love for Catalonia and I wish all the peace and freedom for this lovely part of the world and history. Lately but exactly at the right time, we discovered your hidden talent in designing professional beautiful images. Thank you for spending so much time designing the beautiful cover image of my thesis. To both of you, I have been very lucky to establish the liquid cell team at the Soft Condensed Matter group with such great scientists as you. I have so many memorable moments with you during our travels for different conferences, and I am sure that our friendship will last for longer times.

Furthermore, I would like to thank the scientific staff of our SCMB group: Arnout, René, Marjolein, Patrick, Joost, Freddy, Laura, Krassimir, Hans, and Gerhard. Thank you for all your valuable comments and suggestions which have greatly improved my scientific research, results, and presentations. Arnout, thank you for the fruitful discussions and your nice comments on silica-based particles. I am honored to work in such a group with outstanding academic performance.

This thesis would not have been possible without help from the technical and supporting staff. Chris and Hans, thank you for providing a pleasant atmosphere at the microscopy center. Electron microscopy was the key instrument in the completion of this thesis, and you were extremely supportive in both technical and less technical issues during these years. Chris, I admire how you always helped me to solve problems regardless of how big they were during my microscopy experiments. Hans, I thank you for your helpful microscopy tips which made my experiments smoother. Thank you both for all the funny moments that you shared with me. Peter and Dave, I thank you for your willingness to help me with all sorts of problems that I encountered using my computer and other equipment. Relinde, Elleke, and Judith thank you for making our labs a safe and well-organized place to work. Thank you Relinde for your useful experimental tips in silica synthesis. Hester, Dianne, and Marion, I am grateful for all your efforts to arrange official procedures during these years. Hester, you are a kind person who helped me so much with documents and official procedures. Marion, I appreciate your efforts in finding a place for me in Utrecht which is not an easy task to do.

I would like to call out every single member of the SCM group to thank. This starts with all the people who have shared an office with me. Yang, Somil, Murphy, Xiaobin, Judith, Berend, Robin, and Tom. Somil, thank you for your motivational talks during those moments that I was feeling extremely homesick. Yang and Xiaobin, thanks for

the memories that we made together while traveling for conferences, and thank you for scientific discussions in the microscopy field. Murphy, I shared an office with you for a shorter amount of time but your way of doing science inspired me during these years. Robin, the most well-organized office-mate I ever had, I enjoyed sharing an office with you, thank you for your patience during me and Tom's sometimes nonsensical discussions. Tom, on top of all I mentioned before about you, I would like to thank you for being a great office-mate as well. Judith, although we shared an office for a short time, recalling our conversations always brings a smile on my face.

Naveed, your constant positivity inspired all the members of the SCM group, we shared so many special moments due to our common nationality and culture. We discussed so many good and bad news about our country and we shared moments full of hope and fear at the same time. Thank you for being always available to talk in all tough moments during these years and I am sure our friendship will last for longer times. Rama, my lord, you are the funniest person in the SCM group according to almost everyone who knows you. We shared so many funny moments together however we also shared so many tough moments together during our Ph.D. I enjoyed our in-depth discussions about India, Iran, immigration and its difficulties, Indian movies and songs and so many other topics. Thanks to Italians Massi, Emanuele, and Gabriele who were in my neighbor's office, even though your voice tone while talking about serious stuff always made me think that we share the same office! I shared very nice moments with you guys and you were always so kind and welcoming to me during these years. Also thanks for being patient when I and Naveed were talking about Pizza as it is an Iranian food. Wessel, thank you for being my 'Buddy' and sharing your scientific and non-scientific experiences with me when I started my Ph.D. in the SCM group. Fabian, I admire your generosity in sharing your knowledge and your synthesized particles with me, thanks for your help. Chris, you helped me so many times during my chemical experiments, thanks! Xiaodan and Dnyaneshwar, thank you for making nice memories with me during our Berlin trip. I enjoyed your company. Nynke, Mark, and Lars thank you for sharing your results of the liquid cell experiments, and thanks for fruitful discussions. A special thanks to Simone, Ernest, Wiebke, Guido, Nick, Giulia, Tonnishtha, Vassilis, Doug, Carmine, and Maarten for your endless effort to foosball and our fun moments improving our foosball skills! I am also grateful to all former and current members of the SCM group. Jessi, Vats, Pepijn, Henriëtte, Sid, Da, Harini, Rik, Anna, Frankje, Ravi, Ajoy, Federico, Alberto, Arya, Kelly, Harith, Zahra, Stijn, Mark, Erik, and Sander thank you for creating a lovely atmosphere during these years in the Ornstein Laboratory.

Moving to the Netherlands gave me this opportunity to visit many great people apart from scientific life. Kanako, I may have met you only a few times because of the great distance between Japan and the Netherlands. However, your help was significantly

important in the completion of this thesis. Also, thank you for all the tasty Japanese food you prepared. Paula, thank you for your company in our outgoings and BBQs. Samaneh, Amin, Sanaz, Fahimeh, and Mahdi I was so lucky to meet you here in the Netherlands. You were always extremely friendly and supportive who shared so many nice moments with me. I would like to give a special mention to the group of my friends at Delft university who shared great moments with me during the past four years. Ali Haseltalab, Ali Jamshidi, Mehdi, Reza, Nina, Saba, Mahya, Mojtaba, Farzaneh, Javad, Shahrzad Nikghadam, Zohre, Behzad, Amir, and Somaieh, thank you for your support and for our trips altogether. Hopefully, we will continue this nice friendship. From the first days of my presence in the Netherlands, I had the chance to meet up with one of the greatest maestros in Iranian classical music. Hamid Motebassem, you were the one who kept me connected to my country and its great culture. I simply cannot express how much I learned from you, thanks! Similarly, I would like to express my gratitude to Samira Golbaz for being a kind and impressive music teacher. Ali Hashemi, Ebrahim, Hossein, Nadjla, Behrooz, Mohsen, Nima, Arash, Javid, Nasser, and all other musicians that I met here in the Netherlands thank you for the nice collaboration and our delightful concerts around Europe. My old friends, Sajjad and Sanaz who happened to move to the Netherlands recently. I am grateful for every single moment that we shared together during these years and I am sure we still have so many years of friendship ahead of us. Sina ABD, a true and old friend who helped me in every stage of my life and education regardless of the geographical distance between us, thank you! Arash and Roza, thank you for making our trips to Germany so pleasant and similarly Shabnam, Mina, and Kaveh thanks for your lasting friendship and great hosting in Istanbul.

I would also like to express my gratitude to my supervisors from Sabancı university during my Master's studies. Mali and Meltem, although we have not met for almost four years I am grateful for your efforts teaching me different microscopy techniques which is the reason that I ended up in this field and I am happy about it.

During my years far from my family, I received unconditional support from them despite the long distance between us. Maman and Baba, you are the reason I am where I am today. Thank you for your endless encouragement during these years. Nasim, thank you for being an awesome sibling and for all your supports. Amir, my lovely brother-in-law, thank you for your supports! Hirad, my sweet nephew you increased my motivation simply by coming into this world 2 years ago. I would like to thank my parents-in-law, Zeynab, and Nasser for the extended support during these years.

Above all, I would like to thank my wife Shahrzad for her love and constant support. Dear Shahrzad, the beginning of this journey was coincident with the beginning of our common life. During the last four years, you always stood by me through the ups and downs. Thank you for being extremely patient when I was complaining about my countless failed experiments to you! You gave me support and help, discussed ideas,

and prevented several wrong turns! Thank you for keeping me sane over the past four years. Thank you for being my best friend!

Sina (July 2020, Utrecht)

List of Publications

THIS THESIS IS BASED ON THE FOLLOWING PUBLICATIONS:

- W. Vlug/**S. Sadighikia**, K. Watanabe, D. Nagao, M.A. van Huis, and A. van Blaaderen, Beam induced dissolution of silica in liquid cell Scanning Transmission Electron Microscopy, *in preparation* (**Chapter 2**)
- T.A.J. Welling, **S. Sadighikia**, Daphne Dekker, A. van Blaaderen, and M.A. van Huis, Colloidal diffusion and hydrodynamic interactions in a rigid spherical shell, *in preparation* (**Chapter 3**)
- A. Grau-Carbonell/**S. Sadighikia**, T.A.J. Welling, R. Moes, R. Kotni, M. Bransen, A. van Blaaderen, and M.A. van Huis, In-situ study of the wet chemical etching of SiO₂ and Metal(Oxide)@SiO₂ core-shell nanospheres, *Submitted* (**Chapter 4**)
- **S. Sadighikia**/A. Grau-Carbonell, T.A.J. Welling, M.A. van Huis, and A. van Blaaderen, Complex internal chemical structures of rod-shaped silica colloids investigated by in-situ etching using low-dose liquid cell Electron Microscopy, *Submitted* (**Chapter 5**)

OTHER PUBLICATIONS BY THE AUTHOR:

- T.A.J. Welling, **S. Sadighikia**, K. Watanabe, A. Grau-Carbonell, M. Bransen, D. Nagao, A. van Blaaderen, M.A. van Huis, Observation of unrestricted 3D Brownian motion of nanoparticles using liquid-cell scanning transmission electron microscopy, *Particle and Particle Systems Characterization*, (2020), 37, 6, 2070014
- K.Watanabe, T.A.J.Welling, **S. Sadighikia**, H. Ishii, A. Imhof, M.A. van Huis, A. van Blaaderen, D. Nagao, Compartmentalization of gold nanoparticle clusters in hollow silica spheres and their highly dense assembly induced by an external electric field, *JCIS*, (2020), 566, 202-210
- S. Abdolhosseinzadeh, **S. Sadighikia**, S. Alkan Gürsel, Scalable Synthesis of Sub-Nanosized Platinum-Reduced Graphene Oxide Composite by an Ultraprecise Photocatalytic Method, *ACS Sustainable Chem. Eng.*, (2018), 6(3), 3773-3782

- S. Abdolhosseinzadeh, H. Asgharzadeh, **S. Sadighikia**, A. Khataee, UV-assisted synthesis of reduced graphene oxide-ZnO nanorod composites immobilized on Zn foil with enhanced photocatalytic performance, *Research on Chemical Intermediates*, (2016), 42(5), 4479-4496
- M. Shakoori Oskooie, H. Asgharzadeh, **S. Sadighikia**, M. Salehi, Significant Corrosion Resistance in an Ultrafine-Grained Al6063 Alloy with a Bimodal Grain-Size Distribution through a Self-Anodic Protection Mechanism, *Metals*, (2016), 6(12), 307
- **S. Sadighikia**, S. Abdolhosseinzadeh, H. Asgharzadeh, Production of high porosity Zn foams by powder metallurgy method, *Powder metallurgy*, (2015), 58(1), 61-66
- M. Sezen, **S. Sadighikia**, 3D electron microscopy investigation of human dentin at the micro/nanoscale using focused ion beam based nanostructuring, *RSC Advances*, (2015), 5(10), 7196-7199
- S. Ghobadi, **S. Sadighikia**, M. Papila, F. Cebeci, S. Alkan Gürsel, Graphene-reinforced Poly(vinyl alcohol) electrospun fibers as building blocks for high performance nanocomposites, *RSC Advances*, (2015), 5(103), 85009-85018
- A. Karimzad Ghavidel, T. Azdast, M.R. Shabgard, A. Navidfar, **S. Sadighikia**, Improving electrical conductivity of poly methyl methacrylate by utilization of carbon nanotube and CO₂ laser, *J. Appl. Polym. Sci.*, (2015), 132, 42671

About the Author

Sina Sadighikia was born on the 12th of May 1990 in Tabriz, Iran. In 2008, after finishing high school with a major in physics and mathematics he started to study Metallurgical Engineering at the University of Tabriz where he obtained his bachelor's degree. In 2013, he moved to Istanbul, Turkey to pursue his studies in the field of Materials Science and Engineering at the University of Sabancı. During this period he was awarded a scholarship by the Scientific And Technological Research Council Of Turkey (TÜBITAK) to develop high-resolution electron microscopy techniques, such as HR-TEM, SEM, and FIB to study the micro and nano features within porous materials at the Sabancı University Nanotechnology Research and Application Center (SUNUM) under the supervision of Prof. dr. Mehmet Ali Gülgün and Dr. Meltem Sezen. With the thesis title "3D electron microscopy investigations of human dentin and ion beam irradiation effect on biocompatible anatase TiO₂ using Focused Ion Beam based techniques" he obtained his Master's degree in Material Science and Engineering in January 2016. Shortly after, in March 2016 he moved to the Netherlands and started his Ph.D. project in the Soft Condensed Matter group of Debye Institute for Nanomaterials Science at Utrecht University under the supervision of Prof. dr. Alfons van Blaaderen and Dr. Marijn van Huis. During his Ph.D. he mainly worked on developing liquid phase electron microscopy as a powerful technique to study the physio-chemical properties of colloidal nanoparticles. The highlights of his scientific work have been published in peer-reviewed scientific journals, and have been presented at several national and international conferences.

Apart from his studies and research, Sina enjoys Iranian classical music. He plays Tar (a classical music instrument from Iran) and he is a member of the Iranian classical music orchestra with Hamid Motebassem as its chief conductor in the Netherlands which performs yearly concerts all around Europe. Besides, he enjoys activities like reading, playing computer games, football, squash, and traveling.